Computer Simulation Studies on Supercritical Carbon dioxide

A Thesis

Submitted For the Degree of

DOCTOR OF PHILOSOPHY

in the Faculty of Science

by

Moumita Saharay

CHEMISTRY AND PHYSICS OF MATERIALS UNIT
JAWAHARLAL NEHRU CENTRE FOR ADVANCED SCIENTIFIC RESEARCH
(A DEEMED UNIVERSITY)
Bangalore – 560 064, India

FEBRUARY 2007

Dedicated to my family

DECLARATION

I hereby declare that the matter embodied in the thesis entitled "**Computer Simulation Studies on**
Supercritical Carbon dioxide" is the result of investigations carried out by me at the Chemistry and Physics of Materials Unit, Jawaharlal Nehru Centre for Advanced Scientific Research, Bangalore, India under the supervision of Prof. S. Balasubramanian and that it has not been submitted elsewhere for the award of any degree or diploma.

In keeping with the general practice in reporting scientific observations, due acknowledgement has been made whenever the work described is based on the findings of other investigators. Any omission that might have occurred by oversight or error of judgement is regretted.

Moumita Saharay

CERTIFICATE

I hereby certify that the matter embodied in this thesis entitled "**Computer Simulation Studies on**
Supercritical Carbon dioxide" has been carried out by Ms. Moumita Saharay at the Chemistry and Physics of Materials Unit, Jawaharlal Nehru Centre for Advanced Scientific Research, Bangalore, India under my supervision and that it has not been submitted elsewhere for the award of any degree or diploma.

Prof. S. Balasubramanian
(Research Supervisor)

Acknowledgements

It is my pleasure to thank my research supervisor Prof. S. Balasubramanian for giving me an opportunity to work on this exciting research project and for introducing me to the state-of-the-art simulation techniques. I am extremely thankful to him for providing me excellent research training, support, and encouragement right from the beginning of this project. He has also given me academic freedom to carry out my work and has constantly encouraged me to innovate. I sincerely acknowledge him for providing me excellent computing facilities without which this work would not have taken a good shape. I hope that the research training that I have received from him will surely help me to pursue even more difficult problems in the coming years.

I express my sincere gratitude to Prof. C.N.R. Rao for research support and for being a source of inspiration for me.

I would like to take this opportunity to thank all the faculty members of CPMU and TSU for the fruitful discussions I had with them and for the courses they offered. I am particularly thankful to Prof. Swapan K. Pati (TSU, JNCASR), Prof. Srikanth Sastry (TSU, JNCASR), Dr. Chandrabhas Narayana (CPMU, JNCASR), and Prof. H. Balaram (MBGU, JNCASR) for showing interest in my academic advancements and for their caring words.

It is my pleasure to acknowledge the developers of Car-Parrinello Molecular Dynamics (CPMD) code, which was the principal tool for our research work. I also thank the CPMD community and its mailing list (in particular, Dr. A. Kohlmeyer) for providing us helpful

discussions and suggestions on the implementation of this code. Thanks are also due to the developers of the PINY-MD code which we used to perform classical MD simulations.

Helpful discussions with Professor J. M. Stubbs and Professor M. Vladimir on the RRT (regularized resolvent transformation) method are greatly appreciated. I also thank the latter for providing us the program to perform the RRT calculations.

I would like to thank JNCASR for providing me an excellent research facilities, stimulating research ambience, and for the financial support.

I thank JNCASR, CDAC (Bangalore), and CMSD (University of Hyderabad) for computational facilities.

I am grateful to Sagar Sen and Preston Moore for the visualization program.

I specially thank Dr. M. Krishnan for teaching me molecular dynamics techniques and helping me out at various stages of the thesis writing. I thank him for his immense patience, care, and being there at low-tide-times.

I have enjoyed the company and friendship of my present and past lab mates : Dr. M. Krishnan, MDK, Subrata Pal, Sagar Sen, B.L. Bhargava, Saswati, G. Srinivas Raju, Sheeba, Manish C.M., Sunil Kumar, and Chaitanya.

I thank all the staff members of JNCASR for their constant help.

Thanks are also due to all my friends in JNCASR and IISc for their cheerful company and help.

Finally, I am thankful to my parents and family members for their continued support and encouragement.

Preface

The thesis presents the results of investigations on supercritical carbon dioxide ($scCO_2$) and its binary mixture with solutes under varied conditions of density and temperature. Classical molecular dynamics (MD) as well as density functional theory based Car-Parrinello molecular dynamics (CPMD) simulations were employed to characterize the microscopic structure, electronic properties, and the dynamics of these systems.

The importance and characteristic features of environmentally benign solvents in general, and of $scCO_2$ in particular are introduced in Chapter 1. This chapter reviews knowledge of $scCO_2$ and also provides a brief summary of the simulation methods and analyses employed in subsequent chapters.

Comparative studies between CPMD and MD simulations performed on pristine $scCO_2$ under constant temperature and volume conditions are described in Chapter 2. In search of the specific characteristics of $scCO_2$ that makes it attractive for the solvation of a wide range of solutes, investigations on the near neighbour solvent structure and its dynamics are studied. Three dimensional spatial density maps of oxygen atoms around a central CO_2 shows them to preferably occupy positions in the equatorial plane around the central molecule. Data on the dynamics of CO_2 such as mean squared displacement and reorientational time correlation functions are reported. The CPMD calculations show the possibility of CO_2 molecules exhibiting instantaneous geometries that deviate more from linearity than what is expected from simple harmonic vibrational considerations. The chapter also provides probability distributions of molecular induced dipole and quadrupole moments in the supercritical state.

Chapter 3 describes CPMD calculations to probe the effect of system density on the microscopic properties of neat $scCO_2$ along an isotherm. Intermolecular positional and orientational ordering are found to be enhanced with increase in density. Comparisons have been drawn between the intermolecular arrangement at the highest density in the supercritical state and that in the crystal. The effect of density was also observed in the distributions of intramolecular angle of CO_2, and in the development of a cage rattling vibrational mode in the far infra red region.

Chapter 4 presents a study on the solute-solvent interactions in a system containing one perdeuterated ethanol molecule solvated in $scCO_2$ using classical and CPMD simulations. The formation of a electron donor-acceptor (EDA) complex as well as a hydrogen bonded one have been observed. Apart from simulations of the bulk system, CPMD simulations have also been carried out for ethanol-CO_2 clusters in order to compare the extent of these two types of interactions in bulk and gas phases. The calculated vibrational density of states of the bulk system has been compared with experimental data, and the reasons for the splitting in the bending mode of CO_2 are discussed.

Chapter 5 provides the outcome of investigations on the structural, electronic, and dynamical properties of a solution containing a solitary heavy water soaked in $scCO_2$ over a wide range of solvent densities using CPMD simulations. The formation of a hydrogen bond between D_2O and CO_2 is found to be significant at higher densities, while an electron donor-acceptor complex is stable at all densities. Through a Wannier centre analysis, the effective dipole moment of D_2O was found to increase with increasing density. Spectral shifts in the vibrational density of states of D_2O as a function of density are observed. These shifts are consistent with the change in the behaviour of D_2O from a 'free molecule' to one that interacts well with carbon dioxide.

Nomenclature

- BOMD : Born-Oppenheimer molecular dynamics
- CPMD : Car-Parrinello molecular Dynamics
- CFC : Chlorofluorocarbon
- η : Viscosity
- EDA : Electron donor acceptor
- EPM2 : Elementary physical model
- $\triangle G$: Change in Gibbs free energy
- GGA : Generalized gradient approximation
- h : Planck's constant
- H : Hamiltonian
- HOMO : Highest occupied molecular orbital
- HFT : Hellmann-Feynman theorem
- k_B : Boltzmann constant
- KS : Kohn-Sham
- LUMO : Lowest unoccupied molecular orbital
- LDA : Local density approximation
- MD : Molecular Dynamics
- M_I : Mass of I^{th} ion

- MC : Monte Carlo
- MPI : Message Passing Interface
- MSD : Mean square displacement
- NSC : Non-self-consistent
- NMR : Nuclear Magnetic Resonance
- NVT : Isothermal simulations
- ψ_i : ith Kohn-Sham orbital
- P : Pressure
- P_C : Critical pressure
- ρ_C : Critical density
- $\mathbf{r_i}$: Position vector of ith grid in charge cloud
- $\mathbf{R_I}$: Position vector of Ith ion
- R : Universal gas constant
- RDF : Radial distribution function
- RTIL : Room temperature ionic liquid
- scCO$_2$: Supercritical carbon dioxide
- SCF : Supercritical fluid
- T : Temperature
- T_C : Critical temperature
- T_e : Electronic kinetic energy
- TCF : Time Correlation Function
- V : Volume
- VDOS : Vibrational density of states
- XC : Exchange-Correlation

Contents

Chapter 1

Introduction

1.1 Solvation

A solution is the homogeneous mixture of two or more components dispersed at molecular length scales. Solvent is the component of a solution that is present in the greatest amount and can dissolve solid, liquid, or gaseous solutes depending on its chemical properties. In particular, solvation is the association of solvent molecules around an ion or a solute. Some common examples of the application of solvents in our daily life are in food (water), dry cleaning (e.g. tetrachloroethylene), as paint thinners (e.g. toluene, turpentine), glue solvents (e.g. acetone, methyl acetate, ethyl acetate), spot removers (e.g. hexane, petrol ether), detergent (citrus terpenes), perfume (ethanol), and so on. Solvents are generally classified as polar and non-polar, depending on the magnitude of molecular dipole moment. Polar solvents can solvate ions or polar compounds mainly through electrostatic interactions.

Highly polar solutes, for example inorganic salts and sugar (e.g. sucrose), can be dissolved in polar solvent like water whereas non-polar compounds such as oil and wax can be dissolved in a non-polar solvent like hexane. Solute-solvent interactions include hydrogen bonded, electron donor-acceptor, electrostatic, and van der Waals interactions. A schematic description of the near neighbour solvent reorganization around a solute is

illustrated in Figure 1.1. Shown here, is the first solvation shell of solvent molecules (water) when a positively charged aluminum ion (solute) is dissolved in water.

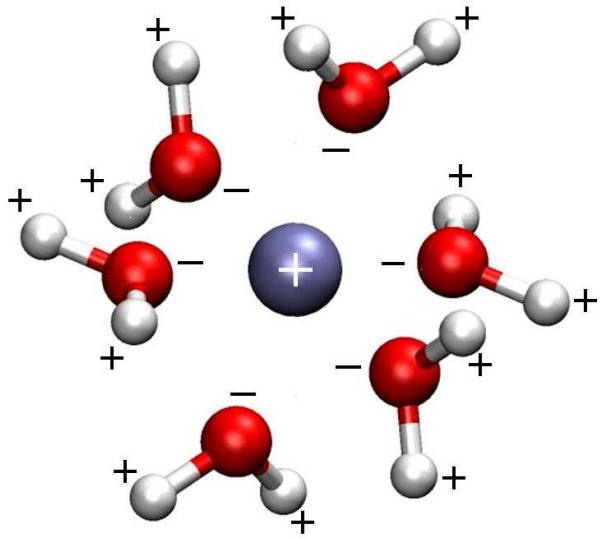

Figure 1.1: **Arrangement of water molecules around aluminum ion (blue sphere) in an aqueous medium. Adapted from Dr. A. Kohlmeyer's homepage (http://www.theochem.ruhr-uni-bochum.de/~axel.kohlmeyer/cpmd-vmd/index.html).**

The change in Gibbs free energy ($\triangle G_{mixing}$) upon mixing two or more components compared to the total free energy when they are separated, is a governing parameter for solubility. Eqn. 1.1 relates this energy change with the chemical potentials of the components [1],

$$\triangle G_{mixing} = G - G^{'} = \sum_{i=1}^{r} n_i(\mu_i - \mu_i^{'}) \tag{1.1}$$

where, n_i is the number of moles of component i; $G^{'}$ and $\mu^{'}$ refer to free energy and chemical potential for pure substance, respectively. The solvation becomes spontaneous when Gibbs free energy is reduced in the mixture, i.e. $\triangle G_{mixing}$ is negative.

When a solute is added to a solvent, the sudden change in the solute charge distribution influences the neighbouring solvent molecules to reorient in such a way that the whole system comes back to equilibrium. This reshuffling of the molecular arrangement and distortion in the solute charge cloud affects the time dependent response of the solvent molecules. A number of theoretical models [2–7] have been developed which can describe

this solvent response in terms of solute-solvent interactions. Some of the models consider the solvent as a linear responding field [8, 9], a Gaussian field, where the field maxima originates from the region of space that is occupied by the solute. On the other hand, as the molecular relaxation time depends on the macroscopic viscosity of the fluid, dielectric relaxation involves a collective process rather than the rotation of a single molecule [10,11]. The solute molecule which is trapped in a partially structured environment may lose its orientation either by rotation of the whole region or by the rotation of individual molecules.

Dielectric relaxation is also found to be guided by the size of both solute (radius, a_M), solvent (radius, a_S), and the radius of the structured region (a_R) surrounding the solute molecule. In general, the dielectric relaxation time (τ) of the solute is a non-linear function of solvent viscosity (η) [12] (as shown in Figure 1.2) and can be written as,

$$\tau = \frac{4\pi a_M^3 \eta_M}{kT} \frac{\eta}{\eta + \eta'} \tag{1.2}$$

with $\eta' = \eta_M (a_M/a_R)^3$, and $\eta_M = \eta_O (a_M/6a_S)$. Note that, when the size of solvent molecule is much smaller than the solute, $a_S \ll a_M$, then $\tau = 4\pi a_M^3 \eta/kT$. Thus, relaxation time is linearly dependent on the solvent viscosity, i.e. Debye behaviour is obeyed. For the reverse situation when $a_M \ll a_S$, τ tends to zero which means that there is no frictional force to the solute and its rotational relaxation rate is inertially controlled. From the above analysis it is evident that the size and shape of solvent as well as solute molecules control the relaxation of a solute in a particular solvent.

Let us consider a situation where the solute and solvent are in equilibrium. An instantaneous excitation of the solute from ground electronic state to the excited state will force the surrounding solvent molecules to relax to a new equilibrium with the excited state of solute molecule. Ultrafast spectroscopic experiments [13–15] can probe this solvent

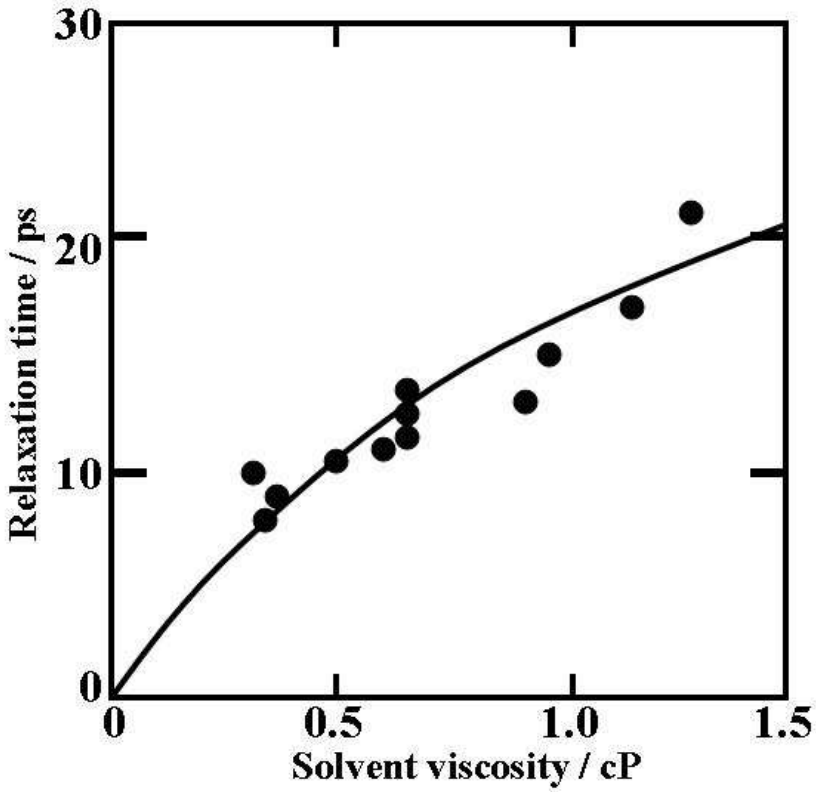

Figure 1.2: **Plot for dielectric relaxation time (τ) against viscosity for the nitrobenzene solutions. The solid line is derived from the eqn. 1.2. Adapted from Ref [12].**

relaxation which measures the relaxation correlation function, S(t),

$$S(t) = \frac{\omega(t) - \omega(\infty)}{\omega(0) - \omega(\infty)} \tag{1.3}$$

$$\hbar\omega(t) = \hbar\omega(0) + \triangle E(t) \tag{1.4}$$

where, ω(t) represents the time dependent fluorescence frequency and $\triangle E(t)$ is the change in solvation energy caused by the change in charge distribution between ground state and excited electronic state due to insertion of solute molecule. $\triangle E(t) = \int \mathbf{dr}\mathbf{P}(\mathbf{r},t)\cdot\triangle\mathbf{D}(\mathbf{r},t)$ relates the extent of solute-solvent interactions in the induced polarization ($\mathbf{P}$($\mathbf{r}$,t)) of solvent and the change in electric field ($\triangle$ $\mathbf{D}$($\mathbf{r}$,t)) due to change in charge distribution in solute.

Apart from the relaxation correlation functions, spectroscopic measurements efficiently

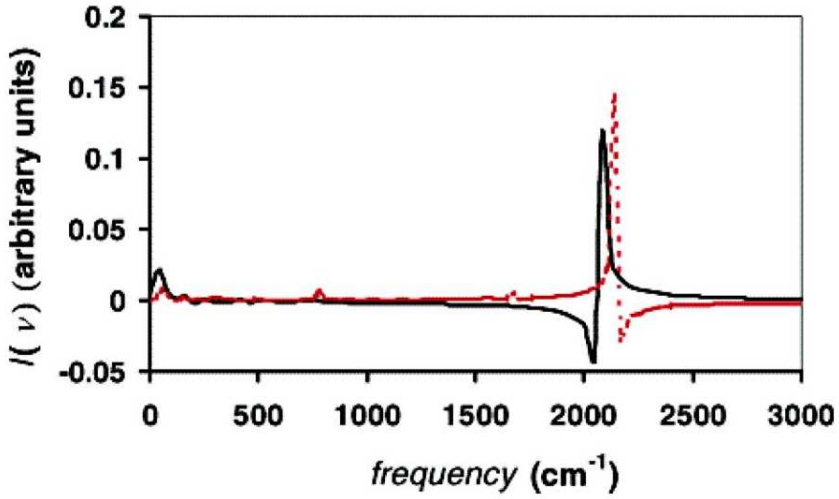

Figure 1.3: **Simulated power spectra of azide ion in anti-symmetric stretching region in two environments, D_2O (solid line) and carbonic anhydrase (dashed line). Adapted from Ref [16].**

probe the environmental effect on the fundamental vibrational modes of a particular molecule. In some molecules, the formation of a hydrogen bonded complex influences blue shift in the bending mode of a molecule with respect to that in the monomeric phase. This phenomenon has been observed in the case of water which is reported to be due to the relative weakening of intramolecular covalent bond upon formation of hydrogen bond [17]. With the advent of computer simulation techniques, the experimental observables can be calculated by molecular dynamics (MD) or Monte Carlo (MC) methods. Figure 1.3 shows the simulated vibrational density of states of azide ion in two different solvents, water and carbonic anhydrase [16]. The electronic structure of azide ion in gas phase is the mixture of three resonance structures and it falls into $D_{\infty h}$ symmetry group. This resonance structure gets perturbed due to formation of hydrogen bond with the solvent (H_2O or D_2O) in aqueous medium which causes a blue shift in the anti-symmetric stretching mode of water. The simulated results compare well with experiment where the anti-symmetric stretching modes appear at 1987 cm^{-1} in gas phase and 2049 cm^{-1} in aqueous medium [18].

A reverse spectral shift is observed due to the formation and dielectric enrichment of the solvation shell around solute molecules instead of hydrogen-bonded interactions. In

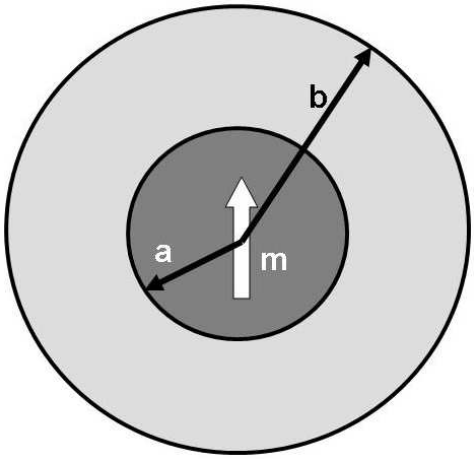

Figure 1.4: **Effect of electron-donor acceptor interaction on the dipole moment vector (m) of a polar solute in binary solvent mixture. Gray region represents first solvation shell formed by more polar solvent molecules with the radius 'b' around the cavity (black region) of radius 'a' which contains solute molecule. Adapted from Ref [20].**

the case of binary mixtures of solvents those strongly differ in their dielectric constants, the more polar solvent molecules replace the less polar solvent around a polar solute (Figure 1.4). The solute-solvent electron-donor acceptor interaction results in the shift of solute vibrational frequency towards lower frequency (red-shift) compared to its pristine state [19, 20].

Thus, the above mentioned experimental and theoretical techniques are useful in understanding solvation.

1.2 Role of solvent in environmental pollution

Chemical industries are the most responsible for environmental pollution for their smoking chimneys, drainage of the hazardous wastes in rivers, and the risk of fire or explosion. Water is the 'universal' solvent that is commonly used in industries. The aqueous affluent from industries are drained into river or local stream without being treated which in turn causes water pollution. In addition, the fibrous materials like poly(amides), cotton and polyesters absorb a huge amount of water restricting the recycling of the solvent.

Generally, the extraction of dissolved solutes from water becomes difficult due to its high boiling point and also this is expensive.

Removal and extraction of solvent from the products is relatively easier for volatile solvents though evaporation leads to the environmental pollution. Organic solvents are used in paints, varnishes, lacquers, industrial cleaners, printing inks, etc. The alarming disadvantage of the use of organic solvents is that they contaminate our air, soil, and water as most of these solvents are toxic and flammable. For the purpose of dry cleaning, a compound namely perchloroethylene is used which can damage the nervous system, liver and kidneys. Some organic solvents that are used for coatings and cleaners are toxic [21–24] and air pollutants, with very low vapour pressure. For example, methylene chloride is used for the extraction of caffeine from coffee beans and also in the production of photographic film. This is a hazardous substance [25] which may cause even skin cancer. The alternative solvent which is more promising for caffeine extraction [26–29], retaining the flavour of coffee intact, is supercritical CO_2 which is a 'green solvent'.

In recent years hydrochlorofluorocarbons (HCFCs) are employed as alternatives to CFCs (Chlorofluorocarbon) because chlorofluorocarbons are toxic, carcinogenic, and implicated in the depletion of the earth's ozone layer [30]. These substances possess properties similar to CFCs, e.g. high density, high dielectric strength, thermal stability, chemical stability, and non flammability. Although HCFCs are less hazardous than CFCs, they are expensive which restricts the use of these solvents in large scale industrial applications as industries also demand 'practical benefits and economic viability'. Thus, a more effective solvent is needed to fetch success in this area.

1.3 Green solvents

The growing need for more environmentally benign chemical processing has focused attention on the search for 'green' or 'sustainable' solvents [31–35]. An useful measure of a 'green' solvent would be the efficiency with which it can replace toxic/hazardous organic

solvents, its ability to process industrial wastes before rejecting to environment, extraction of useful chemicals, and, last but not the least, the capacity to recycle the solvent. Currently, two classes of 'green' solvents [36–38] are known: (1) Supercritical CO_2 and (2) Room temperature ionic liquids (RTIL). Ionic liquids, combining organic cations and inorganic anions, are molten salts at or near room temperature. This class of solvents are useful in biphasic catalysis [39, 40], liquid/liquid extraction [41, 42], fuel and solar cells [43–45], and so on. The physical properties of ionic liquids such as density, melting point, viscosity, and hydrophobicity can be adjusted by the variation of cations and anions that lead to dissolve a solute depending upon the concentration of ions.

Substance	$\mathbf{T}_c$ (K)	$\mathbf{P}_c$ (bar)	ρ_c (g/cc)
Ar	150.9	48.98	0.536
CH_4	190.5	46.04	0.162
Kr	209.4	55.0	0.919
C_2H_4	282.3	50.41	0.214
Xe	289.7	58.4	1.11
C_2F_6	293.0	30.6	0.622
CO_2	304.1	73.7	0.468
N_2O	309.6	72.5	0.452
H_2O	647.1	220.6	0.322

Table 1.1: Critical parameters for some substances. Adapted from [52]

Another class of 'green solvents' is 'supercritical CO_2'. Supercritical CO_2 is currently being realized as environmentally friendly, non-toxic, abundant, and tunable solvent in a variety of purposes [46,47] starting from polymer processing and production [48], cleaning

protocols in microelectronics [49], extraction [27] of different solutes, chemical and materials processing [50], catalysis [51] to nanotechnology. Beyond a certain temperature (T_c) and pressure (P_c), a substance can exist in a supercritical state that possesses properties of both a liquid and a gas. This is the state in which the density of the substance is higher than that of the gas with enhanced diffusivity and reduced viscosity than liquid. The liquid and gas first order transition line ends at a 'critical' point and the state beyond critical point is 'supercritical state'. For some substances, the potential to dissolve the solutes increase in supercritical state than in liquid state. Critical parameters for few substances which are useful as supercritical fluids are listed in Table 1.1. In order to understand the properties of supercritical fluids and also to enhance the solvation capabilities for a wide range of solutes, molecular level studies are necessary. Various techniques have been employed to investigate the molecular structure and dynamics of these fluids by experiments [52] as well as by computer simulations. Let us now discuss the microscopic description of a fluid beyond critical point.

1.4 Supercritical Fluids ($ScCO_2$)

Attractive forces between two molecules in a low density system can cause the association of molecules when their relative velocity is low. This association of molecules is known as condensation which can be enhanced at high densities. However, density is not the only variable that drives condensation. At high temperatures the relative velocities between molecules are also high, and condensation can not occur in such a situation, irrespective of the density of the system. Thus, for every system there lies a particular temperature and pressure above which system can not be condensed. This temperature and pressure are known as 'critical temperature (T_C)' and 'critical pressure (P_C)' respectively. The existence of critical temperature was first demonstrated by Baron Charles Cagniard de la Tour in 1822. He heated a liquid in a closed container and observed that the vapour-liquid interface vanishes after a particular temperature was reached (as shown schematically in

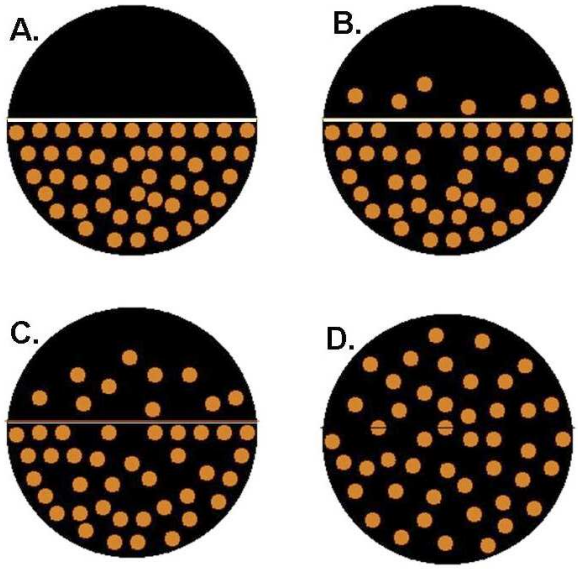

Figure 1.5: **Conceptually simplistic representation of the gradual transformation from liquid to supercritical state of a substance in a confined vessel with increasing temperature. The liquid-gas interface is shown by white line. Phase (A) symbolizes pure liquid and upon heating, the molecules (gray circles) from liquid diffuses to the vapour (B, C) giving rise to 'supercritical' phase in (D).**

Figure 1.5), i.e. boiling of a liquid does not occur in a closed vessel. Figure 1.6 shows the schematic representation of the phase diagram of a substance. pressure increases the density of vapour. Under certain pressure and at a fixed temperature, the interface between the two phases vanishes. This is the 'supercritical state' of a system. The disappearance of meniscus is known as 'opalescence'. Along the liquid-vapour coexistence

	Liquid	**Supercritical state**	**Gas**
Density (g/cc)	1	0.05 - 1	10^{-3}
Viscosity (Pa.s)	10^{-3}	10^{-4} to 10^{-5}	10^{-5}
Diffusion coefficients (cm^2/s)	10^{-5}	10^{-3}	10^{-1}
Surface tension (mN/m)	20 - 50	0	0

Table 1.2: Comparison between physical properties of a substance at gas, liquid, and supercritical state. Adapted from ref. [53]

curve, the pressure of the system increases when temperature increases. The thermal expansion of the liquid decreases its density and the resulting higher pressure increases the density of vapour. Under certain pressure and at a fixed temperature, the interface

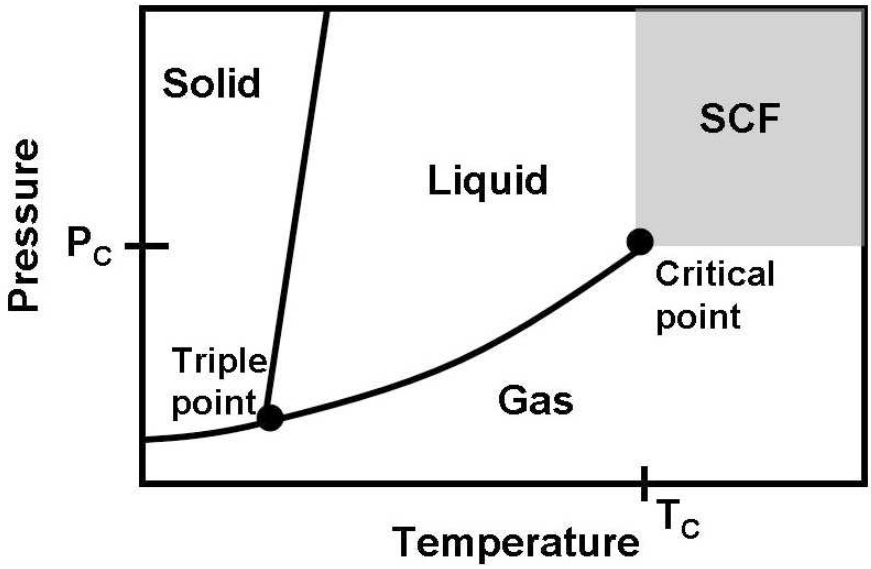

Figure 1.6: **Schematic phase diagram of a substance showing triple point, critical point and supercritical phase (shaded region).**

between the two phases vanishes. This is the 'supercritical state' of a system. The disappearance of meniscus is known as 'opalescence'. The shaded region in the phase diagram (Figure 1.6) is the 'supercritical region'. Supercritical fluids exhibit important

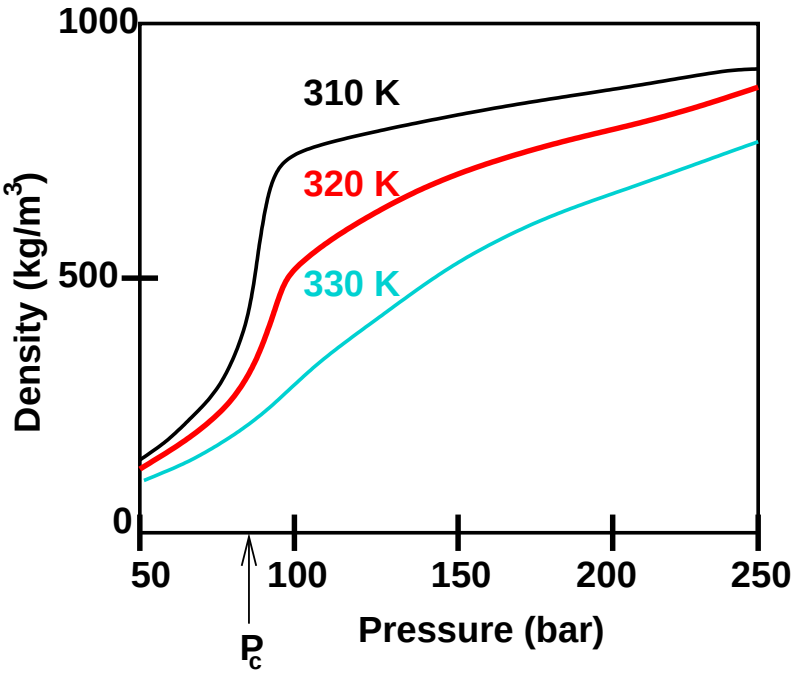

Figure 1.7: **Density vs pressure curves for $scCO_2$ along three isotherms. Adapted from Ref. [54].**

properties like compressibility, diffusivity, homogeneity, and a continuous change from gas-like to liquid-like properties. The comparison of different physical properties of a substance in gas, liquid, and supercritical state is given in the Table 1.2. Note that the density of the substance in supercritical state is much higher than that in gas and can even be doubled by a moderate increase in system pressure. Tunability of the properties of these fluids with temperature and pressure is one of the most attractive features for solvation. Figure 1.7 shows this behaviour of carbon dioxide in supercritical state along three isotherms. On the other hand, intermolecular radial distribution function (RDF) sheds light on the change in molecular arrangement due to varying thermodynamic quantities of the system. The progressive evolution of RDFs obtained from X-ray scattering experiments for CO_2 while going from liquid to supercritical state is shown in Figure 1.8. Oscillation of the RDF for liquid CO_2 around the zero line implies a pseudocrystalline structure in the local region around a central molecule whereas, the same shows long-range correlation in supercritical state.

1.5 Supercritical CO_2

In its electronic ground state, carbon dioxide is a linear molecule with $D_{\infty h}$ symmetry. In atmosphere, CO_2 is present in a small quantity (0.033%) and plays a vital role in the earth's environment as a necessary ingredient for life cycle. At normal temperature and pressure, this compound is a gas and its phase diagram is shown in Figure 1.9. Beyond the critical point at $T_c = 31.1^oC$, $P_c = 73$ bar, and a critical density ρ_c of 0.467 g/cc, in the supercritical phase this compound gains some interesting properties which makes it useful as a solvent for various purposes. One of the applications of supercritical CO_2 is in nanomaterial synthesis [53, 55–58] where the size of the nanocrystals can be changed by regulating solvent density which in turn tunes the steric repulsion between particle cores. $ScCO_2$ is also used in asymmetric catalytic hydrogenation reactions [59, 60] for the manufacture of trimethyl cyclohexanone [61]. Relative to conventional solvents, higher

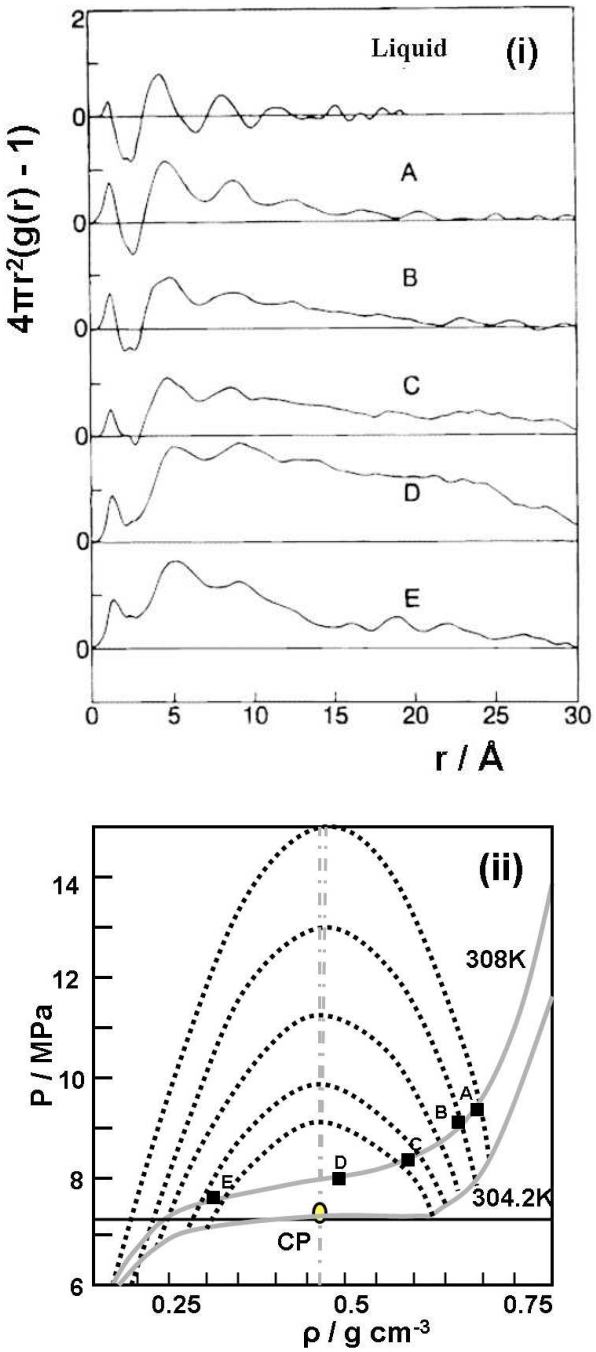

Figure 1.8: **(i) Radial distribution functions of the form $4\pi r^2(g(r) - 1)$ of liquid and supercritical CO_2 obtained from X-ray scattering experiments. (ii) Phase diagram of CO_2 where the line of maximum fluctuation is shown by the gray dashed lines on the P-ρ diagram. These lines start from the critical points (CP) and extends upwards. The fluctuation contours are shown in dotted lines. The index of the plots A-E in (i) are state points indicated in the phase diagram of CO_2 in (ii) along a isotherm at 308K. Adapted from Ref. [62].**

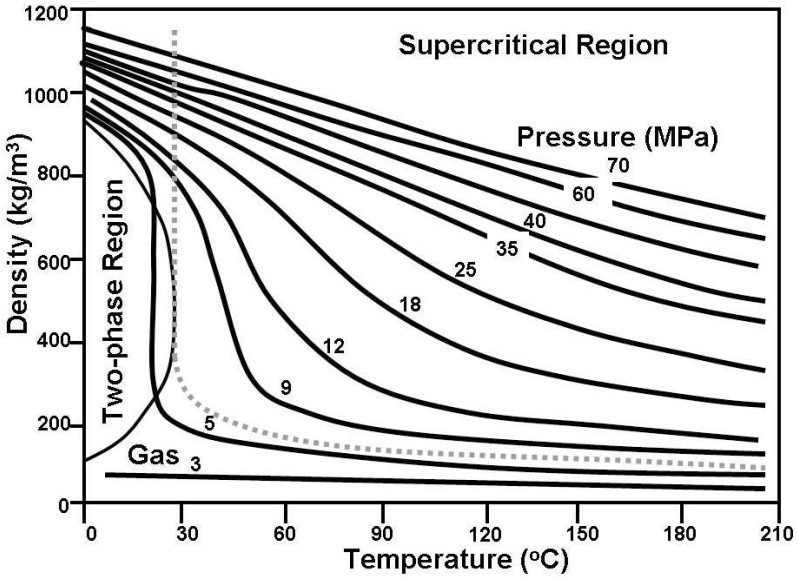

Figure 1.9: **Phase diagram of CO_2. Adapted from Ref [63]**

enantioselectivities can be achieved in $scCO_2$ due to the miscibility of this solvent with hydrogen which results in high diffusion rates providing enhanced reaction rates. Another important utility of this solvent lies in the area of bioconversion [64–68] as some enzymes are more stable in $scCO_2$ than in water. It has been shown that enantioselectivity in $scCO_2$ can be tuned by adjusting the temperature and pressure [69].

In comparison to the liquid medium, $scCO_2$ is much more compressible with large free volumes which enables the attractive forces in the solvent to push the solutes in energetically minimized positions. As a consequence, the local environment around a solute molecule in $scCO_2$ comes to be distinct in density and composition than that of bulk. This enhanced solvent density around the solute reduces the solute-solute interactions giving rise to the 'cage effect' [70, 71]. Some liquid phase reactions can be explained by this effect.

Analytically, the solvatochromic effect can be interpreted by dielectric continuum model. In some systems, where site specific solute-solvent interactions play crucial role, this model is not sufficient enough to capture the microscopic details of the solvation process. Although CO_2 is a nondipolar compound due to its molecular symmetry ($D_{\infty h}$), the partial charges on the individual atoms result in non-zero bond dipole moments which

produce a significant quadrupole moment, making $scCO_2$ a 'quadrupolar' solvent [72, 73]. Raveendran and Wallen have demonstrated [74,75] that CO_2 can be considered as a charge separated polar molecule to its near neighbours while the resultant dipole moment is zero for distant molecules. This can be well understood from an analysis of its electronic polarizability (α), which is a measure of the 'softness' of the charge cloud around a molecule. Typical polarizabilities of different molecules are given in Table 1.3.

Molecule	α **(Å^3)**	$\alpha_\parallel - \alpha_\perp$ **(Å^3)**
H_2	0.819	0.314
D_2	0.809	0.299
N_2	1.77	0.70
CO	1.98	0.53
O_2	1.60	1.10
HCl	2.60	0.311
CO_2	2.63	2.10
NH_3	2.22	0.288
Cyclopropane	5.64	-0.81
Benzene	10.4	-5.6
CH_3Cl	4.53	1.55
$CHCl_3$	8.50	-2.68

Table 1.3: **Polarizabilities and anisotropies of polarizabilities of neutral molecules in their ground states [1, 76].**

The polarizability of neutral CO_2 (2.63 Å^3) in its ground state is much higher than that of CO (1.98 Å^3) and is comparable with that of HCl (2.6 Å^3). The overall higher anisotropy in polarizability of CO_2 with respect to CO and HCl indicates the possibility of distortion in its geometry due to solvent-solvent and solute-solvent interactions. The absence of a permanent dipole moment in CO_2 makes it Raman inactive in the isolated state despite the strong Fermi-coupled ν_1 (symmetric stretching), $2\nu_2$ (first overtone of bending mode) doublet. Interestingly, this doublet can be observed in pressurized CO_2 [77] due to collision induced absorption (CIA). Based on the CIA spectra of CO_2, Vigasin et al. [78–80] have demonstrated that the thermally averaged rotational constants in CO_2

dimer are different from the ground state. In other words, a thorough study of CIA spectra can provide insights into molecular interactions.

There have been a large number of experimental [81–83] studies on the viscosity (η) of CO_2 along different isotherms and isobars. Figure 1.10 shows that the viscosity increases rapidly near critical point ($T_c = 31.1^oC$) whereas beyond the critical point it decreases with increase in temperature at a constant pressure. In contrast, the same has $T^{1/2}$ dependency in low density gas phase. Although the density of $scCO_2$ is much lower than that in liquid, some solid solutes [84–86] can be dissolved in $scCO_2$.

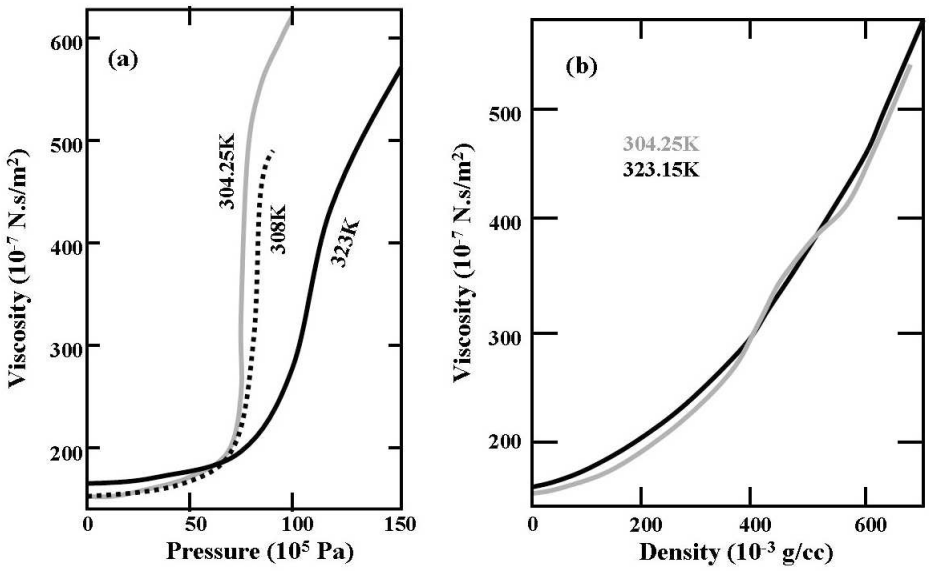

Figure 1.10: **Dependence of viscosity with (a) pressure and (b) density of carbon dioxide along different isotherms. Adapted from ref. [83]**

The dynamics of a molecule is characterized by the kinematic viscosity (η/ρ) which is the ratio of viscosity to the density of the fluid. As fluid density in supercritical state is two orders of magnitude higher than that of gas, the kinematic viscosity of the fluid is much lesser than the gas phase. Thus, in supercritical region the fluid attains higher diffusivity than in liquid. This specific property can be attributed to accelerate the mass transfer reactions under supercritical region. Supercritical CO_2 acquires higher thermal conductivity than in gas phase which results in easier heat removal in highly exothermic reactions where temperature control is imperative for selectivity and product stability [60].

1.6 Binary mixtures

The major disadvantage of supercritical CO_2 as a solvent is its lesser potential to dissolve polar compounds including water [87]. One way to address this issue is through the use

Substance	$\mathbf{T}_c$ (K)	$\mathbf{P}_c$ (bar)	Characteristics
Methanol	513	81	Increases the polarity
Ethanol	514	61	”
2-Butanol	536	42	Chirality
Acetone	508	47	Increases the polarity [88]
Acetonitril	546	48	Totemerism [89]
Acetic acid	593	58	Extraction [90]
Chloroform	536	54	Totemerism [hydrogen bond] [89]

Table 1.4: List of modifiers that are used in supercritical carbon dioxide [91]

of binary mixtures of supercritical CO_2 (component 1) with polar co-solvents (component 2). Depending on the molar mass and critical temperature of component 2, the binary mixtures are classified into two types : when both the properties of component 2 are (i) slightly higher than the component 1, and (ii) much higher than the component 1. The first type of mixture is used as reagent and also to enhance the solvation properties of supercritical fluid. Thus, the co-solvents in this category are known as ‘modifiers’. Whereas, the second type of mixtures are applicable mostly for dissolving solutes of high molar mass in the process of extraction, separation, and chemical reactions. The substances that are used as modifiers are listed in Table 1.4. The asymmetry in the physical properties of the solvent and co-solvent, such as size, shape, interaction strength, and polarity gives rise to interesting characteristics of the supercritical binary mixtures. These compressible fluids are very sensitive to the change in composition and it has been

shown that above the critical point of the mixture, the solubility of a solute increases with pressure along an isotherm and it decreases with temperature along an isobar [92].

Typical co-solvents are alcohols, acetone, water, small chain fluorocarbons, and so on. For example, the chemically homogeneous anionic phosphate fluorosurfactants enable the uptake of water in CO_2, forming Water/CO_2 microemulsions [93–95]. Polar solutes with very less solubility in pure CO_2 can be dispersed into these water-rich regions of the microemulsion. Specific intermolecular interactions such as hydrogen bonding and the attractive forces due to dipole-quadrupole coupling between the co-solvent and solute molecules trigger higher solvation of the polar compounds. Following this concept, binary mixtures of $scCO_2$ and chelating compounds, e.g. acetylacetone and dithiozones, can even be extended to extract heavy metals from a solution [96]. On the other hand, addition of

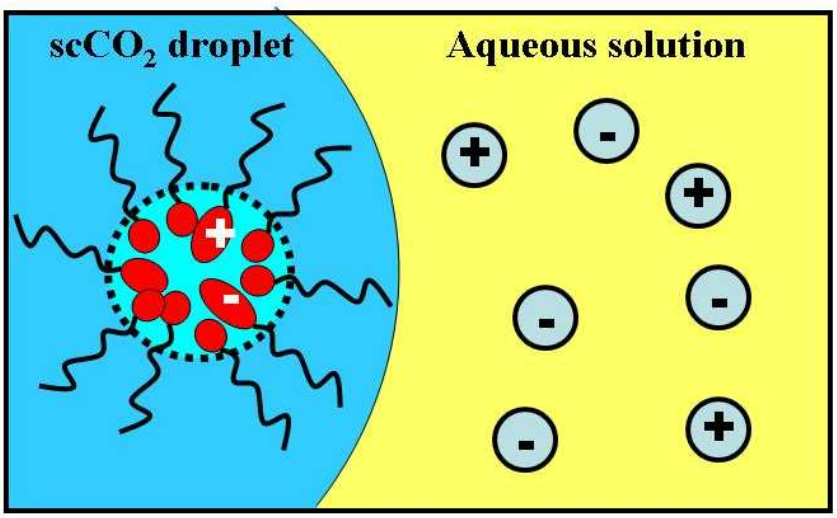

Figure 1.11: **Extraction of highly polar guests from a solution by the aid of fluorinated dendrimer dissolved in $scCO_2$. Adapted from Ref [97]**

fluorinated dendritic polymers in $scCO_2$ enhances [48] the solubility of polar compounds. These dendrimers are highly branched and non-polar. Although they are soluble in $scCO_2$, the inner core of this micelle is polar in nature and can trap the polar guests from the aqueous solutions. Figure 1.11 is a cartoon of this process in simplified manner. Along with the 'smart' molecules, this supercritical fluid mixture can replace environmentally damaging solvents such as freons or chlorinated organic solvents in various purposes.

Several experimental evidences illustrate the local solvent density enhancement around a solute. The local environment gets more denser when a polar co-solvent has been added in small concentration to the solvent [98]. It is known that Gibbs free energy (△G) gives

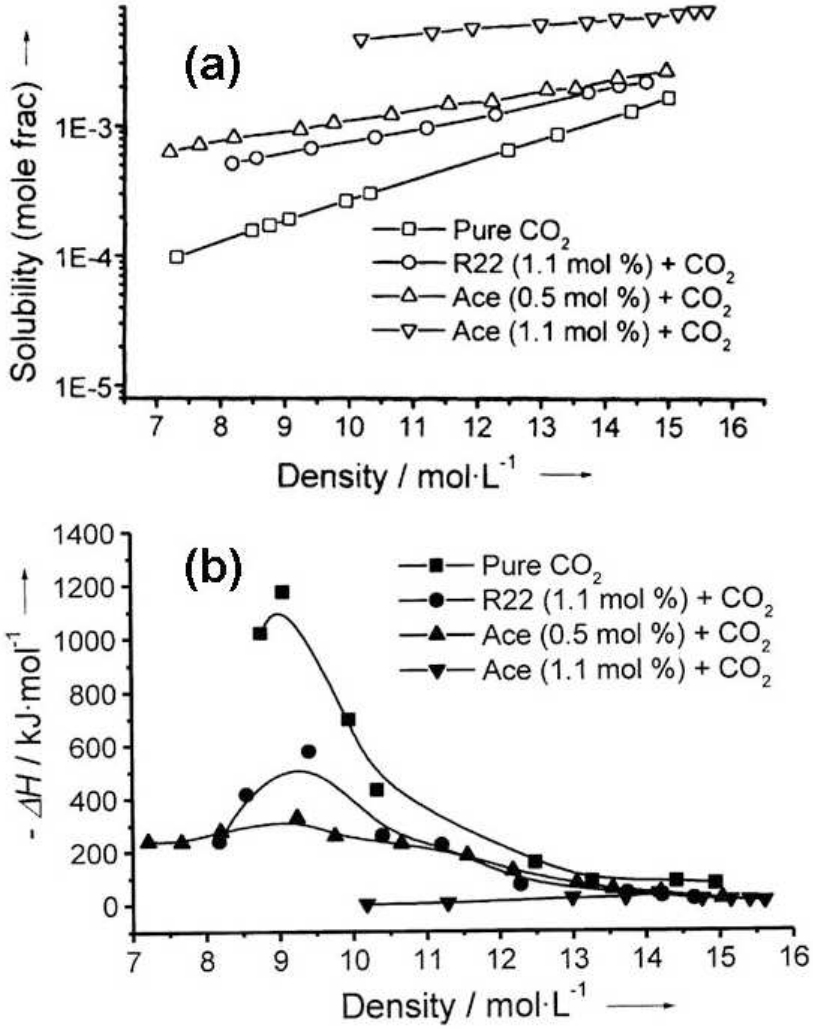

Figure 1.12: **Dependence of (a) solubility (of solute), and (b) enthalpy (of the solution) of 1,4 napthaoquinone in scCO$_2$, CO$_2$/CHClF$_2$ (R22), and CO$_2$/acetone at 308.15K [98] on the solvent densities.**

the measure of solubility [1]. The thermodynamic condition between Gibbs free energy, enthalpy (△H), and entropy (△S) is as follows,

$$\triangle G = \triangle H - T\triangle S \tag{1.5}$$

$$\triangle S = \frac{\triangle H - \triangle G}{T} \tag{1.6}$$

The calorimetric studies [98] of binary mixtures in $scCO_2$ show that the solubility of a solute and the absolute enthalpy of a solution increase with the addition of co-solvent. For example, an order of magnitude increase in solubility of 1,4 napthaoquinone in binary mixture of acetone/$scCO_2$ can be observed in comparison to that in pristine $scCO_2$ (Figure 1.12). Thus, analyzing the experimental results and the above equations, one can conclude that increase in solubility with the addition of co-solvent is due to the enhancement of entropy. As the solute-solvent and solute-co-solvent interactions are stronger than solvent-solvent interaction [99,100], the solvent and co-solvent density around a solute can even be factors of magnitude higher than the bulk density [101]. The increase in entropy is caused by the replacement of CO_2 molecules by the co-solvents molecules in the solvation shell. The stepwise rearrangement of these components in the solution is shown in Figure 1.13.

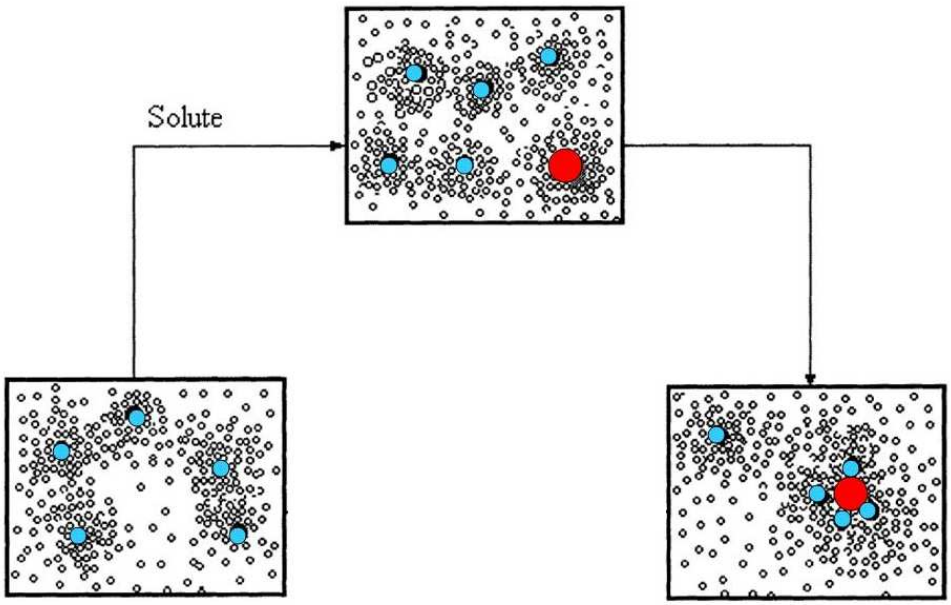

Figure 1.13: **Conceptually simplistic representation of 'clustering' in a binary supercritical fluid mixture; solvent (open circle), co-solvent (blue cricles), solute (red circle). Adapted from ref. [98]**

Among the binary mixtures of CO_2/Acetone, and $CO_2/CHClF_2$, acetone is more efficient in solvation than the other due to its higher dipole moment. Spectroscopic measure-

ment [99] suggests that significant contribution to solubility also comes from the hydrogen bonding network between solute, solvent, and co-solvent in the vicinity of the solute.

In summary, supercritical CO_2 is treated to be an efficient solvent due to the following characteristics,

1. It is an environmentally friendly solvent as $scCO_2$ is non-toxic, non-flammable, and recyclable. In some situations this solvent is more useful with added modifiers than the pure substance.

2. $ScCO_2$ posses favourable physical properties for solvation.

3. It is highly sensitive to the change in temperature and pressure. The density of the solvent can even be doubled by minute change in pressure [54].

The above mentioned interesting properties and applications of supercritical CO_2 have motivated the investigation of a molecular level description of this solvent. This thesis discusses the solvent structure and dynamics in supercritical CO_2 and the effect of pressure on its physical properties. Binary mixtures of ethanol/CO_2 and water in CO_2 have also been studied. Results reported in this thesis have been obtained by using both *ab initio* and classical molecular dynamics simulations. In the following section, a brief description of the Car-Parrinello molecular dynamics technique [102] is presented for the sake of completeness.

1.7 Car-Parrinello Molecular Dynamics

There exists several excellent reviews of this technique [103–117]. Here, the basic principles are discussed. Condensed matter systems can be well studied using classical molecular dynamics simulations [118–131]. The interactions between different species in a system can be divided into two-body, three-body, and many body, long range and short range contributions. In most of the cases, these potential parameters are 'predefined' depending on experimental studies or independent electronic structure calculations. Generally, the

total potential energy [132] can be written as,

$$\begin{aligned} U(\overrightarrow{r}) &= \sum_{bonds} K_b(b-b_0)^2 + \sum_{angle} K_\theta(\theta-\theta_0)^2 + \sum_{dihedrals} K_\chi(1+cos(n\chi-\delta)) \\ &+ \sum_{nonbond} 4\epsilon_{ij}\left[\left(\frac{\sigma_{ij}}{r_{ij}}\right)^{12} - \left(\frac{\sigma_{ij}}{r_{ij}}\right)^{6}\right] + \sum \frac{q_i q_j}{4\pi\epsilon_0 r_{ij}} \end{aligned} \tag{1.7}$$

where, i, and j are particle indices; b_0, and θ_0 are equilibrium bond length and bend angle respectively; K_b, K_θ, and K_χ denote bond stretching, bending, and dihedral angle force constants respectively; ϵ_0 is the permitivity of free space; and r_{ij} is the distance between ith and jth particles with corresponding partial charges q_i, and q_j, respectively. Lennard-Jones and Coulomb terms represent the external non-bonded interactions.

In spite of the overwhelming success, this method cannot be used for 'complex chemical' systems where realistic bond breaking and formation and in general where transferability of the potential between different chemical systems and studies of systems under varied thermodynamic conditions are demanded. Thus, an advanced technique is needed to study the system where the electronic structure and bonding pattern changes in the course of the molecular dynamics trajectory. The extended technique which couples traditional molecular dynamics and electronic structure method is "*ab initio* molecular dynamics" [103–117]. *Ab initio* molecular dynamics (AIMD) is also known as Car-Parrinello (CP), Hellmann-Feynman, first principles, quantum chemical, on-the-fly molecular dynamics.

Such *ab initio* calculations involve quantum part dealing with the electronic degrees of freedom and another, classical dynamics of the ions. The foundation of AIMD is the Born-Oppenheimer approximation, also known as adiabatic approximation, which separates the electronic degrees of freedom from that of ions, exploiting the mass difference between the two. Due to the large mass difference between the electron and ions, their time scales for evolution are also well separated. In CPMD, both the electronic and ionic parts are evolved with respect to time using Newton's equations of motion. Time

evolution of ions keeping the electrons at its ground state is the main feature of AIMD simulations. CPMD [102] simulation is based on the Hohenberg-Kohn-Sham density functional theory [133–135] (DFT) for electronic structure within a plane wave pseudopotential [136–144] implementation. The details of CPMD approach will be discussed in the following sections.

1.7.1 Simulated annealing

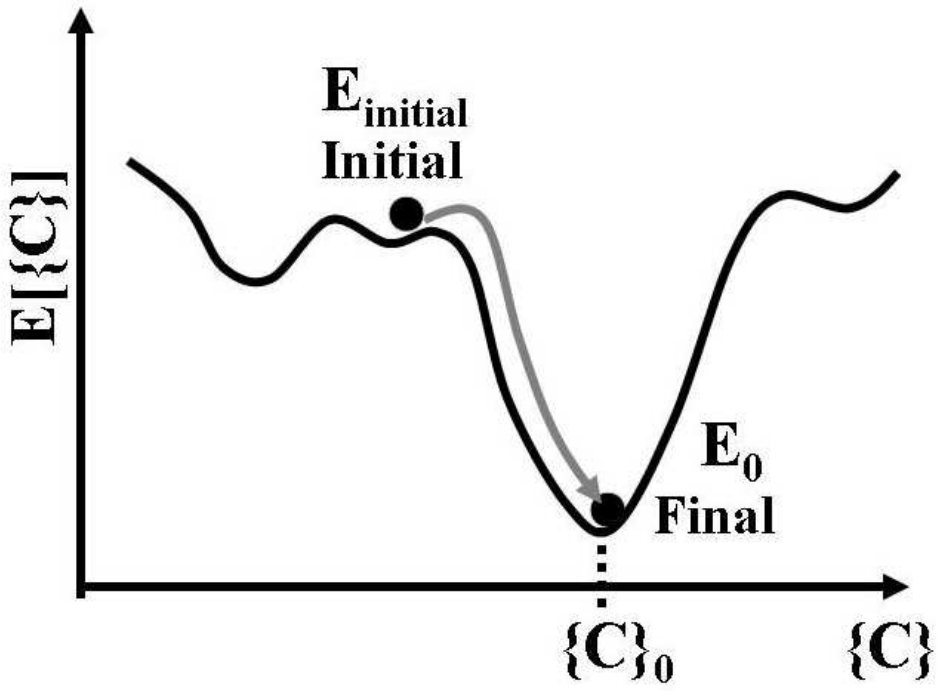

Figure 1.14: **Schematic representation of simulated annealing and the evolution of the Kohn-Sham energy functional E[{C}] from an initial higher energy state ($E_{initial}$) to its ground state E_0.**

Bloch's theorem [145] states that in a periodic system each electronic wave function can be expanded in terms of plane wave basis sets,

$$\psi_i(\vec{r}) = \sum_k C_k^i e^{\vec{k}\cdot\vec{r}} \tag{1.8}$$

where, C_k^i's are the coefficients of expansion. A particular set of these co-efficients represent a state point in the multidimensional space. According to the Born-Oppenheimer approximation, the electrons must be maintained at the ground state with respect to ions, i.e. electronic wave function should be optimized accurately to nuclear position, as the nuclear configuration evolves in time. If electronic wavefunction is not optimized up to a desired accuracy, energy will continuously flow between electrons and nuclei which will lift electrons to excited states. In such a situation, the adiabatic nature of electronic and nuclear dynamics will be violated. Simulated annealing (see Figure 1.14) is a methodology by which the energy of a system is minimized starting from a higher energy state. Annealing means slow decrease or increase in temperature. Here, temperature is synonymous to fictitious kinetic energy of electrons.

The rate at which the coefficients will scroll through the configuration space is denoted as 'coefficient velocity', $\dot{C}_k^i = \frac{dC_k^i}{dt}$.
Here, 't' is not the usual time rather it is some variable on which C_k^i's are dependent. The kinetic energy term in Lagrangian can be written as,

T = $\frac{1}{2}\mu \sum_i \sum_k (\dot{C}_k^i)^2$, μ is arbitrary inertia of mass that controls the speed and character of the motion through coefficient space. And,

V = $\mathrm{E}_{KS}\{C_k^i\}$, E_{KS} is the Kohn-Sham energy functional
also, wave functions must satisfy the orthonormality constraint equations,

$$\sigma_{ij} = \frac{1}{V}\int_{\mathrm{v}} d\vec{r}\psi_i^*(\vec{r})\psi_j(\vec{r}) - \delta_{ij} \tag{1.9}$$

where, V is the cell volume.
The time evolution of electronic degrees of freedom are governed by the following Lagrange equations of motion,

$$\frac{d}{dt}\frac{\partial L}{\partial \dot{C}_k^i} - \left(\frac{\partial L}{\partial C_k^i}\right) = 0 \tag{1.10}$$

Thus, combining equation 1.9 and 1.10 we get,

$$\mu \ddot{C}_k^i = -\frac{\partial E_{KS}}{\partial C_k^i} - \sum_j \lambda_{ij} \frac{\partial \sigma_{ij}}{\partial C_k^i} \tag{1.11}$$

where, λ_{ij} is Lagrange multiplier. The first term on the right hand side is the force acting on C_k^i's to minimize the energy of the wavefunction, and the second term is that due to constraints. Convergence of the wave function can be controlled by choosing appropriate values of μ, and time step [146] and the coefficients, C_k^i, can be time evolved using the velocity Verlet alogorithm [147].

1.7.2 CP equations of motion

The CPMD method is a parametric propagation of the electronic ground state with the displacement in the ionic position rather than solving the self consistent equation, i.e. optimization of the wavefunction at each time step. The adiabatic approximation fails in systems where the gap between conduction and valence bands is such that the lowest electronic transition frequency is comparable or smaller than the highest phonon vibrational frequency. For example [105], in a system consisting of eight silicon atoms, the lowest occurring frequency in vibrational density of states for the electronic degrees of freedom is much higher than the highest-frequency phonon mode of ions, which satisfies the criteria for the application of the CPMD method. Figure 1.15 shows comparison between these two density of states. Finally, for a chosen set of parameters the electronic and ionic subsystems should be dynamically well separated.

The ionic potential energy within the pseudopotential implementation of the local density approximation (LDA) [134] in the Kohn-Sham (KS) scheme can be written as,

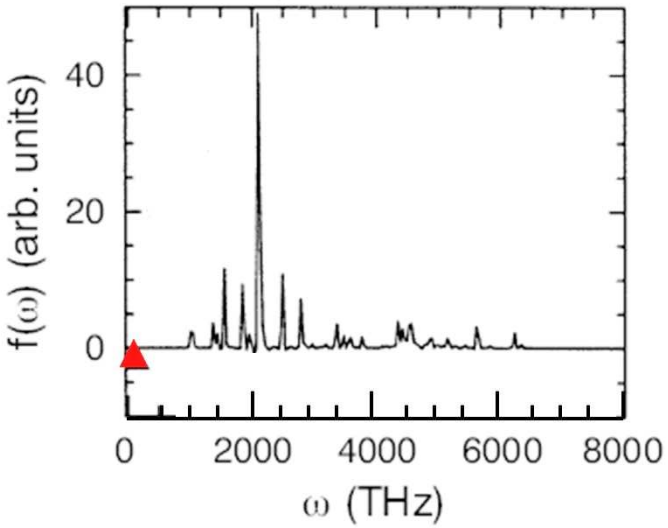

Figure 1.15: **Vibrational density of states of the electronic degrees of freedom compared to the highest-frequency phonon mode (triangle) for a model system. Adapted from Ref [105].**

$$
\begin{aligned}
E_{KS}[\{\psi_i(\overrightarrow{r})\}] &= \sum_i f_i \int \psi_i^*(\overrightarrow{r}) \left(\frac{-1}{2}\nabla^2\right) \psi_i(\overrightarrow{r})\mathbf{dr} \\
&+\frac{1}{2}\int\int \frac{\rho(\overrightarrow{r_1})\rho(\overrightarrow{r_2})}{|\overrightarrow{r_1}-\overrightarrow{r_2}|}\mathbf{dr_1 dr_2} + \int \varepsilon_{XC}\{\rho(\overrightarrow{r})\}\rho(\overrightarrow{r})\mathbf{dr} \\
&+E_{eI}([\psi_i(\overrightarrow{r})],\{\overrightarrow{R_I}\}) + U_I^O(\{\overrightarrow{R_I}\}) \qquad (1.12)
\end{aligned}
$$

where, on the right hand side, the first term is the electronic kinetic energy, second term represents electron-electron Coulomb energy, electron exchange correlation energy is represented by the third term, the fourth term is electron-ion interaction energy and the last term represents ion-ion interaction. Ionic potential energy for the electrons in ground state can be obtained by minimizing E_{KS} with respect to single particle wave function ψ_i. In Born-Oppenheimer molecular dynamics (BOMD) method, E_{KS} is minimized at each molecular dynamics step which can be time consuming.

On the other hand, Car-Parrinello technique provides a parametric evolution of the

electronic and ionic degrees of freedom through classical equations of motion with different time scales for electrons and ions. The CP Lagrangian (L_{CP}) can be written as,

$$\begin{aligned} L_{CP} &= \mu \sum_i \int |\dot{\psi}_i(\overrightarrow{r})|^2 \mathbf{dr} + \frac{1}{2} \sum_I M_I \dot{\overrightarrow{R_I}}^2 - E_{ks}[\{\psi_i\}, \overrightarrow{R_I}] \\ &\quad + \sum_{i,j} \Lambda_{ij} \left(\int \psi_i^*(\overrightarrow{r}) \psi_j(\overrightarrow{r}) \mathbf{dr} - \delta_{ij} \right) \end{aligned} \tag{1.13}$$

In the right hand side of the above equation, first and second terms are kinetic energy of electrons, and ions respectively, and the third term is Kohn-Sham energy functional, while the last term ensures orthonormality of the wave functions. The parameter 'μ', also known as 'fictitious' electronic mass, is a mass-like quantity having the units of energy×time^2. The resulting equations of motion for electronic and ionic parts with holonomic constraints are,

$$\frac{d}{dt} \frac{\partial L_{CP}}{\partial \dot{\mathbf{R}}_\mathbf{I}} = \frac{\partial L_{CP}}{\partial \mathbf{R_I}} \tag{1.14}$$

$$\frac{d}{dt} \frac{\delta L_{CP}}{\delta \dot{\psi}^*} = \frac{\delta L_{CP}}{\delta \psi^*} \tag{1.15}$$

Thus, the time evolution of ions and electrons in CP dynamics are found to be of the form,

$$M_I \ddot{\mathbf{R}}_\mathbf{I}(t) = -\frac{\partial}{\partial \mathbf{R_I}} E_{KS} + \frac{\partial}{\partial \mathbf{R_I}} \{constraints\} \tag{1.16}$$

$$\mu_i \ddot{\psi}_i(t) = -\frac{\delta}{\delta \psi_i} E_{KS} + \frac{\delta}{\delta \psi_i} \{constraints\} \tag{1.17}$$

Solving these equations, the unknown variables such as ψ_i(r,t), R_I(t), and λ_{ij}(t) can be estimated from the initial conditions on $R_I(0)$, $\dot{R}_I(0)$, $\psi_i(0)$, $\dot{\psi}_i(0)$, and $\lambda_{ij}(0)$.

Let us now compare the dynamics generated from CP equations of motion with that of from BOMD. In BOMD, the Kohn-Sham energy functional is minimized at each molecular dynamics time step in order to get the ground state wavefunction of the electrons with

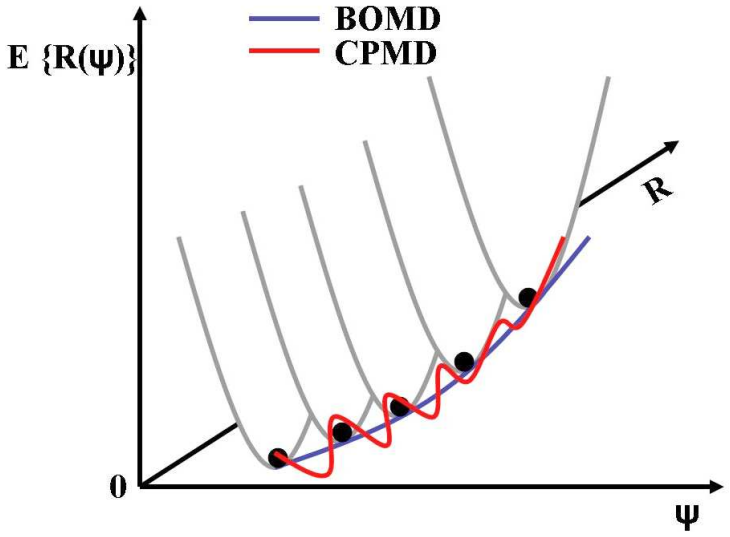

Figure 1.16: **Schematic representation of the BO and CP molecular dynamics trajectories. For simplicity, the Kohn-Sham energy functionals are displayed as harmonic oscillator potential energy surfaces where black circles imply to the ground state wave functions for electronic orbital at a particular set of ionic coordinates. The red-line shows the small oscillation in the CP dynamics around the true BO trajectory. (adapted from Prof. S. Scandolo's lecture)**

respect to the instantaneous ionic positions. Thus the force exerted on ionic and as well as on electronic degrees of freedom keeps the system to be adiabatic. On the other hand, in case of CPMD the optimization of electronic wave function is performed only at the beginning of MD simulation which implies the ionic force calculated in the CP method is different from the BO force. This discrepancy gives rise to different dynamical trajectories. Only when the deviation of the CP trajectory is negligibly small from that of BO trajectory, one can get the true ionic time evolution. In Figure 1.16, the time evolution of BO and CP dynamics has been shown schematically.

1.7.3 Constants of motion

The study of constants of motion along a CP trajectory provides the information on the accuracy of the calculations. For a time independent Lagrangian, the apparent constant of motion is,

$$E_{cons} = \sum_i \frac{1}{2}\mu_i \langle \dot{\psi}_i | \dot{\psi}_i \rangle + \sum_I \frac{1}{2} M_I \dot{\mathbf{R}}_\mathbf{I}^2 + \langle \psi_0 | H_{KS} | \psi_0 \rangle \tag{1.18}$$

Here, the first term represents the fictitious kinetic energy (T_e) of electrons. The physical energy (E_{phys}) of the system is thus the sum of ionic kinetic and the total potential (E_{KS}) energies.

$$T_e = \sum_i \frac{1}{2}\mu_i \langle \dot{\psi}_i | \dot{\psi}_i \rangle \tag{1.19}$$

$$E_{KS} = \langle \psi_0 | H_{KS} | \psi_0 \rangle \tag{1.20}$$

$$E_{phys} = \sum_I \frac{1}{2} M_I \dot{\mathbf{R}}_\mathbf{I}^{\,2} + \langle \psi_0 | H_{KS} | \psi_0 \rangle = E_{cons} - T_e \tag{1.21}$$

In Figure 1.17 these energy parameters are shown for a model system (a periodic diamond lattice of eight silicon atoms with local density approximation to density functional theory, norm conserving pseudopotential for core electrons, 6 Ry plane wave cut off, fictitious electronic mass, μ = 300 a.u. with 0.3 fs time step and 6.3 ps molecular dynamics trajectory [105]) as a function of time. The total energy, E_{cons} is a conserved quantity

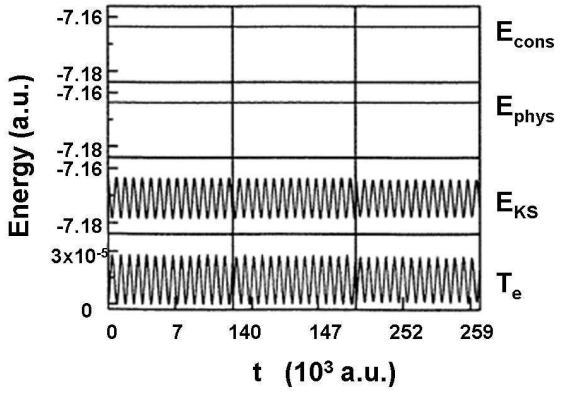

Figure 1.17: **Different energy parameters from Eqn. 1.21 obtained for a model system. Adapted from Ref [105]**

with 10^{-6} standard deviation from the mean value of energy. Oscillatory behaviour in the fictitious electronic energy ensures that there is no energy transfer from the 'hot' nuclei to the 'cold' electrons. As mentioned earlier, T_e is the extra term introduced in the CP Hamiltonian from that of exact BO calculations. Thus, this term reproduces the deviation of the CP dynamics from the true BO energy surface. A closer inspection of the forces

calculated from CP and BO methods are shown in the Figure 1.18, and Figure 1.19

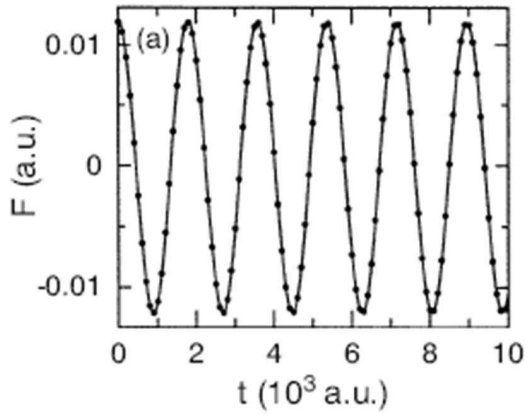

Figure 1.18: **. X-components of the force on an atom obtained from Car-Parrinello ($\mathbf{F}_{CP}$, solid line) and well-converged Born-Oppenheimer ($\mathbf{F}_{BO}$, dots) simulations in a model system. Adapted from Ref [105]**

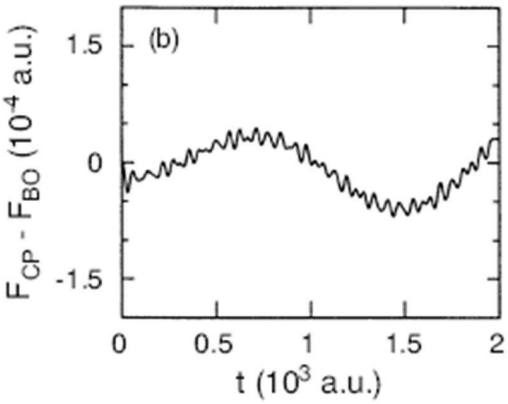

Figure 1.19: **Deviation of $\mathbf{F}_{CP}$ from $\mathbf{F}_{BO}$. Adapted from Ref [105]**

One can notice two different time scales of oscillations in Figure 1.19. The high frequency part is due to the intrinsic fast electronic motion and the low frequency part arises from a weak coupling between electronic and ionic modes. Indeed, the instantaneous CP force is different from the exact BO force but in average this deviation is negligible which is of the order of one part in 10^4.

Another important aspect of the CP method is the choice of the value for fictitious electron mass, μ. In the limit of infinitesimally small value of μ, the first term in the

right hand side of Eqn. 1.18 reduces to 0 which leads to the exact Born-Oppenheimer molecular dynamics trajectory. In order to achieve adiabaticity, the separation between minimum electronic frequency (ω_e^{min}) and the maximum phonon frequency (ω_n^{max}) should be large [104, 105, 117]. The analytical expression for ω_e^{min} is given by,

$$\begin{aligned} \omega_e^{min} &\propto \left(\frac{E_{HOMO-LUMO}}{\mu}\right)^{1/2} \\ &\propto \left(\frac{E_{gap}}{\mu}\right)^{1/2} \end{aligned} \tag{1.22}$$

The crucial point is, however, the adiabaticity of the system depends on occupied and unoccupied band gap as well as on the value of μ. Decreasing μ value kicks up the electronic minimum frequency resulting in the decrease in simulation time step. That is, lower μ value reproduces more accurate result. As CPMD simulations are computationally time consuming, there has to be the balance between accuracy and speed of the calculations. It has been proved by Schutte et. al [148] that if the energy gap is greater than zero, the difference between the trajectories generated from CP ($\mathbf{R}_I^{CP}$) and BO ($\mathbf{R}_I^{BO}$) methods is,

$$|\mathbf{R_I^{BO}}(\mathbf{t}) - \mathbf{R_I^{CP}}(\mathbf{t})| < C\sqrt{\mu} \tag{1.23}$$

where, C is some constant. On the other hand, for $E_{gap} = 0$, i.e. for metallic system, the electronic energy increases unresistingly. In those cases, electronic thermostats [149–152] can be used to keep the electrons in BO energy surface.

1.7.4 Hellmann-Feynman Force

The important aspect of any dynamical system is the calculation of forces on the ions. In the Hellmann-Feynman scheme [153–159], the force on a particular configuration of nuclear positions can be derived by taking the derivatives of the total energy of the system with respect to parameters dependent on nuclear position. The force on a nucleus is thus the electrostatic forces by other nuclei and the charge distribution in the system. Let

the nuclear position be dependent on a variable λ which could be internuclear distance, a semi-empirical parameter in an approximate theory, a nuclear coordinate, and so on. Thus the force, F_λ, which is the negative slope of the potential energy surface can be defined as,

$$F_\lambda = -\frac{\partial}{\partial\lambda}\langle\psi|H_{KS}|\psi\rangle \tag{1.24}$$

Now, the expansion of the above equation gives,

$$\frac{\partial}{\partial\lambda}\langle\psi|H_{KS}|\psi\rangle = \langle\psi|\frac{\partial H_{KS}}{\partial\lambda}|\psi\rangle + \langle\frac{\partial\psi}{\partial\lambda}|H_{KS}|\psi\rangle + \langle\psi|H_{KS}|\frac{\partial\psi}{\partial\lambda}\rangle \tag{1.25}$$

If ψ is an exact solution of H_{KS}, $H_{KS}|\psi\rangle = E_{KS}|\psi\rangle$. Thus we can write,

$$\frac{\partial}{\partial\lambda}\langle\psi|H_{KS}|\psi\rangle = \langle\psi|\frac{\partial H_{KS}}{\partial\lambda}|\psi\rangle \tag{1.26}$$

When the wavefunction is exact and expressed by complete basis sets, the force calculated from Hellmann-Feynman theorem (HFT) can be written as,

$$F_\lambda^{HFT} = -\langle\psi|\frac{\partial H_{KS}}{\partial\lambda}|\psi\rangle \tag{1.27}$$

As discussed earlier, the one particle wave function ψ_i is expressed by a sum of plane wave basis functions multiplied by some coefficient.

$$\psi_i = \sum_k C_k^i f_k(\mathbf{r};\{\mathbf{R_I}\}) \tag{1.28}$$

Differentiation of the above equation with respect to λ gives,

$$\frac{\partial\psi}{\partial\lambda} = \sum_k \frac{\partial C_k^i}{\partial\lambda} f_k + \sum_k C_k^i \frac{\partial f_k}{\partial\lambda} \tag{1.29}$$

By substituting Eqn. 1.29 in Eqn. 1.24,

$$\begin{aligned} F_\lambda &= F_\lambda^{HFT} - \sum_{i,\nu,\mu}(\langle\frac{\partial C_\nu^i}{\partial\lambda}f_\nu|H_e|C_\mu^i f_\mu\rangle + \langle C_\nu^i\frac{\partial f_\nu}{\partial\lambda}|H_e|C_\mu^i f_\mu\rangle \\ &\quad +\langle C_\nu^i f_\nu|H_e|\frac{\partial C_\mu^i}{\partial\lambda}f_\mu\rangle + \langle C_\nu^i f_\nu|H_e|C_\mu^i\frac{\partial f_\mu}{\partial\lambda}\rangle) \\ &= F_\lambda^{HFT} - \sum_{i\nu\mu}(\langle\frac{\partial f_\nu}{\partial\lambda}|H_e^{NSC}-\epsilon_i|f_\mu\rangle + \langle f_\nu|H_e^{NSC}-\epsilon_i|\frac{\partial f_\mu}{\partial\lambda}) \\ &\quad -\int d\mathbf{r}\frac{\partial\rho}{\partial\lambda}(U^{SCF}-U^{NSC}) \end{aligned} \tag{1.30}$$

where, ρ is charge density, $\rho(\mathbf{r}) = \sum_i \psi_i^*(\mathrm{r})\ \psi_i(\mathrm{r})$. The second term in the right hand side of the above equation is called as 'incomplete-basis-set-correction' (IBS) [160, 161] and ϵ_i is the single particle eigen value from the Hartree equation.

$$F_\lambda^{IBC} = -\sum_{i\nu\mu}(\langle\frac{\partial f_\nu}{\partial\lambda}|H_e^{NSC}-\epsilon_i|f_\mu\rangle + \langle f_\nu|H_e^{NSC}-\epsilon_i|\frac{\partial f_\mu}{\partial\lambda}) \tag{1.31}$$

U^{SCF} is the 'self-consistent' (SCF) potential whereas U^{NSC} is the complement of it that is 'non-self-consistent' (NSC) corresponding to H_e^{NSC}. Total force acting on a nucleus due to λ parameter is,

$$F_\lambda = F_\lambda^{HFT} + F_\lambda^{IBC} + F_\lambda^{NSC} \tag{1.32}$$

Finally, F_λ turns out to be equal to F_λ^{HFT} only when ψ is the exact solution of H_{KS} and also is expanded in a complete plane wave basis set. Note that, there is an extra term in the total force which arises due to incompleteness of the basis set. Thus at each time step, $\langle\psi|H_{KS}|\psi\rangle$ has to be minimized up to a certain tolerance. Car-Parrinello molecular dynamics method does not really depend on the exact minimization of $\{\langle\psi|H_{KS}|\psi\rangle\}$, which in turn implies that non-consistency correction to the force, F^{NSC}, is irrelevant in CPMD. Whereas, NSC correction is mandatory in BOMD due to its method of operation.

The more extended and generalized [162–165] version of Hellmann-Feynman theorem assumes the classical movement of nuclei while the electrons move quantum mechanically.

This method is also known as 'dynamical Feynman theorem' which has not been discussed here.

1.8 Codes developed and Used

All the results reported in this thesis have been obtained from computer simulation techniques. Bulk systems were simulated in two steps. Initially, the system under consideration was generated with random positions of the molecules at the appropriate density with meaningful intermolecular minimum separations. Such a system was equilibrated employing classical interaction potentials. The PINY-MD [166] package was used for this purpose. The final configuration is used as the starting configuration for first principle MD simulations. Bulk *ab inito* studies were performed using the CPMD [167] code. In some situations, the geometry optimization of small molecular clusters were carried out using Gaussian 98 [168] code. For the calculation of molecular multipole moments from electronic charge density, a code was developed to obtain the appropriate electrostatic integrals. For the calculation of time correlation functions of the bulk system over a very large number of time steps, we have developed MPI based codes. Other codes to study the structure, dynamics, and electronic properties were developed during the course of this research work. The CPMD simulations were performed on Beowulf clusters in our group, on the Centre for Development of Advanced Computing's IBM-SP based cluster, and in the Centre for Modeling and Simulation, University of Hyderabad's IBM SMP machines.

Bibliography

[1] R. S. Berry, S. A. Rice, J. Ross, *Physical Chemistry*, Oxford University Press (2000).

[2] D. Chandler, K. S. Schweizer, P. G. Wolynes, *Phys. Rev. Lett.* **49**, 1100 (1982).

[3] J. S. Hoye, K. Olaussen, *J. Chem. Phys.* **77**, 2583 (1982).

[4] P. G. Wolynes, *J. Chem. Phys.* **86**, 5133 (1987).

[5] I. Rips, J. Klafter, J. Jortner, *J. Chem. Phys.* **89**, 4288 (1988).

[6] A. L. Nichols, D. F. Calef, *J. Chem. Phys.* **89**, 3783 (1988).

[7] Y. C. Chen, J. L. Lebowitz, P. Nielaba, *J. Chem. Phys.* **91**, 340 (1989).

[8] D. Chandler, *Phys. Rev. E* **48**, 2898 (1993).

[9] X. Song, D. Chandler, R. A. Marcus, *J. Phys. Chem.* **100**, 11954 (1996).

[10] E. Bauer, M. Magat, *J. Phys. Radium* **9**, 319 (1938).

[11] A. Schallamach, *Trans. Faraday Soc.* **42A**, 180 (1946).

[12] M. D. Magee, *J. Chem. Soc. Faraday Trans.* **70**, 929 (1974).

[13] B. Bagchi, *Annu. Rev. Phys. Chem.* **40**, 115 (1989).

[14] P. F. Barbara, W. Jarzeba, *Adv. Photochem.* **15**, 1 (1990).

[15] M. Maroncelli, *J. Mol. Liq.* **57**, 1 (1993).

[16] M. G. Viloca, K. Nam, C. Alhambra, J. Gao, *J. Phys. Chem. B* **108**, 13501 (2004).

[17] S. S. Xantheas, T. H. Dunning, *J. Chem. Phys.* **99**, 8774-8792 (1993).

[18] M. Lim, P. Hamm, R. M. Hochstrasser, *Proc. Natl. Acad. Sci. USA* **95**, 15315 (1998).

[19] N. K. Petrov, A. Wiessner, H. Staerk, *Chem. Phys. Lett.* **241**, 127 (1995).

[20] N. K. Petrov, A. Wiessner, H. Staerk, *J. Chem. Phys.* **108**, 2326 (1998).

[21] E. Browning, *Toxicity of Industrial Organic Solvents* Rev. ed., London : H. M. Stationary Office, 411 (1953).

[22] K. Vaajasaari, M. Kulovaara, A. Joutti, E. Schultz, K. Soljamo, *J. Hazardous Materials* **106**, 71 (2004).

[23] R. Yang, W. Xie, *Forensic Science International* **139**, 177 (2004).

[24] A. Salvador, A. Chisvert, *Analytica Chimica Acta* **537**, 15 (2005).

[25] P. Mazzafera, A. Carvalho, *Documentos IAC* **25**, 1 (1991).

[26] G. Bruner, *Ber. Bunsen-Ges. Phys. Chem.* **88**, 887 (1984).

[27] M. A. McHugh, V. Krukonis, *J. Supercritical Fluid Extraction : Principles and Practice*; Butterworth Publishers: Boston, MA, (1994).

[28] H. Peker, M. P. Srinivasan, J. M. Smith, B. J. McCoy, *AlChE J.* **38**, 761 (1992).

[29] M. D. A. Saldaña, R. S. Mohamed, M. G. Baer, P. Mazzafera, *J. Agric. Food. Chem.* **47**, 3804 (1999).

[30] P. J. Fraser, M. J. Prather, *Nature* **398**, 663-664 (1999).

[31] J. Sherman, B. Chin, P. D. T. Huibers, R. Garcia-Valls, T. A. Hatton, *Environmental Health Perspectives Supplements* **106**, 253 (1998).

[32] R. T. Baker, W. Tumas, *Science* **284**, 1477-1479 (1999).

[33] B. Horton, *Nature* **400**, 797-799 (1999).

[34] M. Poliakoff, *Science* **297**, 807-810 (2002).

[35] R. A. Sheldon, *Green Chem.* **7**, 267 (2005).

[36] *Chemical Synthesis Using Supercritical Fluids,* (Eds.: P.G. Jessop and W. Leitner), Wiley-VCH, Weinheim, 1999.

[37] W. Leitner *Nature* **405**, 129 (2000).

[38] J. M. DeSimone *Science* **297**, 799 (2002).

[39] A. J. Carmichael, M. J. Earle, J. D. Holbrey, P. B. McCormac, K. R. Seddon, *Org. Lett.* **1**, 997 (1999).

[40] R. Sheldon, *ChemComm* **23**, 2399 (2001).

[41] J. G. Huddleston, H. D. Willauer, R. P. Swatloski, A. E. Visser, R. D. Rogers, *ChemComm* **16**, 1765 (1998).

[42] K. R. Seddon, *J. Chem. Technol. Biotech.* **68**, 351 (1997).

[43] P. Bonhote, A. Dias, N. Papageorgiou, K. Kalyanasundaram, M. Gratzel, *Inorg. Chem.* **35**, 1168 (1996).

[44] J. Fuller, A. C. Breda, R. T. Carlin, *J. Electroanal. Chem.* **459**, 29 (1998).

[45] B. M. Quinn, Z. Ding, R. Moulton, A. J. Bard, *Langmuir* **18**, 1734 (2002).

[46] M. Poliakoff, P. King, *Nature* **412**, 125 (2001).

[47] S. L. Wells, J. DeSimone, *Angew. Chem. Int. Ed.* **40**, 518 (2001).

[48] A. I. Cooper, J. D. Londono, G. Wignall, J. B. McClain, E. T. Samulski, J. S. Lin, A. Dobrynin, M. Rubinstein, A. L. C. Burke, J. M. J. Frechet, J. M. DeSimone, *Nature* **389**, 368-371 (1997).

[49] G. Brumfiel, *Nature* **431**, 622-623 (2004).

[50] C. A. Eckert, B. L. Knutson, P. G. Debenedetti, *Nature* **383**, 313 (1996).

[51] P. G. Jessop, T. Ikariya, R. Noyorl, *Nature* **368**, 231 (1994).

[52] M. Poliakoff, S. M. Howdle, S. G. Kazarian, *Angew. Chem. Int. Ed. Engl.* **34**, 1275 (1995).

[53] P. S. Shah, T. Hanrath, K. P. Johnston, B. A. Korgel, *J. Phys. Chem. B* **108**, 9574 (2004).

[54] T. Clifford, *Fundamentals of Supercritical Fluids*, Oxford University Press, 1999.

[55] M. Ji, X. Chen, C. M. Wai, J. L. Fulton, *J. Am. Chem. Soc.* **121**, 2631 (1999).

[56] J. D. Holmes, P. A. Bhargava, B. A. Korgel, K. P. Johnston, *Langmuir* **15**, 6613 (1999).

[57] P. S. Shah, J. D. Holmes, R. C. Doty, K. P. Johnston, B. A. Korgel, *J. Am. Chem. Soc.* **122**, 4245 (2000).

[58] P. S. Shah, S. Husain, K. P. Johnston, B. A. Korgel, *J. Phys. Chem. B* **106**, 12178 (2002).

[59] M. J. Burk, S. Feng, M. F. Gross, W. J. Tumas *J. Am. Chem. Soc.* **117**, 8277 (1995).

[60] A. Baiker *Chem. Rev.* **99**, 453 (1999).

[61] P. Licence, J. Ke, M. Sokolova, S. K. Ross, M. Poliakoff, *Green Chem.* **5**, 99 (2003).

[62] T. Morita, K. Nishikawa, M. Takematsu, H. Iida, S. Furutaka, *J. Phys. Chem. B* **101**, 7158 (1997).

[63] P. Freund, S. Bachu, D. Simbeck, K. Thambimuthu, M. Gupta, *IPCC Special Report on Carbon Dioxide Capture and Storage*, AI-1 (2005).

[64] T.W. Randolph, H.W. Blanch, J.M. Prausnitz, C. R.Wilke *Biotechnol. Lett.* **7**, 325 (1985).

[65] D. A. Hammond, M. Karel, A. M. Klibanov, V. J. Krukonis *Appl. Biochem. Biotechnol.* **11**, 393 (1985).

[66] K. Nakamura, Y. M. Chi, Y. Yamada, T. Yano *Chem. Eng. Commun.* **45**, 207 (1986).

[67] T. W. Randolph, D. S. Clark, H. W. Blanch, J. M. Prausnitz, *Science* **239**, 387-390 (1988).

[68] T. Matsuda, T. Harada, K. Nakamura *Green Chem.* **6**, 440 (2004).

[69] T. Matsuda, R. Kanamaru, K. Watanabe, T. Harada, K. Nakamura *Tetrahedron Lett.* **42**, 8319 (2001).

[70] K. P. Johnston, D. G. Peck, S. Kim *Ind. Eng. Chem. Res.* **28**, 1115 (1989).

[71] S. Ganapathy, C. Carlier, T. W. Randolph, J. A. O'Brien *Ind. Eng. Chem. Res.* **35**, 19 (1996).

[72] L. Reynolds, J. A. Gardecki, S. J. V. Frankland, M. L. Horng, M. Morencelli, *J. Phys. Chem.* **100**, 10337 (1996).

[73] J. F. Kauffman, *J. Phys. Chem. A* **105**, 3433 (2001).

[74] P. Raveendran, S. L. Wallen, *J. Phys. Chem. B* **107**, 1473 (2003).

[75] P. Raveendran, Y. Ikushima, S. L. Wallen, *Acc. Chem. Res.* **38**, 478 (2005).

[76] N. J. Bridge, A. D. Buckingham, *Proc. Roy. Soc.* (London) **A295**, 334 (1966).

[77] H. A. Gebbie, N. W. B. Stone, *Proc. Phys. Soc.* **82**, 543 (1963).

[78] Y. L. Baranov, A. A. Vigasin, *J. Mol. Spec.* **193**, 319 (1999).

[79] A. A. Vigasin, *J. Mol. Spec.* **200**, 89 (2000).

[80] A. A. Vigasin, F. Huisken, A. I. Pavlyuchko, L. Ramonat, E. G. Tarakanova, *J. Mol. Spec.* **209**, 81 (2001).

[81] J. Kestin, J. H. Whitelaw, T. F. Zien, *Physica* **30**, 161 (1964).

[82] L. Bruschi, M. Santini, *Phys. Lett. A* **73**, 395 (1979).

[83] H. Iwasaki, M. Takahashi, *J. Chem. Phys.* **74**, 1930 (1981).

[84] J. B. Hannay, J. Hogart, *Proc. R. Soc. London* **29**, 324 (1879).

[85] K. D. Bartles, A. A. Clifford, S. A. Jaffar, G. F. Shilstone, *J. PhysChem. Ref. Data* **20**, 713 (1991).

[86] A. Hourri, J. M. St-Arnaud, T. K. Bose, *Rev. Sci. Instrum.* **69**, 2732 (1998).

[87] K. A. Consani, R. D. Smith, *J. Supercrit. Fluids* **3**, 51 (1990).

[88] J. Jin, Z. Zhang, Q. Li, Y. Li, and E. Yu, *J. Chem. Eng. Data* **50**, 801 (2005).

[89] H. P. Li, H. F. Zhang, J. Liu, and B. X. Han, *Chinese Chemical Letters* **12**, 351 (2001).

[90] D. Pyo, K. Park, H. Shin, and M. Moon, *Chromatographia* **49**, 539 (1999).

[91] R.C. Reid, J.M. Prausnitz, and B.E. Poling, *The properties of gases and liquids.* McGraw Hill, New York.

[92] H. M. J. Levelt Sengers, in *Supercritical Fluids, Fundamentals for Application* (eds. E. Kiran, and H. M. J. Levelt Sengers) 3-38 (NATO ASI Ser. E, 273, Kluwer, Dordrecht, 1994).

[93] J. S. Keiper, R. Simhan, J. M. DeSimone, G. D. Wingnall, Y. B. Melnichenko, H. Frielinghaus, *J. Am. Chem. Soc.* **124**, 1834 (2002).

[94] M. J. Clarke, K. L. Harrison, K. P. Johnston, S. M. Howdle, *J. Am. Chem. Soc.* **119**, 6399 (1997).

[95] S. R. P. Rocha, K. P. Johnston, R. E. Westacott, P. J. Rossky, *J. Phys. Chem. B* **105**, 12092 (2001).

[96] A. V. Yazdi, E. Beckman, *Ind. Eng. Chem. Res.* **35**, 3644-3652 (1996).

[97] J. R. Brennecke, *Nature* **389**, 333-334 (1997).

[98] X. Zhang, B. Han, Z. Hou, J. Zhang, Z. Liu, T. Jiang, J. He, H. Li, *Chem. Eur. J.* **8**, 5107 (2002).

[99] D. L. Tomasko, B. L. Knutson, F. Pouillot, C. L. Liotta, C. A. Eckert, *J. Phys. Chem.* **97**, 11823 (1993).

[100] S. S. T. Ting, S. J. Macnaughton, D. L. Tomasko, N. R. Foster, *Ind. Eng. Chem. Res.* **32**, 1471 (1993).

[101] S. Kim, K. P. Johnston, *Am. Inst. Chem. Eng. J.* **33**, 1603 (1987).

[102] R. Car, M. Parrinello, *Phys. Rev. Lett.* **55**, 2471 (1985).

[103] G. Galli, M. Parrinello, *Science* **250**, 1547 (1990).

[104] D. K. Remler, P. A. Madden, *Molec. Phys.* **70**, 912 (1990).

[105] G. Pastore, E. Smargiassi, F. Buda, *Phys. Rev. A* **44**, 6334 (1991).

[106] M. C. Payne, M. P. Teter, D. C. Allan, T. A. Aris, J. D. Joannopoulos, *Rev. Mod. Phys.* **64**, 1045 (1992).

[107] M. Palummo, L. Reining, P. Ballone, *J. Phys. IV (Paris)* **3:(C7)**, 1955 (1993).

[108] E. Deumens, A. Diz, R. Longo, Y. Ohrn, *Rev. Mod. Phys.* **66**, 917 (1994).

[109] M. E. Tuckerman, M. Parrinello, *J. Chem. Phys.* **101**, 1302, 1316 (1994).

[110] J. Hutter, M. Tuckerman, M. Parrinello, *J. Chem. Phys.* **102**, 859 (1995).

[111] M. E. Tuckerman, P. J. Ungar, T. von Rosenvinge, M. L. Klein, *J. Phys. Chem.* **100**, 12878 (1996).

[112] M. J. Gillan, *Contemp. Phys.* **38**, 115 (1997).

[113] M. Parrinello, *Solid State Commun.* **102**, 107 (1997).

[114] E. Sandre, and A. Pasturel, *Mol. Simul.* **20**, 63 (1997).

[115] D. Marx, *Nachr. Chem. Tech. Lab.* **47**, 186 (1999).

[116] D. Marx, J. Hutter, '*Ab initio* Molecular Dynamics : Theory and Implementation', in http://www.fz-juelich.de/nic-series/ (2000).

[117] M. Parrinello, *Comput. Sci. Engg.* **2**, 22 (2000).

[118] D. Frenkel, and B. Smit, *Understanding Molecular Simulation* (Academic Press, San Diego, 1996).

[119] M. P. Allen, D. J. Tildesley, *Computer Simulation of Liquids* (Oxford, Clarendon, 1987).

[120] G. Ciccotti, D. Frenkel, and I. R. Mc.Donald, *Simulation of Liquids and Solids : Molecular Dynamics and Monte Carlo Methods in Statistical Mechanics* (North Holland, Amsterdam, 1990).

[121] J. P. Hansen, G. Ciccotti, and W. G. Hoover, *Molecular-Dynamics Simulation of Statistical-Mechanical Systems* (North-Holland, Amsterdam, 1986).

[122] A. R. Leach, *Molecular Modelling : Principles and Applications* (Prentice Hall, Harlow, 2001).

[123] A. K. Rappe, and C. J. Casewit, *Molecular Mechanics Across Chemistry* (University Science Books, Sausalito, 1997).

[124] M. J. Field, *A Practical Introduction to Simulation of Molecular Systems* (Cambridge University Press, Cambridge, 1999).

[125] M. Johnson, D. O'Connor, P. Barnes, C. R. A. Catlow, S. L. Owens, G. Sankar, R. Bell, S. J. Teat, R. Stephenson, *J. Phys. Chem. B* **107**, 942 (2003).

[126] A. Mudi, C. Chakravarty, E. Miltotti, *J. Chem. Phys.* **125**, 074508 (2006).

[127] D. Marx, *NIC Series* **31**, ISBN 3-00-017350-1, 195 (2006).

[128] S. Goundla, S. Nielsen, P. B. Moore, M. L. Klein, *J. Am. Chem. Soc.* **128**, 848 (2006).

[129] I-F. Will Kuo, C. J. Mundy, B. L. Eggimann, M. J. McGrath, J. I. Siepmann, B. Chen, J. Vieceli, D. J. Tobias, *J. Phys. Chem. B* **110**, 3738 (2006).

[130] T. Todorova, A. P. Seitsonen, J. Hutter, I-F. W. Kuo, C. J. Mundy, *J. Phys. Chem. B* **110**, 3685 (2006).

[131] R. M. Lynden-Bell, P. G. Debenedetti, *J. Phys. Chem. B* **109**, 6527 (2005).

[132] A. D. MacKerell, D. Bashford, M. Bellott, R. L. Dunbrack, J. D. Evanseck, M. J. Field, S. Fischer, J. Gao, H. Guo, S. Ha, D. Joseph-McCarthy, L. Kuchnir, K. Kuczera, F. T. K. Lau, C. Mattos, S. Michnick, T. Ngo, D. T. Nguyen, B. Prodhom, W. E. Reiher, B. Roux, M. Schlenkrich, J. C. Smith, R. Stote, J. Straub,

M. Watanabe, J. Wiorkiewicz-Kuczera, D. Yin, and M. Karplus, *J. Phys. Chem. B* **102**, 3586 (1998).

[133] P. Hohenberg, W. Kohn, *Phys. Rev.* **136**, B864 (1964).

[134] W. Kohn, L. J. Sham, *Phys. Rev.* **140**, A1133 (1965).

[135] I. R. Stich, R. Car, M. Parrinello, S. Baroni, *Phys. Rev. B* **39**, 4997 (1989).

[136] V. Heine, *Solid. St. Phys.* **24**, 1 (1970).

[137] L. R. Kahn, W. A. Goddard, *J. Chem. Phys.* **56**, 2685 (1972).

[138] G. B. Bachelet, D. R. Hamann, M. Schlüter, *Phys. Rev. B* **26**, 4199 (1982).

[139] L. Kleinman, D. M. Bylander, *Phys. Rev. Lett.* **48**, 1425 (1982).

[140] Y. Bar-Yam, S. T. Pantelides, J. D. Joannopoulos, *Phys. Rev. B* **39**, 3396 (1989).

[141] A. Rappe, K. Rabe, E. Kaxiras, J. D. Joannopoulos, *Phys. Rev. B* **41**, 1227 (1990).

[142] D. Vanderbilt, *Phys. Rev. B* **41**, 7892 (1990).

[143] N. Trouillier, J. L. Martins, *Phys. Rev. B* **43**, 1993 (1991).

[144] N. J. Ramer, A. M. Rappe, *Phys. Rev. B* **59**, 12471 (1998).

[145] N. W. Ashcroft, N. D. Mermin, *Solid State Physics* (Holt Saunders, Philadelphia), p. 113.

[146] M. Arjunwadkar, D. G. Kanhere, *Computer Physics Communications* **62**, 8 (1991).

[147] L. Verlet, *Phys. Rev.* **159**, 98 (1967).

[148] F. A. Boremann, C. Scutte, *Numerische Mathematik*, **78**, 359 (1998).

[149] H.C. Andersen, *J. Chem. Phys.* **72**, 2384 (1980).

[150] S. Nose, *Mol. Phys.* **52**, 255 (1984).

[151] S. Nose, *J. Chem. Phys.* **81**, 511 (1984).

[152] G.J. Martyna, M.L. Klein, and M. Tuckerman, *J. Chem. Phys.* **97**, 2635 (1992).

[153] H. Hellmann, *Z. Phys.* **85**, 180 (1933).

[154] H. Hellmann, *Einführung in die Quantenchemie* , Sec. 1-2 (Franz Deuticke, Liepzig and Vienna) (1937).

[155] R. P. Feynman, *Phys. Rev.* **56**, 340 (1939).

[156] W. H. Flygare, J. M. Pochan, G. I. Kerley, T. Caves, M. Karplus, S. Aung, R. M. Pitzer, S. I. Chan, *J. Chem. Phys.* **45**, 2793 (1966).

[157] B. M. Deb, *Proc. Ind. Nat. Sc. Acad.* **37 A**, 349 (1971).

[158] B. M. Deb, *Rev. Mod. Phys.* **45**, 22 (1973).

[159] F. M. Fernandez, *Chem. Phys. Lett.* **233**, 651 (1995).

[160] P. Bendt, A. Zunger, *Phys. Rev. Lett.* **50**, 1684 (1983).

[161] G. P. Srivastava, D. Weaire, *Adv. Phys.* **36**, 463 (1987).

[162] E. H. Kerner, *Phys. Rev. Lett.* **2**, 152 (1959).

[163] W. L. Clinton, *J. Chem. Phys.* **32**, 626 (1960).

[164] P. O. Löwdin, *J. Mol. Spec.* **3**, 46 (1959).

[165] E. F. Hayes, R. G. Parr, *J. Chem. Phys.* **43**, 1831 (1965).

[166] M. E. Tuckerman, D. A. Yarne, S. O. Samuelson, A. L. Hughes, G. J. Martyna, *Comp. Phys. Comm.* **128**, 333 (2000).

[167] CPMD, Copyright IBM Corp 1990-2001, Copyright MPI fur Festkorperforschung Stuttgart 1997- 2005.

[168] M. J. Frisch, G. W. Trucks, H. B. Schlegel, G. E. Scuseria, M. A. Robb, J. R. Cheeseman, V. G. Zakrzewski, J. A. Montgomery, R. E. Stratmann, J. C. Burant, S. Dapprich, J. M. Millam, A. D. Daniels, K. N. Kudin, M. C. Strain, O. Farkas, J. Tomasi, V. Barone, M. Cossi, R. Cammi, B. Mennucci, C. Pomelli, C. Adamo, S. Clifford, J. Ochterski, G. A. Petersson, P. Y. Ayala, Q. Cui, K. Morokuma, D. K. Malick, A. D. Rabuck, K. Raghavachari, J. B. Foresman, J. Cioslowski, J. V. Ortiz, B. B. Stefanov, G. Liu, A. Liashenko, P. Piskorz, I. Komaromi, R. Gomperts, R. L. Martin, D. J. Fox, T. Keith, M. A. Al-Laham, C. Y. Peng, A. Nanayakkara, C. Gonzalez, M. Challacombe, P. M. W. Gill, B. G. Johnson, W. Chen, M. W. Wong, J. L. Andres, M. Head-Gordon, E. S. Replogle, J. A. Pople, Gaussian 98, revision A.9; Gaussian,Inc.: Pittsburgh, PA, 1998.

Chapter 2

First Principles Studies of Pristine Supercritical Carbon Dioxide at T = 318K and P = 130 atm with local density approximations

2.1 Introduction

The structure and dynamics of $scCO_2$, its interface with water, and ternary microemulsions of $scCO_2$, water and fluorinated surfactants have been studied extensively using experiments [1, 2] and by computer simulation methods [3–5]. These simulations employed an empirical interaction model for the constituent molecules which was based on both quantum chemical calculations as well as on equation of state data. Independent validation of such simulations come from neutron and x-ray diffraction experiments [6–8]. It is crucial that such simulations are also verified by molecular dynamics calculations that do not depend on empirical potentials. We employ the CPMD approach here in order to understand the microscopic structure and dynamics of *neat* $scCO_2$. CPMD calculations

are relatively free of empiricism and can thus validate empirical potential models. However, one pays for the increased fidelity in atomic interactions with a limit in the size of the systems and in the time span that can be studied. Such simulations can also be used to fine tune interaction parameters of empirical potentials [9] which can then be employed to study systems of larger sizes which are more relevant for the supercritical state [10]. More importantly, CPMD simulations can shed light on the molecular structure and solvation dynamics of the solvent and are thus essential in their own right [11]. *This is the primary purpose of our study.*

Carbon dioxide is a textbook example of a linear, symmetric molecule with zero dipole moment in its electronic ground state. The leading non-zero multipole moment is thus the quadrupole that couples with the gradient of the electric field. As a consequence, the interaction strength of CO_2 with solutes is expected to be relatively weaker than for a solvent whose molecules possess a permanent dipole moment. This fact, coupled with the relatively low density in the supercritical state seemingly makes scCO_2 a less attractive choice as a solvent. Neutron [6,8,12] and x-ray [7] diffraction experiments on scCO_2 have shown significant structural correlations in the first coordination shell. These experiments and MD simulations using empirical potentials have shown the presence of T-shaped near-neighbor configurations of CO_2 molecules in the supercritical state, particularly at high densities [12]. This arrangement is believed to arise out of the non-zero quadrupole moment of the CO_2 molecule and is supposed to compete against a relatively less probable, parallel configuration of nearest neighbors. A proper understanding of the local structure and reorientational dynamics of *neat* CO_2 in the supercritical state is thus required in order to understand its ability to solvate a variety of species.

Here, we offer some microscopic reasons for the solvation capacity of scCO_2, and thus its widespread use. (i) A structured first coordination shell that prefers an equatorial configuration, and (ii) a non-zero instantaneous molecular dipole moment and an enhanced quadrupole moment. With this aim, we report results of *ab initio* MD calculations of

$scCO_2$. For comparison, we have also performed MD calculations using an established empirical potential. Our larger aims are to study the solvation of small molecules and chemical reactions in $scCO_2$. As a first inquiry, we are interested in characterizing the pristine solvent.

In the following section, we describe the details of the calculations performed, followed by a presentation of the results. Conclusions drawn from this work are discussed later.

2.2 Simulation Details

The CPMD and the classical MD calculations were performed at a temperature of 318.15K and at a density of 0.703 g/cc (or 9.57 molecules nm^{-3}), one of the state points studied in Ref. [13]. The former were carried out using the CPMD code [14], for a system of 32 CO_2 molecules in a cubic box of edge length 14.956Å in the canonical (NVT) ensemble. Three dimensional periodic boundary conditions were employed to obtain bulk behavior. The initial configuration of the system for the CPMD run was obtained from a well equilibrated run of classical MD using empirical potentials. The CPMD calculations were performed using density functional theory within the local density approximation (LDA) and employed Vanderbilt ultrasoft pseudopotentials [15] for core electrons while valence electrons were considered explicitly. The k=0 point of the Brillouin zone was used in these simulations. A plane wave basis set with an energy cutoff of 25 Ry was found to be sufficient in obtaining converged energies and geometry for a CO_2 monomer, and was thus used for the bulk CPMD calculations as well. Given the rather large system size of 512 valence electrons, and a box edge of around 15Å for the $scCO_2$ system, the choice of the ultrasoft pseudopotential is justified. Similar CPMD calculations have been successful in predicting properties of liquid water, methanol and a host of other molecular liquids [11, 16, 17]. The fictitious electronic mass was chosen to be 400 a.u. Its kinetic energy and that of the ions were controlled using Nosé-Hoover chain thermostats [18]. The equations of motion were integrated with a time step of 5 a.u. (around 0.12 fs) over a

total run length of 12 ps (excluding an initial, equilibration time of 3 ps). The electronic degrees of freedom were quenched to the Born-Oppenheimer surface at the start of the CPMD run. The total energy was monitored during the entire CPMD trajectory, and was found to be conserved to 4 parts in 10^6. Atomic configurations and velocities were stored every time step, which were later used for analyzing the structure and dynamics.

The classical MD simulations were performed using the EPM2 potential, which has been used earlier in simulations of liquid CO_2 [19] as well as in studies of the water-CO_2 interface [20]. Here the C-O bond length was constrained to 1.149Å, and a harmonic bending interaction for the intramolecular O-C-O angle was applied. Other details of the potential were identical to those reported earlier [19]. These classical MD simulations were performed under NVT conditions for a system of 100 molecules in a cubic box with three dimensional periodic boundary conditions. The MD equations of motion were integrated with a time step of 0.5 fs. Long range interactions were treated using the Ewald summation method. A distance cutoff of 10.7Å was employed for truncating the nonbonded interactions.

Intermolecular partial structure factors were calculated using the following relation,

$$S_{\alpha\beta}(k) = \delta_{\alpha\beta} + 4\pi(\rho_\alpha\rho_\beta)^{\frac{1}{2}} \int_0^\infty [g_{\alpha\beta} - 1]\frac{sin\ kr}{kr} r^2 dr. \tag{2.1}$$

The total neutron weighted structure factor was obtained as [21],

$$S(k) = b_\alpha^2 S_{\alpha\alpha} + b_\beta^2 S_{\beta\beta} + 2b_\alpha b_\beta S_{\alpha\beta}. \tag{2.2}$$

where $\rho_\alpha = N_\alpha/V$ is the number of atoms of the αth component per unit volume and the neutron scattering lengths (b_α) for carbon and oxygen atoms are 6.646 fm and 5.805 fm respectively.

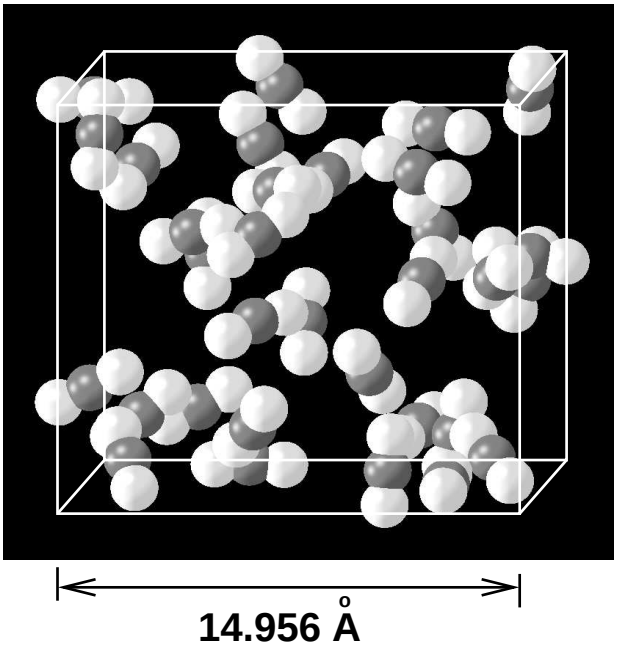

Figure 2.1: **Snapshot of a configuration of 32 molecules of CO_2 in the supercritical state obtained from the CPMD simulations. Oxygen atoms are shown in white, and carbon atoms are in black.**

2.3 Results and Discussion

2.3.1 Molecular Structure

In order to gain confidence in the use of this method with these approximations, we performed a calculation for optimization of the geometry of an isolated CO_2 molecule. Excellent agreement with the structure and vibrational spectrum reported experimentally was obtained. Specifically we obtained the C-O bond length to be 1.167Å, and the O-C-O bond angle to be 180^o, compared to the experimental value for the bond length of 1.162Å [22]. CPMD calculations of the system containing 32 molecules in the supercritical state yielded an average C-O bond length of 1.169Å. A snapshot of the configuration of 32 molecules studied using CPMD is shown in Figure 2.1. An observation of the total

energy of the system during the course of the CPMD run did not indicate the disruption of any intramolecular C-O bond as expected at these state conditions. This is also borne out by the visualization presented in Figure 2.1

2.3.2 Pair Correlation Functions

We have studied the pair correlation function between the sites of different CO_2 molecules in order to understand the structural features of this system. These are shown in Figures 2.2 where a comparison is made between the results obtained from CPMD and from classical MD. The essential features of the pair correlation functions such as the position of the first peak, its minimum, the number of near neighbors, are summarized in Table 2.1.

Figure 2.2a displays $g_{CC}(r)$. The first neighbor C-C distance in the CPMD calculation is around 3.9Å, as compared to a value of 4.3Å from the MD calculation. The first peak in $g_{CC}(r)$ of MD is shifted overall relative to the CPMD result. In addition, the first peak in this function for CPMD is marginally narrower than the corresponding MD result. Thus, the MD calculation overestimates to some extent the thickness of the first coordination shell. At the respective minima of the first peaks the coordination numbers are around 6.3 for the CPMD calculation, as compared to a value of around 9.5 for the MD run.

Quantity	g_{CC}		g_{CO}		g_{OO}	
	CPMD	MD	CPMD	MD	CPMD	MD
First peak (Å)	3.9	4.3	3.1,4.1	4.3	3.1	3.5
First min (Å)	5.5	6.3	5.7	6.1	4.3	4.5
Coordination number	6.3	9.5	13.8	17.3	5.2	5.9

Table 2.1: Summary of structural features.

The intermolecular C-O pair correlation functions obtained from CPMD and MD are shown in Figure 2.2b. The CPMD distribution exhibits two well defined peaks one at 3.1Å and the other at 4.1Å. Although it is likely that these two peaks arise from the two oxygens of the same CO_2 neighbor, a part of the contribution particularly to the second

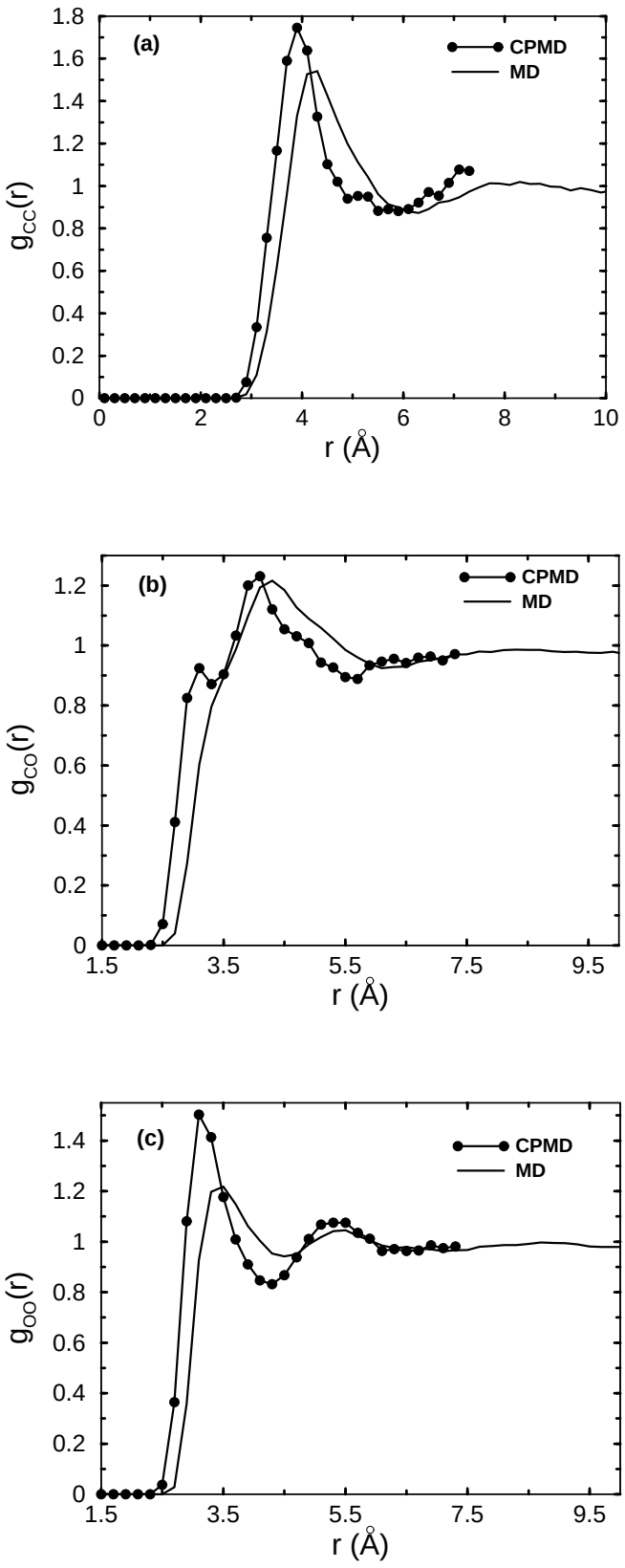

Figure 2.2: **Intermolecular radial distribution functions in supercritical carbon dioxide. (a) $g_{CC}(r)$, (b) $g_{CO}(r)$, (c) $g_{OO}(r)$.**

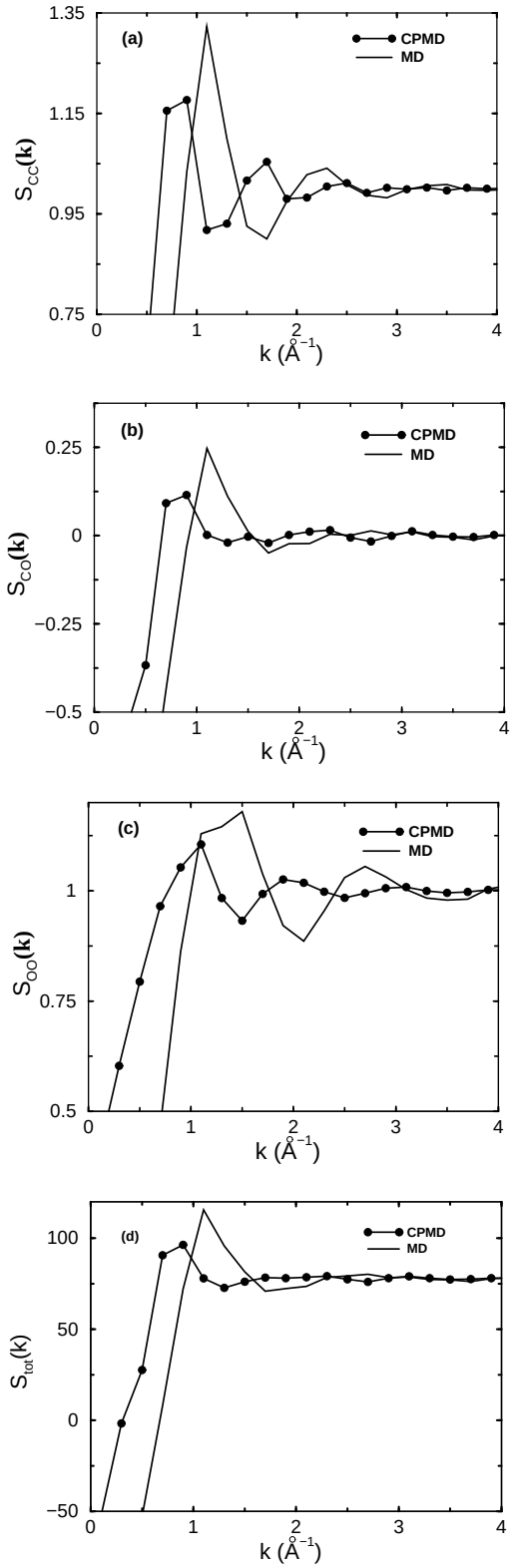

Figure 2.3: **Partial structure factors and neutron weighted total structure factor of scCO$_2$. (a) S$_{CC}$(k), (b) S$_{CO}$(k), (c) S$_{OO}$(k), and (d) S$_{tot}$(k).**

peak could come from CO_2 neighbors who share only one oxygen atom within a distance of 5.7Å (the first peak minimum in $g_{CO}(r)$ from the carbon atom of the central molecule. In the following discussion, we denote the oxygen atom that falls within the first hump of $g_{CO}(r)$ as O_a, and the one falling under the second hump as O_b. The number of oxygen neighbors at the first peak minimum of 3.3Å is around 1.4. The nominal number of oxygen atoms at the minimum of the second hump (at 5.7Å) is 13.8. Since the number of carbon neighbors (from $g_{CC}(r)$) is 6.3, we can expect that twice the number of oxygens in the first coordination shell. The value of 13.8 obtained from $g_{CO}(r)$ is reasonably close to this expectation, suggesting that the two humps in $g_{CO}(r)$ probably arise from the same CO_2 neighbor. The difference is likely to come from those neighbor molecules that do not have both their oxygen atoms within a distance of 6Å of the carbon atom of the central CO_2 molecule. The pair correlation function obtained from MD is shifted to larger distances by about 0.2Å relative to that from CPMD, quite similar to the observations in $g_{CC}(r)$. Also note that the prominent first hump (denoted as O_a above) present in the CPMD data of $g_{CO}(r)$, is absent in the classical MD result. In the absence of a clear hump in $g_{CO}(r)$ obtained from the classical MD run, O_a for the MD results was defined through the change in slope of the pair correlation function that occurred at 3.2Å. Although a hump or a peak is not clearly visible at this distance, an underlying feature at 3.2Å is likely to be the cause for the change in slope. Hence one can suppose that the MD data agrees qualitatively with the CPMD result on the existence of a shorter near neighbor oxygen around a central carbon atom. The intermolecular $g_{OO}(r)$ (Figure 2.2c) obtained from CPMD exhibits a first peak at 3.1Å, with a minimum at 4.3Å. The coordination number at the minimum is around 5.2, in good agreement with the value expected from the preceding discussion on $g_{CO}(r)$. Again, we observe a marginal shift of about 0.4Å in the function obtained from MD, relative to the result of CPMD. The structure factors obtained from these pair correlation functions are shown in Figure 2.3.

2.3.3 Intermolecular Angle Distributions

As discussed in the Introduction, at higher densities of $scCO_2$, near neighbor CO_2 molecules are possibly oriented in a distorted T-shaped geometry. Recently, Cipriani *et al* [12] have predicted an arrangement in which the molecule in the first neighboring shell lies in the equatorial plane of the central molecule. We have examined this aspect by studying the distribution of the angle between molecular backbones of neighbors. We proceed by displaying a schematic of the near neighbor configuration in Figure 2.4.

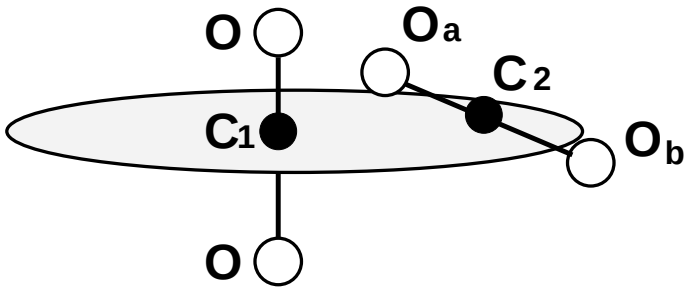

Figure 2.4: **Schematic of the arrangement of near neighbor molecules in $scCO_2$. O_a is the oxygen atom of the neighboring molecule that is closest to the carbon atom (C_1) of the central molecule.**

Here, O_a is an oxygen atom that is within a distance of 3.1Å from the carbon atom of the central CO_2 molecule. C_2 is the carbon atom that is bonded to O_a and O_b is the second oxygen atom in this neighbor molecule. We show in Figure 2.5, the distribution of angles made by the backbone vector (the OC_1 vector) of the central molecule with the vectors, C_1O_a, C_1C_2, and C_1O_b. In all the three cases, a preference for perpendicular orientation is observed. However, the OC_1C_2 and the OC_1O_b distributions are relatively flatter as compared to the distribution of OC_1O_a angles. Thus, our data indicates that although a T-shaped near neighbor configuration is preferred, a significant fraction of neighbors could be oriented such that the O_a atom of the neighbor and its carbon (C_2) are in the equatorial plane of the central CO_2 molecule, while the O_b atom exhibits a tendency to be out of this plane.

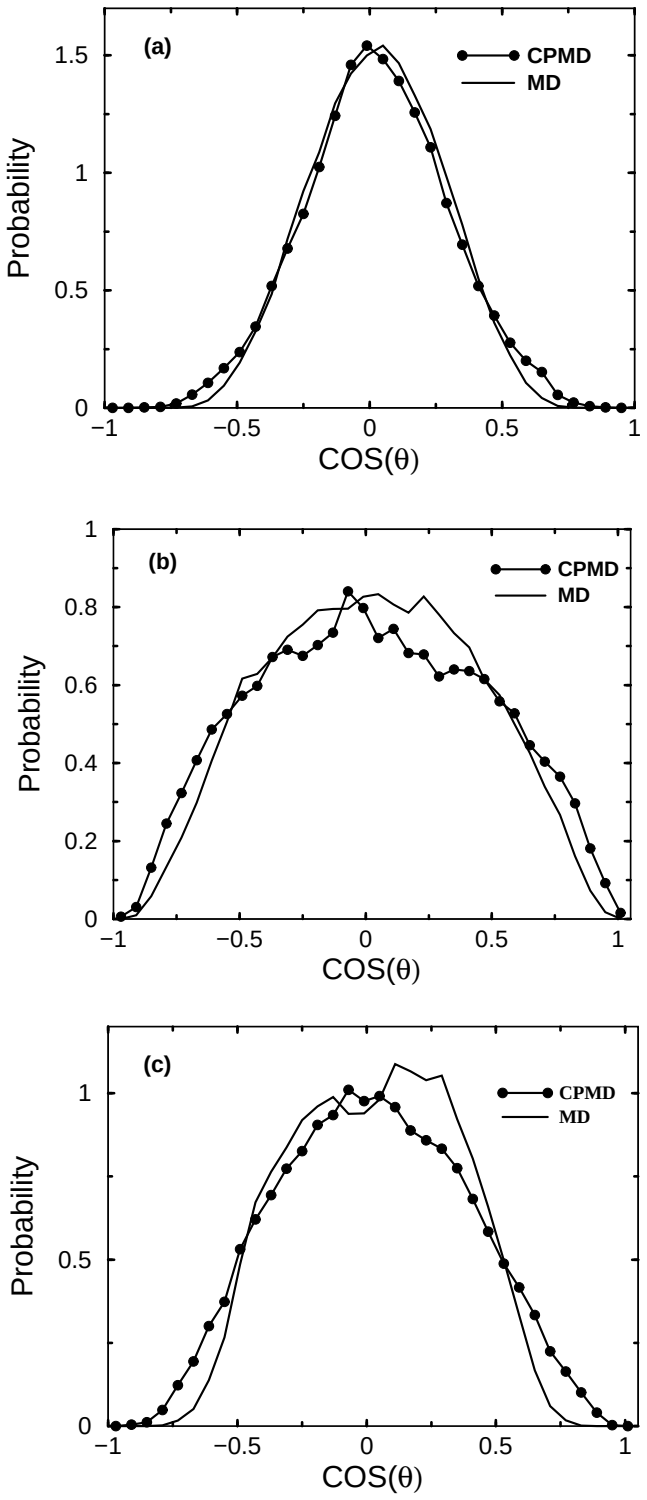

Figure 2.5: **Angular distribution of molecules in the first coordination shell. (a)** $\widehat{OC_1O_a}$**, (b)** $\widehat{OC_1O_b}$**, (c)** $\widehat{OC_1C_2}$**.**

However, when a near neighbor condition based on the C-C distance is imposed (based on the minimum of the first peak of the $g_{CC}(r)$, i.e., 5.7Å), the distribution of OCC angles shows no preference (not shown). One obtains a featureless distribution that indicates an isotropic distribution of carbon atoms around the central molecule. We believe that these results are not inconsistent with each other; rather they indicate that molecules in the closest shell (as defined by the C-O distance cutoff) exhibit orientational preferences which die rather quickly as one increases the shell envelope. It should also be noted that this closest shell is not defined well as the minimum of the first peak in the $g_{CO}(r)$ has a value of around 0.88. This result explains the loss in orientational preferences of near neighbors with increasing distance.

2.3.4 Probability density map

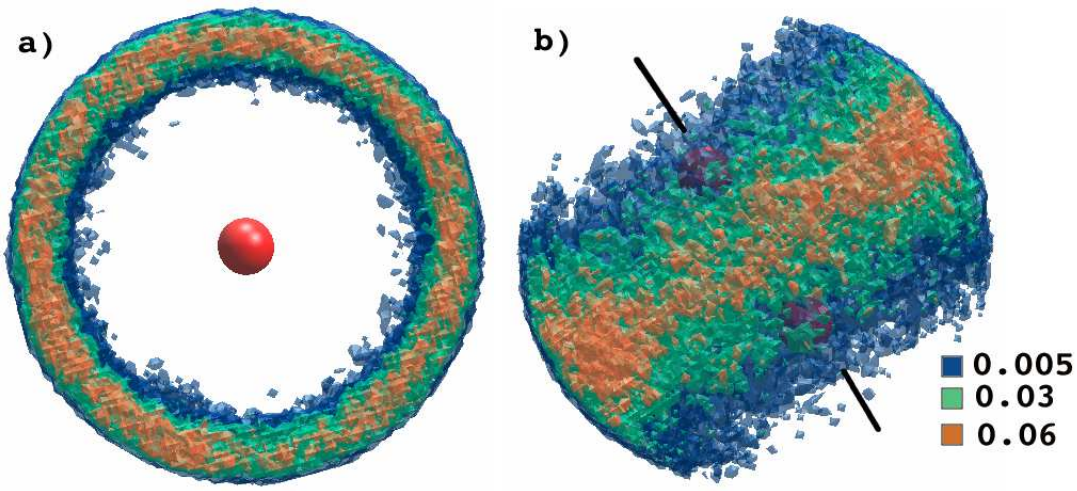

Figure 2.6: **Density isosurfaces of oxygen atoms that belong to molecules in the first coordination shell of CO_2 in supercritical carbon dioxide. The data is ensemble averaged over all the molecules in the system and through the entire CPMD trajectory. a) View along the back-bone axis of the central CO_2, b) Side view: Black line represents CO_2 backbone axis. The different shades are in units of number of oxygen atoms per Å^3. Black sphere denotes the oxygen atom of the central molecule.**

Probability density maps of intermolecular configurations have enhanced our under-

standing in a large number of liquid systems, including liquid water [23, 24]. We have obtained the density map of the first coordination shell in $scCO_2$ as an average over the entire trajectory of the CPMD run, and over all the molecules. In Figure 2.6, we present the arrangement of oxygen atoms which are within 3.3Å from the carbon atom of the central CO_2 molecule. The equatorial ring indicates the absence of neighbors along both the poles. The greater probability for T-shaped intermolecular configurations in the equatorial plane arise from the interaction of the lone pairs on oxygen with the partial positive charge on the central carbon atom. We examine the first coordination shell further by studying the distribution of the coordination number around a molecule.

2.3.5 Coordination number distribution

Figure 2.7 shows the probability of finding a molecule with a coordination number n, of oxygen atoms and of carbon atoms in the first shell. These plots were obtained with distance cutoffs of 3.2Å and 5.0Å which correspond to the first minimum in the respective pair correlation functions those are presented in Figure 2.2. We notice a wide distribution in the number of molecules in the coordination shell, which is likely to determine the extent of charge polarization of a central molecule.

2.3.6 Intramolecular geometry

In the previous chapter we discussed that although the resultant dipole moment of an isolated CO_2 molecule is zero, its 'bond dipole moments' [25–27] are significant as a result of partial charges on individual atoms. The molecule is also highly polarizable. In other words, the geometry and charge density of a central CO_2 can be distorted due to near-neighbor interactions. The extent of this effect on its instantaneous geometry, i.e. intramolecular O-C-O angle (ϕ), has been demonstrated in Figure 2.8 using both CP and classical MD simulations. The distribution from classical MD simulation shows high probability at $\mathrm{Cos}(\phi)$ = -1 and decays rapidly to zero at around $\mathrm{Cos}(\phi) \sim$ -0.985.

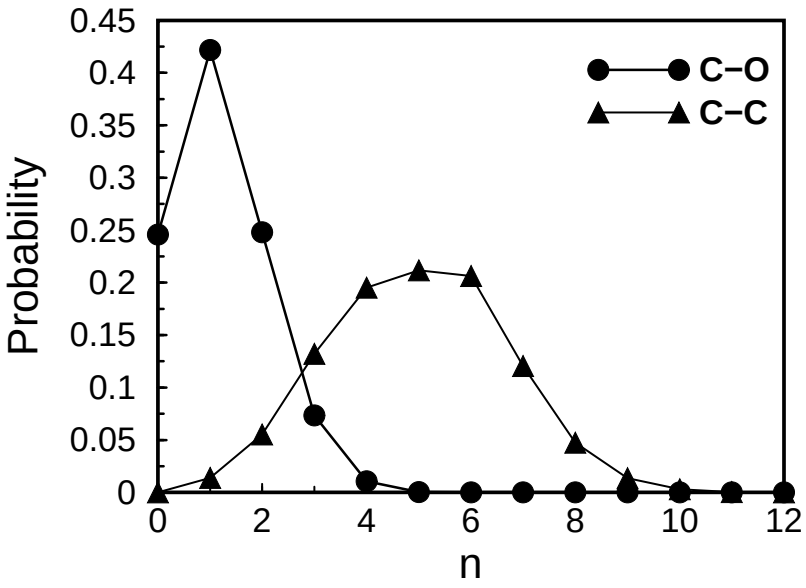

Figure 2.7: **Probability distribution of the number of oxygen (circles) and carbon (triangles) atoms in the first neighbor shell of carbon dioxide in scCO$_2$.**

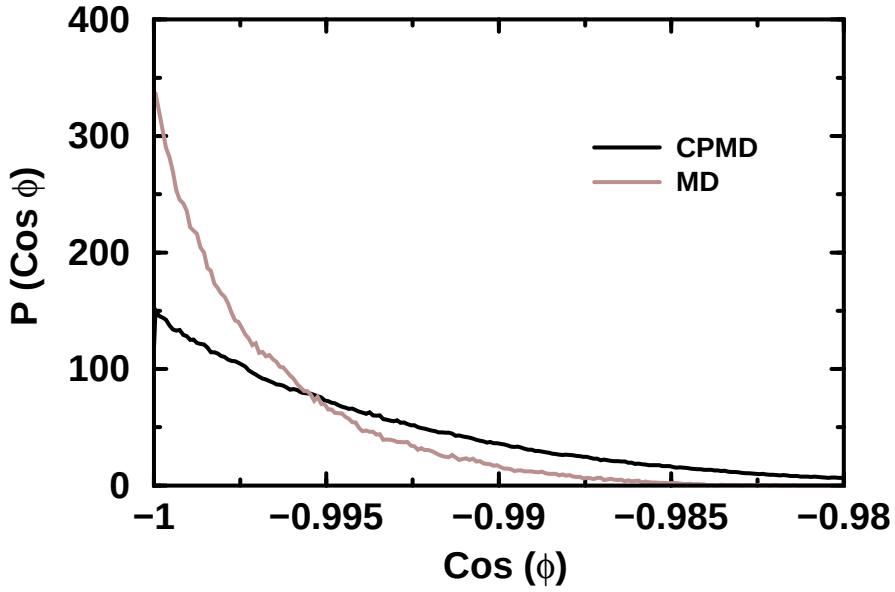

Figure 2.8: **Distribution of instantaneous intramolecular $\widehat{\mathrm{OCO}}$ angle of CO$_2$ in supercritical state using (a) CPMD (black), (b) classical MD (gray) simulations. The bending coefficient for CO$_2$ in the classical EPM2 model [19] is, k$_\theta$ = 1236 kJ/mol/rad^2.**

In contrast, the same from CPMD calculation with long tail depicts lesser probability at Cos(ϕ) = -1 than that obtained from simulation with empirical potential parameters.

Thus, the CPMD distribution indicates higher tendency towards non-linear instantaneous geometry of CO_2.

CPMD calculations of small clusters of CO_2 molecules at 318.15K (one to four molecules) show a progressive distortion of the linear backbone with increasing cluster size. We are thus led to believe that the nonlinearity in the OCO angle in $scCO_2$ is a consequence of the formation of a first neighbor shell. This distortion will manifest as a small deviation of less than 0.01Å in the intramolecular O-O distance from what is expected for a linear molecule. Such a nonlinear molecular geometry has also been observed earlier in charged clusters of CO_2 [28], in CO_2 clusters containing halide molecules or ions [29, 30], and in high pressure phases [31]. We also note that the time averaged structure of any molecule is linear, as expected. There could be two possibilities for this non-linearity in the instantaneous geometry; (1) thermal contribution, and/or (2) intermolecular interactions. In the following chapter, this question has been addressed in details by suppressing one of these variables.

2.3.7 Multipole moment calculation

The deviation from linearity includes a dipole moment to the molecule. At any instant, the dipole moment of a molecule can have two contributions. Firstly, an instantaneous difference in the two C-O bond lengths creates an imbalance of charge distribution on either end of the molecule and leads to a dipole moment that is oriented along the molecular axis. Secondly, the bending of the O-C-O angle, away from the value of 180^o can create a dipole moment and this is a more important contribution. We have calculated the cumulative effect of these contributions by analyzing the instantaneous values of dipole moment and quadrupole moment of individual molecules in the supercritical state. Such calculations of molecular multipole moments have been performed earlier by Silvestrelli *et al* in liquid water [32] using the maximally localized Wannier orbital method [33, 34]. The calculation of Wannier orbitals in the CPMD program employs the Boys' localization

criterion [34]. For CO_2, this method leads to a structure that contains two triple bonds between carbon and oxygen atoms and a lone pair on each oxygen, instead of the Lewis' two double bonded structure [35]. Hence, in our work, the electrostatic molecular multipole moments have been calculated by integrating the charge density distribution in a region centered around each molecule, much in the spirit of Laasonen et al [17]. In the present study, the partitioning of electron charge cloud corresponding to a particular CO_2 molecule is shown schematically in Figure 2.9. For these calculations the coordinates of each molecule were transformed such that their O-O vector was aligned with the z-axis (see Figure 2.10). The molecular dipole moments were calculated as,

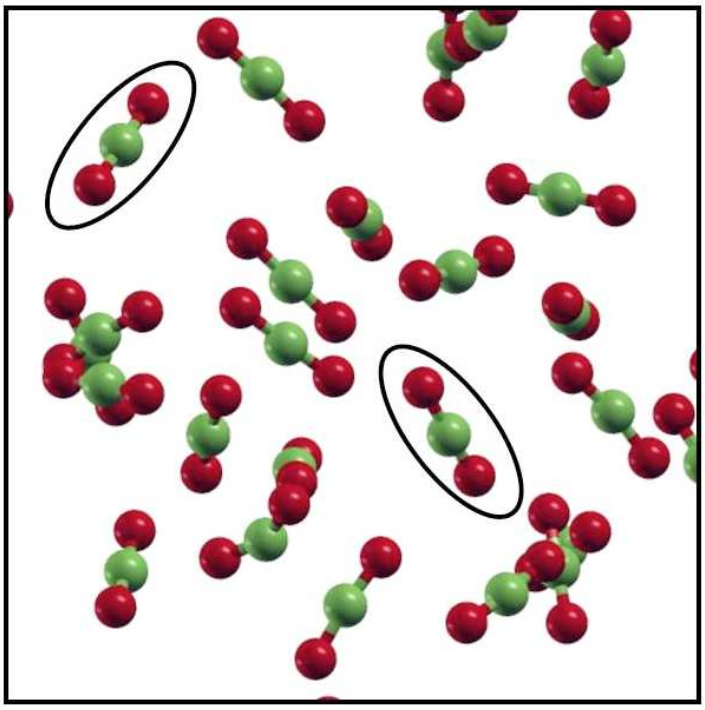

Figure 2.9: **Snapshot of a $scCO_2$ simulation box. The white background represents continuous electron cloud throughout the system. In order to roughly isolate the concentrated charge distribution around a particular solvent molecule, cylindrical box (black contour) has been described around each molecule satisfying the condition that the total charge inside this box should be around -16e.**

$$\mu_i = 2\pi \int_{r=0}^{r_c} \int_{z=-z_c}^{z_c} \rho(\vec{r} - \vec{R}_i)\vec{r} r dr dz \tag{2.3}$$

where μ_i is the dipole moment vector of i-th molecule, and $\vec{R}_i$ is the position of the carbon atom of this molecule. $\rho(\vec{r})$ is the charge density at $\vec{r}$ that contains contributions from the positive ions and the negative electronic density. The expression for the molecular quadrupole moment tensor, $\overleftrightarrow{\mathbf{Q}}$ is given by,

$$Q^i_{mn} = 2\pi \int_{r=0}^{r_c} \int_{z=-z_c}^{z_c} (3r_m r_n - r^2\delta_{mn})\rho(\vec{r} - \vec{R}_i) r dr dz \tag{2.4}$$

where δ_{mn} is the Kronecker delta function and m, n denote Cartesian axes.

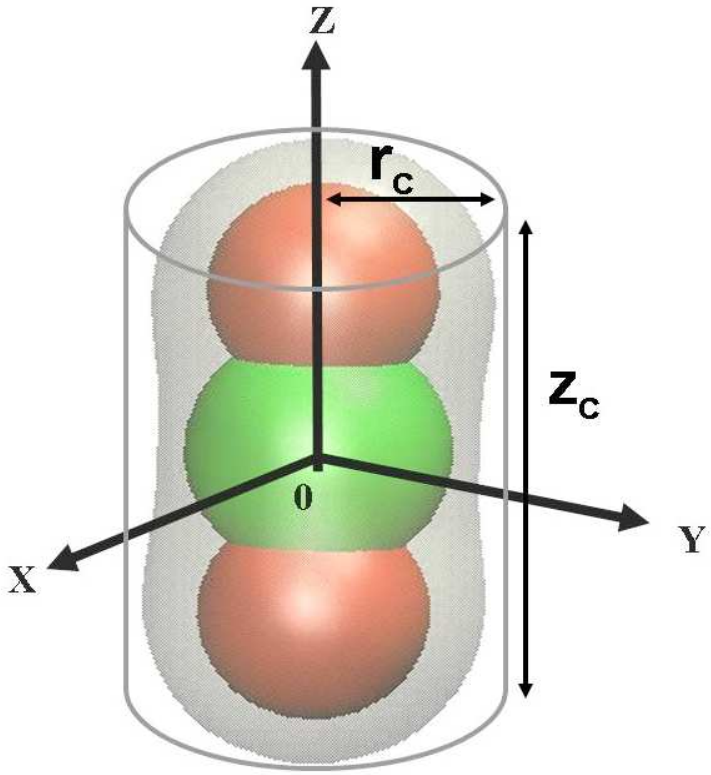

Figure 2.10: **Description of different parameters involved in the multipole moment calculations. The gray region represents electron cloud around a single CO_2 and the cylindrical box has been approximated to accommodate total -16e valence electronic charge belonging to this molecule. r_c and z_c denote the cut-off radius and height of the cylinder, respectively.**

The integrals in Equation (2.3) and Equation (2.4) are calculated in cylindrical coor-

dinates, as the electronic density around each molecule is nearly cylindrical. r_c and z_c denote the cutoff in the radial and the axial directions respectively. In the choice of these parameters, we were guided by the following criteria; (i) the full electronic charge of -16e that is associated with each molecule must be nearly retrieved by integrating the negative charge density within this cylinder, and (ii) the dipole moment vector for an isolated, artificially bent CO_2 molecule calculated using this procedure should nearly coincide with the vector that bisects its two C-O bonds. We have employed cutoff values of 1.3Å and 2.8Å for r_c and z_c respectively. The molecular multipole moment distributions were not much altered with slight changes from these cutoff values.

The ensuing $\overleftrightarrow{\mathbf{Q}}$ matrix is nearly diagonal, as the molecule is quite close to being linear. In the discussion that follows, we report Q_{zz} whose magnitude is twice that of the other two diagonal components. The distributions of the magnitude of dipole and quadrupole moments in $scCO_2$ are displayed in Figures 2.11a and 2.11b respectively. They are asymmetric and exhibit long tails. The mean dipole and quadrupole moments are calculated to be 0.85 Debye and 6.1×10^{-26} esu respectively. The latter should be compared to the value of 4.26×10^{-26} esu that is obtained for a geometry optimized isolated CO_2 molecule in CPMD, and a value of 4.1×10^{-26} esu that is obtained in experiments [36]. The long tail in these distributions could arise from the asymmetry in the distribution of the number of neighbors around a given CO_2 molecule (Figure 2.7). The lack of a complete second neighbor shell, a consequence of the small system size studied here, could also contribute to this tail, apart from the errors involved in apportioning electronic density to each molecule. These need to be checked in calculations of a larger system that employ a localization method to obtain the multipole moments. Thus, we expect the mean value of these moments to decrease to some extent and their magnitudes reported here could be regarded as best estimates.

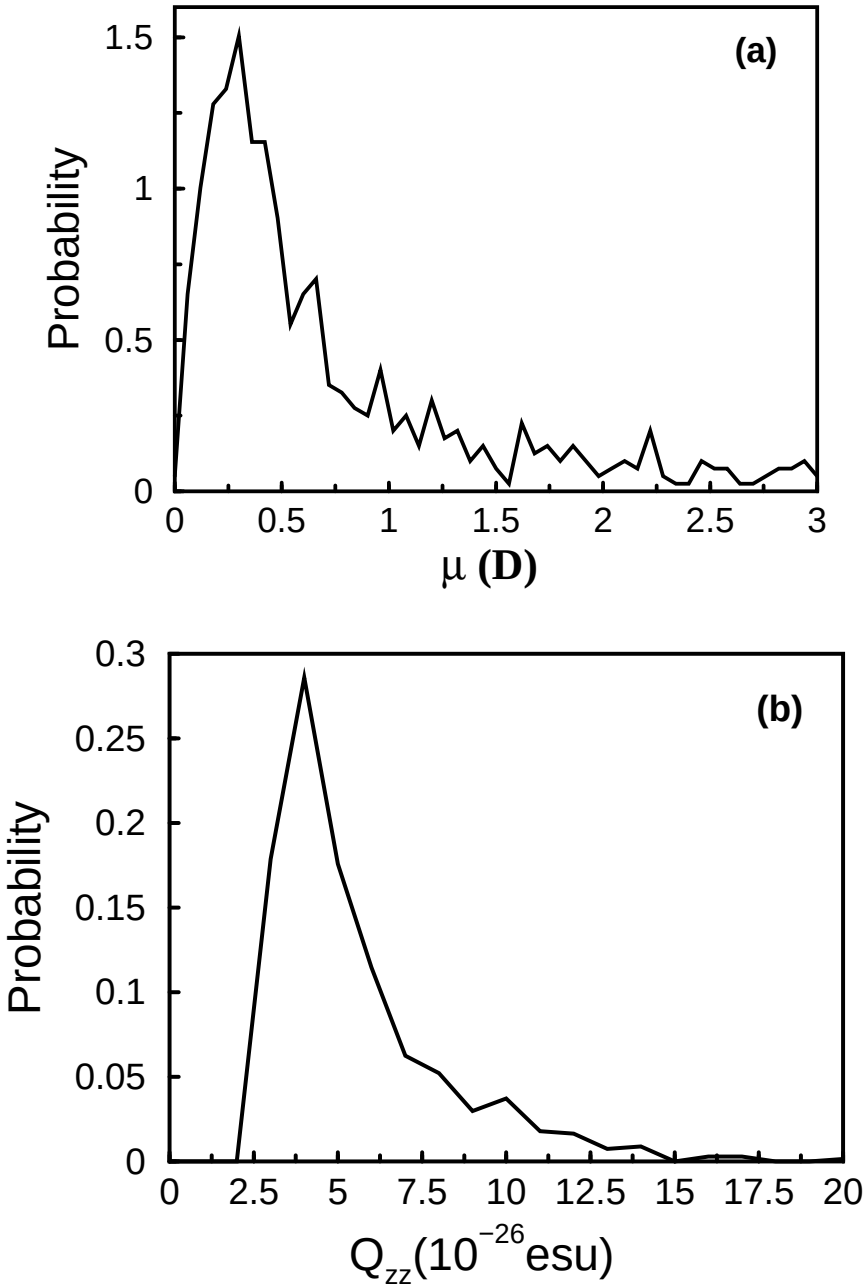

Figure 2.11: **Probability distribution of instantaneous electrostatic multipole moments of CO_2 molecules. a) Magnitude of dipole moment, μ . b) zz component of quadrupole moment, Q. (1 esu=3.3356 X 10^{-14} C.m^2).**

2.3.8 Reorientational Dynamics

The timescales of reorientation of a CO_2 molecule in scCO_2 are crucial to understanding its ability to solvate other species. We examine this quantity through the time correlation

function of the vector $\vec{R}$ [37], that connects the two oxygen atoms of the molecule, as

$$C_{\ell r}(t) = \frac{\langle P_\ell(\vec{R}_i(0) \cdot \vec{R}_i(t))\rangle}{\langle P_\ell(\vec{R}_i(0) \cdot \vec{R}_i(0))\rangle} \tag{2.5}$$

where the angular brackets denote averaging over molecular index i, and over the initial time value 0. P_ℓ is the Legendre polynomial of order ℓ. The time correlation function for ℓ=1 is related to the infrared spectrum and that for ℓ=2 relates to the depolarized Raman spectrum of the system. We show the TCFs for ℓ=1 and ℓ=2, for the systems simulated using CPMD and using MD in Figure 2.12.

The TCF obtained from CPMD, for $\ell = 1$ exhibits a plateau region between 1 ps and about 2 ps, after an initial fast decay, which is absent in the function obtained from MD. The average time constants of this relaxation can be obtained by integration of these functions over time, as,

$$\tau_{\ell r} = \int_0^\infty C_{\ell r}(t)dt \tag{2.6}$$

These values obtained from MD and CPMD are compared in Table 2.2. The CPMD result

Quantity	CPMD	MD	Experiment
τ_{1r} (fs)	620	520	–
τ_{2r} (fs)	268	246	250[a]
D ($10^{-4} \times$ cm^2/sec)	2.29 (MSD) 2.50 (VACF)	2.17 (MSD) 2.62 (VACF)	2.02[b]
Vibrational frequencies (cm^{-1})	1228 (ν_1) 1319 (ν_1) 628 (ν_2) 697 (ν_2) 2309 (ν_3)	– –	1281[c] (ν_1) 1387[c] (ν_1) 667[d] (ν_2) 2318[e] (ν_3)

Table 2.2: Dynamical properties of scCO$_2$.

[a]Estimate from Ref. [38]. [b]Ref. [41]; [c]Refs. [44,45]; [d]for isolated CO$_2$ molecule. [e]Estimate from Refs. [42,43].

for τ_{2r} of 268 fs is in close agreement with the value of 250 fs obtained by ^{17}O relaxation rate (1/T$_1$) measurements by Holz et al [38], of Umecky et al [39], and the classical MD results of Adams and Siavosh-Haghighi [40]. The time constants obtained from MD for

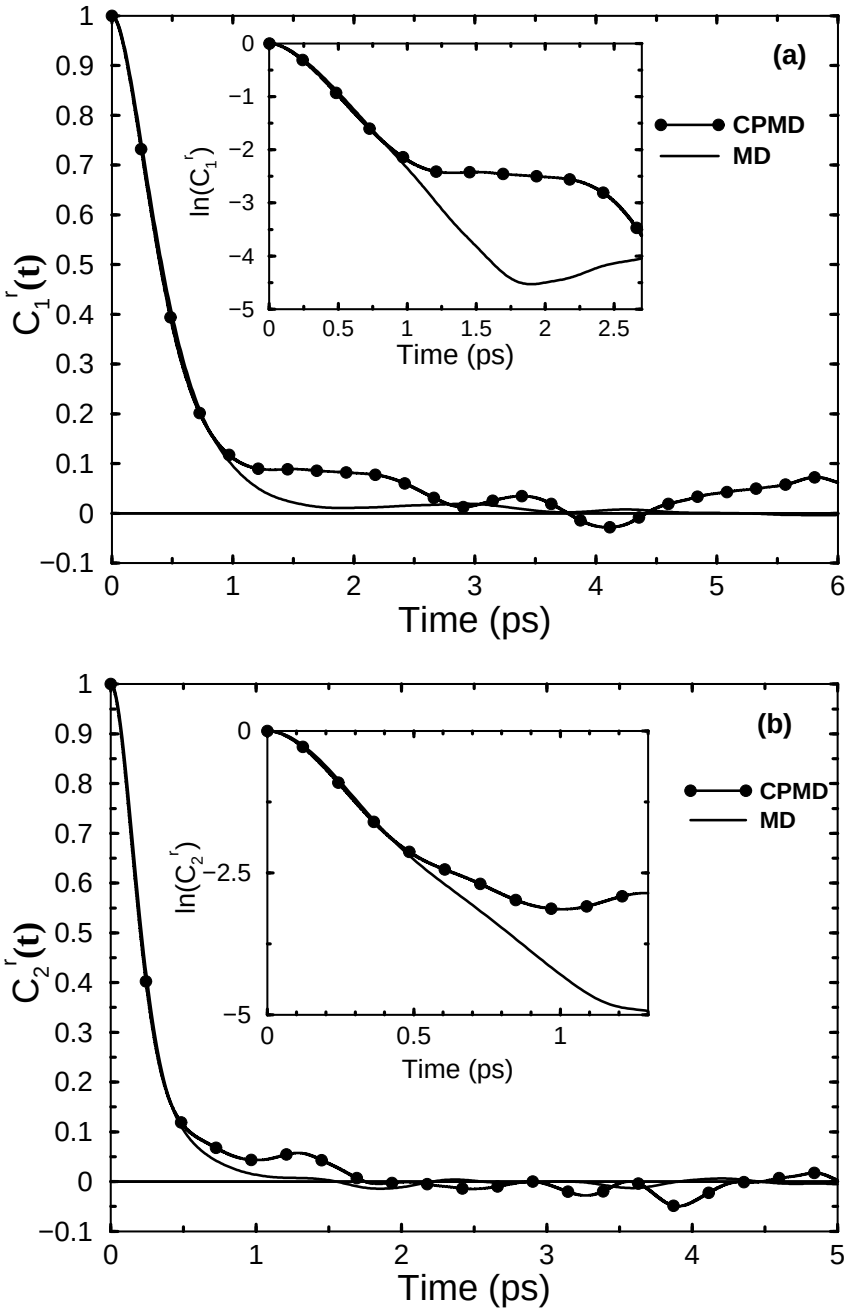

Figure 2.12: **Reorientational time correlation functions, $C_\ell^r(t)$, of CO_2 for (a) $\ell = 1$, and (b) $\ell = 2$. Insets show the short-time decay in logarithmic scale.**

both the functions are smaller than that obtained from the CPMD simulations. Although the TCFs are quite close to each other for times less than 500 fs, they tend to differ at longer times. The initial decay is likely to arise from inertial rotation and classical MD captures it well, while at the intermediate timescales of 1-2 ps, it decays faster than the

CPMD result. The entire length of the CPMD and of the MD analysis trajectories (12 ps and 20 ps respectively) were employed for these calculations. These run lengths are longer than the relaxation times of the TCFs. Thus it is unlikely that the difference between the CPMD and the MD result arises from the shorter run length of the former.

2.3.9 Translational Dynamics

We characterize the translational motion of the CO_2 molecules in the two simulations by the usual quantity, i.e., by their mean squared displacement (MSD). We compare these

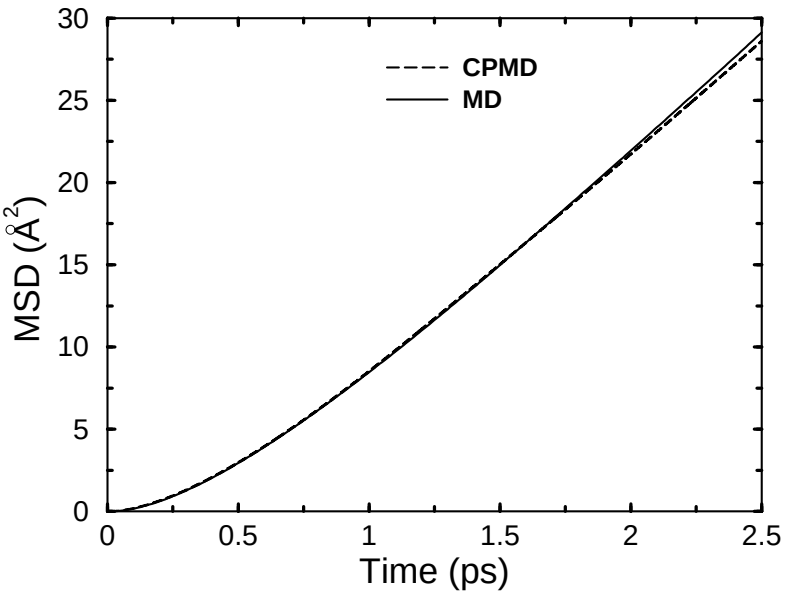

Figure 2.13: **Mean square displacement of CO_2 molecules in supercritical state.**

results in Figure 2.13. Firstly, although the time scales of investigation are small (few picoseconds), the values of displacements are healthy as the system is in the supercritical state. Experience in MD simulations have taught us that the MSD data can exhibit quite different slopes for different blocks of the MD trajectory in a generic liquid. However, in this case since the values of MSD are large, it is possible to trust the data obtained from limited run lengths. The functions for CPMD and for MD are nearly identical. The diffusion coefficient obtained from CPMD calculations is found to be 2.29×10^{-4}cm^2/s,

while that from MD is 2.17×10^{-4}cm^2/s. The results are in good agreement with the value of 2.02×10^{-4}cm^2/s, obtained from the ^{17}O NMR spin-lattice relaxation time measurements [41].

2.3.10 Velocity Correlations and Vibrational Spectrum

The normalized velocity auto time correlation functions of carbon and oxygen atoms are shown in Figure 2.14. The integral of the unnormalized function for carbon atoms is

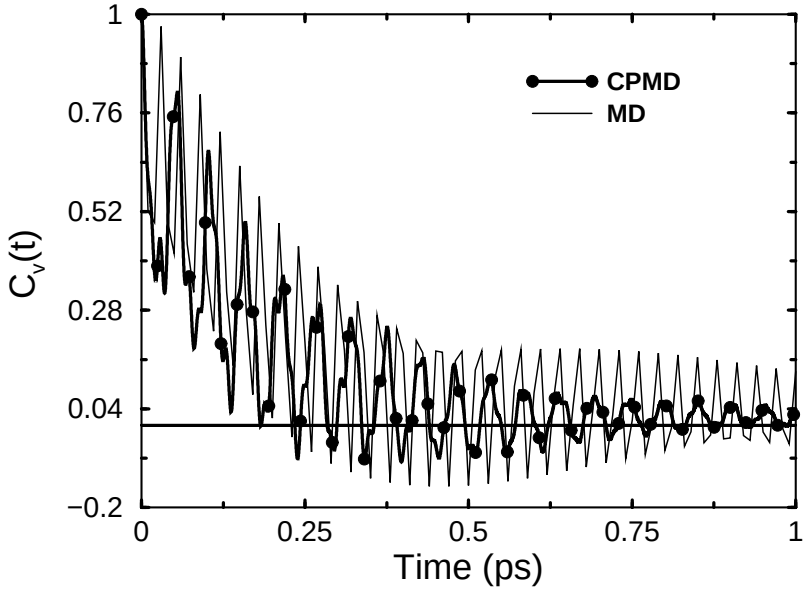

Figure 2.14: **Normalized velocity autocorrelation functions obtained from CPMD and MD simulations.**

related to the diffusion coefficient of the molecule. The value calculated thus from the CPMD run, is found to be $2.50\times\ 10^{-4}$ cm^2/sec and compares well with the estimate obtained from the MSD data that used the Einstein relation. These velocity correlation functions can be Fourier transformed to obtain the power spectrum or the vibrational density of states. We show this data in Figure 2.15. Three distinct features are evident; the asymmetric stretch frequency (ν_3) is observed at 2309 cm^{-1}, in comparison to the experimental value of 2318 cm^{-1} for scCO_2 (estimated from Refs. [42], [43]), and a value

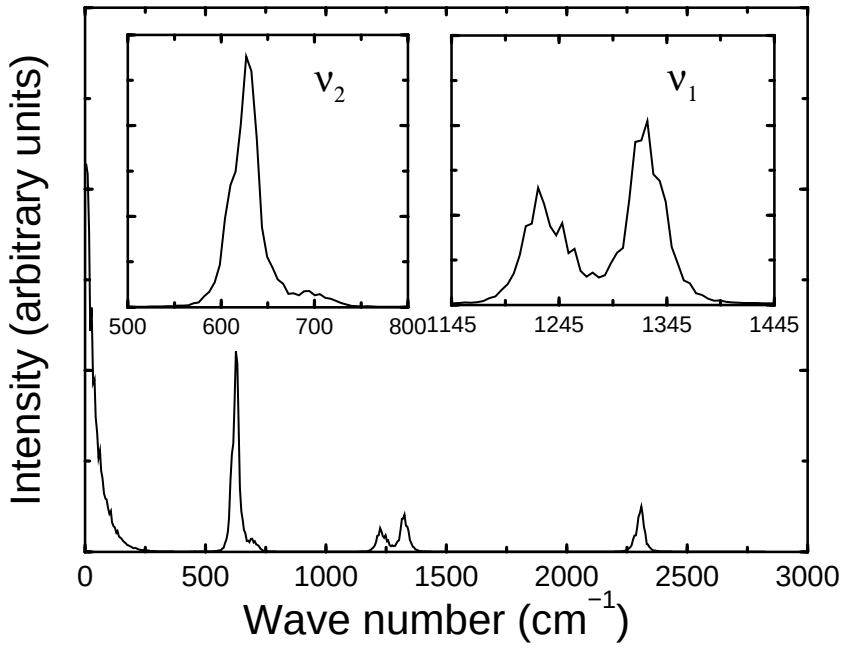

Figure 2.15: **Vibrational spectrum of supercritical CO_2 obtained as the Fourier transform of velocity autocorrelation function from the CPMD calculation. The region around the symmetric stretch mode (ν_1) and the bending mode (ν_2) are shown in an expanded scale in the inset.**

of 2349 cm^{-1} for the isolated CO_2 molecule. The bending mode (ν_2) is two-fold degenerate and is observed at 667 cm^{-1} for the case of an isolated, linear CO_2 molecule. In the CPMD calculations of $scCO_2$, this peak appears at 628 cm^{-1}.

The symmetric stretch (ν_1) in isolated CO_2 is infrared inactive but is Raman active. Usually, this mode is observed as a split peak, the splitting arising from the combination of the fundamental of the symmetric stretch mode and the first overtone of the bending mode, a process called the Fermi resonance. The CPMD vibrational spectrum shows two peaks in this region, one at 1228 cm^{-1}, and the other at 1319 cm^{-1}, probably arising from the same combination. Experimentally, these are observed at 1281 cm^{-1}, and 1387 cm^{-1} respectively in the supercritical state [44, 45] and at 1388 cm^{-1} for the isolated molecule. It is important to note that all the vibrational features observed for $scCO_2$ through the CPMD calculations, show a red shift in the peak frequencies relative to the experimental data for an isolated CO_2 molecule, the shift arising out of intermolecular interactions.

Such a red shift is observed in the experimental vibrational spectrum of scCO2 as well [43], although to a lesser extent than what is observed in these CPMD calculations. The differences between experiments and the current simulations could also be due to the local density approximation employed in our study. At zero frequency, the VDOS obtained from CPMD has a non-zero value, due to the presence of rigid body translational and rotational modes in the system.

2.4 Conclusions

We have performed *ab initio* MD calculations of supercritical carbon dioxide and have compared these results with experiments and against conventional MD simulations that employ empirical potentials. Our calculations used the local density approximation; their accuracy for this system needs to be checked against functionals that are dependent on the gradient of the charge density as well, such as the recently proposed X3LYP functional [46]. Preliminary calculations using the BLYP functional [47] on small clusters of CO_2 show essentially similar intramolecular geometrical features as that reported here. This allows us to place some degree of confidence in our results on $scCO_2$. Expectedly, CPMD calculations agree quite well with experiments both in terms of the structure, and in dynamics. These CPMD calculations could form a baseline for future analyses and comparisons to both theory and to experiment.

The ability of $scCO_2$, despite its low density, and its supposed lack of a molecular dipole moment, to solvate a wide variety of substances has long been a puzzle. Our calculations reveal that (a) the CO_2 molecule possesses an induced dipole moment, however small, that arises out of a change in the internal geometry of the molecule due to a polarization of charge density from intermolecular interactions, and (b) a reasonably ordered near neighbor molecular structure exists at the state point studied here. The combination of these two observations along with the molecular quadrupole moment may partially explain the capacity of $scCO_2$ to solvate other species. Isolated CO_2 has a quadrupole moment

of 4.1×10^{-26} esu [36]. As remarked earlier, the presence of T-shaped near neighbor configurations has been attributed to the non-zero quadrupole moment [12]. The relative strengths of the dipole and quadrupole moments in mediating $scCO_2$-solute interactions needs to be studied further.

We observe a well defined near neighbor structure in the supercritical state. The pair correlation function of intermolecular C-O pairs, exhibits two clear peaks which enabled us to study in detail, the arrangement of molecules around a central CO_2. We find the molecules in the first coordination shell to be arranged in a distorted T-shaped geometry. Although intermolecular distances were found to be marginally larger in the MD calculations, the intermolecular angle distributions from MD were found to be in good agreement with CPMD data.

The reorientational dynamics of CO_2 plays an important role in its ability to solvate other species. In this respect, the CPMD calculations were found to match very well the rotational timescales obtained from NMR experiments. The rotational time constants for relaxation of the first order and the second order reorientational TCFs were found to 620 fs and 268 fs respectively. The MD results for the same agreed with the CPMD data for timescales less than a picosecond, but they do not reproduce the plateau found in the CPMD results between 1 and 2 ps. Hence the time constants obtained from MD calculations were, smaller than that obtained from CPMD. The vibrational density of states obtained from the velocity auto correlation functions of the atoms reproduced the key observations of experiments – a red shift in the frequencies of the modes relative to that for an isolated molecule was observed, and the splitting of the symmetric stretch peak due to Fermi resonance was reproduced in the CPMD calculations. Needless to state, the MD calculations involving no internal degrees of freedom cannot be expected to capture the vibrational modes of the molecules in $scCO_2$.

The results of the present CPMD simulations could be used to refine the interaction parameters of carbon dioxide for use in classical MD simulations. Specifically, the rele-

vance of retaining the linear structure of the molecule in the supercritical state in such simulations, could be examined. In an interesting study on the vibrational relaxation of I_2^- ions in carbon dioxide clusters, Ladanyi and Parson [48] have observed a spontaneous solvent polarization for an artificially constructed hyperflexible solvent model. The marginal differences observed between the CPMD and the MD calculations could also arise from system size effects [10]. Our CPMD calculations involve only 32 molecules – this could influence the results, by artificially suppressing density heterogeneities of length scales larger than 7.5 Å, which is around half of the simulation box length used in the CPMD study. However, we wish to point out that a box of about 15 Å itself is quite large by CPMD standards, and tremendous resources are required to study systems of larger sizes. We had performed MD calculations at two system sizes, one with 32 molecules and the other with 100 molecules and found the structural and dynamical data not to be too dependent on the size of the system. This makes us believe that the CPMD calculations involving 32 molecules are likely to be converged with respect to the size of the system and thus to be realistic of bulk behavior.

Dispersive forces have long been an issue in DFT, and efforts have been made recently to treat van der Waals interactions more accurately [49, 50]. In light of this, the excellent agreement obtained by our CPMD simulations with experiments could be due to a fortuitous cancellation of minor errors, or could point to the dominance of electrostatic interactions in supercritical carbon dioxide. This needs to be studied further. One needs to also compare the results obtained within the local density approximation with that obtained using a functional that includes gradient corrections. The former has been shown to underestimate intermolecular bond lengths [16]. High pressure solid phases of carbon dioxide have been studied using gradient corrected functionals [51], and their use in predicting the properties of $scCO_2$ could be explored.

The enhanced instantaneous electrostatic multipole moments and the solvent structure offer a microscopic explanation for the ability of supercritical carbon dioxide to dissolve a

variety of solutes. The quadrupole moment of CO_2 has been shown to diminish the activation barrier and influence the kinetics in isomerization and charge transfer reactions [52]. Thus, its enhancement in $scCO_2$ over the value for the isolated molecule is significant. The existence of an induced dipole moment could be probed using the method of dielectric relaxation. Such experiments have been performed for $scCO_2$-methanol mixtures [53] and not for pure $scCO_2$. Based on our simulations, we expect a dielectric loss peak in $scCO_2$ to be present at frequencies of the order of 10^{12}Hz. Earlier spectroscopic studies have indicated the interaction of the lone pairs on a carbonyl oxygen in poly(methyl methacrylate) with the carbon atom of carbon dioxide molecule [54]. Our results on the existence of equatorial near neighbor configurations agree with these observations and point to the importance of electrostatic interactions in this green solvent. Successive chapters of this thesis probe these interactions as a function of solvent density and in the presence of solutes.

Bibliography

[1] M. J. Clarke, K. L. Harrison, K. P. Johnston, S. M. Howdle *J. Am. Chem. Soc.* **119**, 6399 (1997).

[2] K. Nagashima, C.T. Lee Jr., B. Xu, K.P. Johnston, J.M. DeSimone, C.S. Johnson Jr. *J. Phys. Chem. B* **107**, 1962 (2003).

[3] B. Chen, J.I. Siepmann, M.L. Klein *J. Phys. Chem. B* **105**, 9840 (2001).

[4] S. Salaniwal, S.T. Cui, P.T. Cummings, H.D. Cochran *Langmuir* **15**, 5188 (1999); S. Salaniwal, S.T. Cui, H.D. Cochran, P.T. Cummings *Langmuir* **17**, 1773 (2001).

[5] S. Senapati, J.S. Keiper, J.M. DeSimone, G.D. Wignall, Y.B. Melnichenko, H. Frielinghaus, M.L. Berkowitz *Langmuir* **18**, 7371 (2002).

[6] P. Cipriani, M. Nardone, F. P. Ricci *Physica B* **241 - 243**, 940 (1998); S. Chiappini, M. Nardone, F. P. Ricci *Mol. Phys.* **89**, 975 (1996).

[7] K. Nishikawa, M. Takematsu *Chem. Phys. Lett.* **226**, 359 (1994); T. Morita, K. Nishikawa, M. Takematsu, H. Iida, S. Furutaka *J. Phys. Chem B* **101**, 7158 (1997).

[8] R. Ishii, S. Okazaki, O. Odawara, I. Okada, M. Misawa, T. Fukunaga *Fluid Phase Equilibria* **104**, 291 (1995); R. Ishii, S. Okazaki, I. Okada, M. Furusaka, N. Watanabe, M. Misawa, T. Fukunaga *J. Chem. Phys.* **105**, 7011 (1996).

[9] G. Tabacchi, C.J. Mundy, J. Hutter, M. Parrinello *J. Chem. Phys.* **117**, 1416 (2002).

[10] S.C. Tucker *Chem. Rev.* **99**, 391 (1999).

[11] J.A. Morrone, M.E. Tuckerman *J. Chem. Phys.* **117**, 4403 (2002);

[12] P. Cipriani, M. Nardone, F. P. Ricci, M. A. Ricci *Mol. Phys.* **99**, 301 (2001).

[13] R. Ishii, S. Okazaki, I. Okada, M. Furusaka, N. Watanabe, M. Misawa, T. Fukunaga *J. Chem. Phys.* **105**, 7011 (1996).

[14] J.Hutter, P. Ballone, M. Bernasconi, P. Focher, E. Fois, S. Goedecker, D. Marx, M. Parrinello, and M.E. Tuckerman, CPMD Version 3.7.2, Max Planck Institut fuer Festkoerperforschung, Stuttgart, and IBM Zurich Research Laboratory, 1990-2003.

[15] D. Vanderbilt *Phys. Rev. B* **41**, 7892 (1990).

[16] K. Laasonen, M.L. Klein *J. Am. Chem. Soc.* **116**, 11620 (1994);

[17] K. Laasonen, M. Sprik, M. Parrinello, R. Car *J. Chem. Phys.* **99**, 9080 (1993).

[18] G.J. Martyna, M.E. Tuckerman, M.L. Klein *J. Chem. Phys.* **97**, 2635 (1992).

[19] J.G. Harris, K.H. Yung *J. Phys. Chem.* **99**, 12021 (1995). A.J. Sillanpaa, C. Simon, M.L. Klein, K. Laasonen *J. Phys. Chem. B* **106**, 11315 (2002).

[20] S. R. P. Rocha, K. P. Johnston, R. E. Westacott, P. J. Rossky *J. Phys. Chem. B* **105**, 12092 (2001).

[21] N.H. March, M.P. Tosi *Atomic dynamics in liquids* (Dover, New York, 1991).

[22] G. Herzberg *Electronic spectra and electronic structure of polyatomic molecules* (Van Nostrand, New York, 1966).

[23] P.G. Kusalik, I.M. Svishchev *Science* **265**, 1219 (1994).

[24] K. Bagchi, S. Balasubramanian, M.L. Klein *J. Chem. Phys.* **107**, 8561 (1997).

[25] P. Raveendran, S. L. Wallen, *J. Phys. Chem. B* **107**, 1473 (2003).

[26] P. Raveendran, Y. Ikushima, S. L. Wallen, *Acc. Chem. Res.* **38**, 478 (2005).

[27] R. S. Berry, S. A. Rice, J. Ross, *Physical Chemistry*, Oxford University Press (2000).

[28] I. A. Shkrob *J. Phys. Chem. A* **106**, 11871 (2002).

[29] D. W. Arnold, S. E. Bradforth, E. H. Kim, D. M. Neumark *J. Chem. Phys.* **102**, 3493 (1995).

[30] H. Gomez, T. R. Taylor, D. M. Neumark *J. Chem. Phys.* **116**, 6111 (2002).

[31] J.-H. Park, C.S. Yoo, V. Iota, H. Cynn, M.F. Nicol, T. Le Bihan *Phys. Rev. B* **68**, 014107-1 to 014107-9 (2003).

[32] P.L. Silvestrelli, M. Parrinello *Phys. Rev. Lett.* **82**, 3308 (1999); P.L. Silvestrelli, M. Parrinello *J. Chem. Phys.* **111**, 3572 (1999).

[33] N. Marzari, D. Vanderbilt *Phys. Rev. B* **56**, 12847 (1997).

[34] G. Berghold, C. J. Mundy, A. H. Romero, J. Hutter, M. Parrinello *Phys. Rev. B* **61**, 10040 (2000).

[35] J.P. Foster, F. Weinhold *J. Am. Chem. Soc.* **102**, 7211 (1980); N. Marzari, I. Souza, D. Vanderbilt, Ψ_k Newsletter **57**, 129 (2003).

[36] A. D. Buckingham, R. L. Disch *Proc. R. Soc. A* **273**, 275 (1963).

[37] A.S. Haghighi, J.E. Adams *J. Phys. Chem. A* **105**, 2680 (2001).

[38] M. Holz, R. Haselmeier, A. J. Dyson, H. Huber *Phys. Chem. Chem. Phys.* **2**, 1717 (2000).

[39] T. Umecky, M. Kanakubo, Y. Ikushima *J. Phys. Chem. B* **107**, 12003 (2003).

[40] J. E. Adams, A.S. Haghighi *J. Phys. Chem. B* **106**, 7973 (2001).

[41] P. Etesse, J.A. Zega, R. Kobayashi *J. Chem. Phys.* **97**, 2022 (1992).

[42] C. Yokoyama, Y. Kanno, M. Takahashi, K. Ohtake, S. Takahashi *Rev. Sci. Instrum.* **64**, 1369 (1993).

[43] J. P. Blitz, C. R. Yonker, R. D. Smith *J. Phys. Chem.* **93**, 6661 (1989).

[44] Y. Yagi, H. Tsugane, H. Inomata, S. Saito *J. Supercrit. Fluids* **6**, 139 (1993).

[45] M. Poliakoff, S. M. Howdle, S. G. Kazarian *Angew. Chem. Int. Ed. Engl.* **34**, 1275 (1995).

[46] X. Xu, W. A. Goddard III *J. Phys. Chem. A* **108**, 2305 (2004).

[47] C. T. Lee, W. T. Yang, R. G. Parr *Phys. Rev. B* **37**, 785 (1988); A.D. Becke *Phys. Rev. A* **38**, 3098 (1998).

[48] B. M. Ladanyi, R. Parson *J. Chem. Phys.* **107**, 9326 (1997).

[49] W. Kohn, Y. Meir, D. E. Makarov *Phys. Rev. Lett.* **80**, 4153 (1998).

[50] M. Kamiya, T. Tsuneda, K. Hirao *J. Chem. Phys.* **117**, 6010 (2002).

[51] S. A. Bonev, F. Gygi, T. Ogitsu, G. Galli *Phys. Rev. Lett.* **91**, 065501 (2003).

[52] J. F. Kauffman *J. Phys. Chem. A* **105**, 3433 (2001).

[53] S. B. Lee, R. L. Smith Jr., H. Inomata, K. Arai *Rev. Sci. Inst.* **71**, 4226 (2000); R. L. Smith Jr., C. Saito, S. Suzuki, S.-B. Lee, H. Inomata, K. Arai *Fluid Phase Equilib.* **194-197**, 869 (2002).

[54] S. G. Kazarian, M. F. Vincent, F. V. Bright, C. L. Liotta, C. A. Eckert *J. Am. Chem. Soc.* **118**, 1729 (1996).

Chapter 3

Evolution of Intermolecular Structure and Dynamics in Supercritical Carbon dioxide with Pressure: An *Ab Initio* Molecular Dynamics Study

3.1 Introduction

We have mentioned in the Chapter 1, that one of the characteristic features of supercritical CO_2 (compressed fluids in general) is its density tunability. Unlike the normal fluids, the density of this solvent can even be doubled by doubling the pressure [1]. The solubility of solid solutes in $scCO_2$ has been shown to increase with increasing pressure of the solvent [2]. Despite being such a facile experimental tool that is employed to tune the properties of the fluid, the effect of pressure on the molecular and intermolecular structure and dynamics in this system remains not well studied. Motivated by this aim, we report

here results of *ab initio* molecular dynamics simulations of $scCO_2$ based on the Car-Parrinello (CPMD) approach [3]. This method has been applied to study a wide variety of liquids and processes therein [4].

Neutron diffraction measurements on high pressure supercritical CO_2 [5,6] show that the intermolecular structure factors depend primarily on the density of the solvent and are insensitive to temperature, in the ranges studied. It is reported that the T-shaped near neighbor configuration [7] around a solvent molecule becomes more structured at higher pressures due to electric multipole interactions. Our earlier works [8,9] on pristine CO_2 (318.15 K and 130 bar), showed that oxygen atoms of CO_2 molecules surround a central molecule in a plane perpendicular to its backbone. Similar near neighbor arrangements have also been reported by other classical MD simulations [10–12]. The near neighbor structure in $scCO_2$ is highly sensitive to its density. In the gas phase, the 'slipped parallel' geometry between two neighboring CO_2 molecules is energetically more favorable than the T-shaped geometry [13,14]. The preference appears to be reversed in the liquid [15]. It was also speculated that CO_2 molecules could adopt non-linear geometries in their instantaneous configurations due to polarization by neighboring molecules in the coordination shell [9]. Thus, although under isolated conditions in its electronic ground state carbon dioxide is a non-dipolar molecule, an induced dipole moment could arise through interactions with near neighbors.

Here, we aim to obtain a microscopic picture of the changes in the intermolecular structure and dynamics of $scCO_2$ that are brought upon by an increase in the pressure. The work can also enable us to distinguish between the contributions from thermal factors and induced polarization due to near-neighbors on the deviation from a linear geometry in the instantaneous configurations of carbon dioxide. In pursuit of these aims, we report here results obtained from extensive *ab initio* molecular dynamics simulations carried out at four different densities along an isotherm at 318.15K. Anticipating our results, we find a marginal, but systematic effect of density on the intramolecular structure, while

the intermolecular structure shows significant changes with increasing pressure. Data on the rotational dynamics of CO_2 molecules are also provided. We present the details of simulation in the next section followed by a description of the results.

3.2 Simulation Details

CPMD simulations [16] have been carried out along an isotherm at 318.15K and at densities of 0.80444, 1.1, 1.216 and 1.4 g/cc. These densities correspond to experimentally observed pressures of 190, 1034, 2000, and 5025 bar respectively [17]. Each simulated system contained 32 CO_2 molecules. The simulations were performed in cubic supercells in the NVT ensemble. In order to obtain a reliable estimate of pressure in ab initio MD simulations, one is required to employ larger values of the plane wave energy cuto than what is used here. Our simulations are carried out under constant density conditions, and the pressure values referenced in the discussion are obtained from experiments [17]. Three dimensional periodic boundary conditions were applied. The box lengths at these densities were 14.27, 12.86, 12.43, and 11.86 Å respectively. Our earlier work [18] had shown that the near neighbor structure is unchanged for systems consisting either 32 or 64 molecules. Hence a smaller system size was employed here.

The CPMD simulations at each state point were started from configurations which were equilibrated by classical MD simulations employing the EPM2 [19] potential model. The equilibration runs in these classical MD simulations were of 100 ps duration each. At the start of each CPMD run, the electronic wavefunctions were quenched to the Born-Oppenheimer surface. CPMD calculations were carried out within the density functional approximation. The exchange and correlation functionals were from the works of Becke [20], and Lee, Yang, and Parr [21] respectively. The electronic orbitals of valence electrons were expanded in a plane wave basis set with an energy cutoff of 70Ry for the orbitals. Norm conserving pseudopotentials of the Troullier-Martins form [22] were employed for the treatment of the core electrons. CPMD simulations using similar

procedures as described here, but of reactive forms of carbon dioxide at much higher temperatures and pressures have been carried out recently [23]. The fictitious mass of electrons was set to 500 a.u. and the equations of motion were integrated with a time step of 4 a.u. (around 0.096fs). Temperature control for the ions was achieved by the use of a Nosé-Hoover chain thermostat [24]. The fictitious electronic kinetic energy was seen to be conserved throughout the molecular dynamics trajectory without the use of a electronic thermostat. In order to achieve better ensemble averaged properties of the solvent, the analysis run lengths at 1.216 and 1.4 g/cc were higher than that at lower densities. Leaving a short span of 2 ps for equilibration at all the densities, the results at 0.80444, 1.1, 1.216, and 1.4 g/cc were analyzed over 13, 13, 18.6, and 21.3 ps respectively. The value of the mean squared displacement of CO_2 molecules in the densest system was found to be 55Å^2 at 7 ps. Hence, we are satisfied that the molecules are labile and that the structural data reported here are well averaged.

3.3 Results and Discussion

3.3.1 Structure

Pair correlation function

The intermolecular structure of pure carbon dioxide in the supercritical state has been studied by neutron diffraction measurements [5, 15] at densities ranging from 11 to 15 molecules/nm^3 over a wide variety of temperatures. Our work reported here consists of systems at densities varying between 11 to 19 molecules/nm^3. Hence a comparison between our *ab initio* results and the neutron data is possible.

The partial radial distribution function, $g_{CC}(r)$ shown in Figure 3.1 exhibits a monotonic shift in the position of the first peak towards lower distances with increase in pressure. In addition, the peak gets narrower indicating a better definition of the first coordination shell.

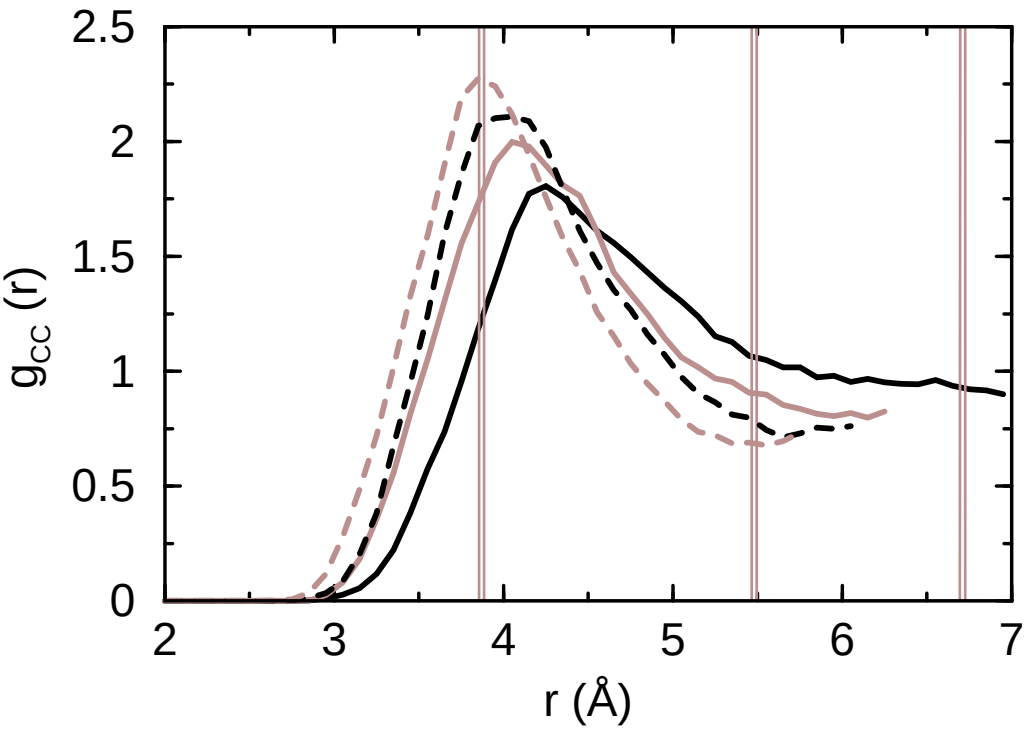

Figure 3.1: **Intermolecular partial radial distribution functions between C-C pairs of CO_2 molecules at densities of 0.80444 (solid black), 1.1 (thick solid gray), 1.216 (dashed black), and 1.4 (dashed gray) g/cc under supercritical conditions at 318.15K. The thin gray vertical lines are the same function for crystalline CO_2. The latter are not completely shown along the y-axis**

Significant changes in the solvent structure can be observed however, in the intermolecular $g_{CO}(r)$ which is shown in Figure 3.2. The first peak at the lowest density is present at 4.2Å and it shifts to shorter distances with increasing density, as expected. Interestingly, a hump develops in the first peak at moderate pressures and transforms into a distinct pre-peak at the highest density studied, at 1.4 g/cc. This feature is present at around 3.1Å . These observations are found to be consistent with the radial distribution functions obtained from neutron scattering measurements [15]. In order to investigate the origin of this new feature at 3.1Å , we have examined the crystal structure of α-CO_2, in its Pa-3 form [25,26]. In a unit cell of the crystal, CO_2 molecules occupy the face centered cubic sites and the orientations of the molecular backbone axes are parallel to the body

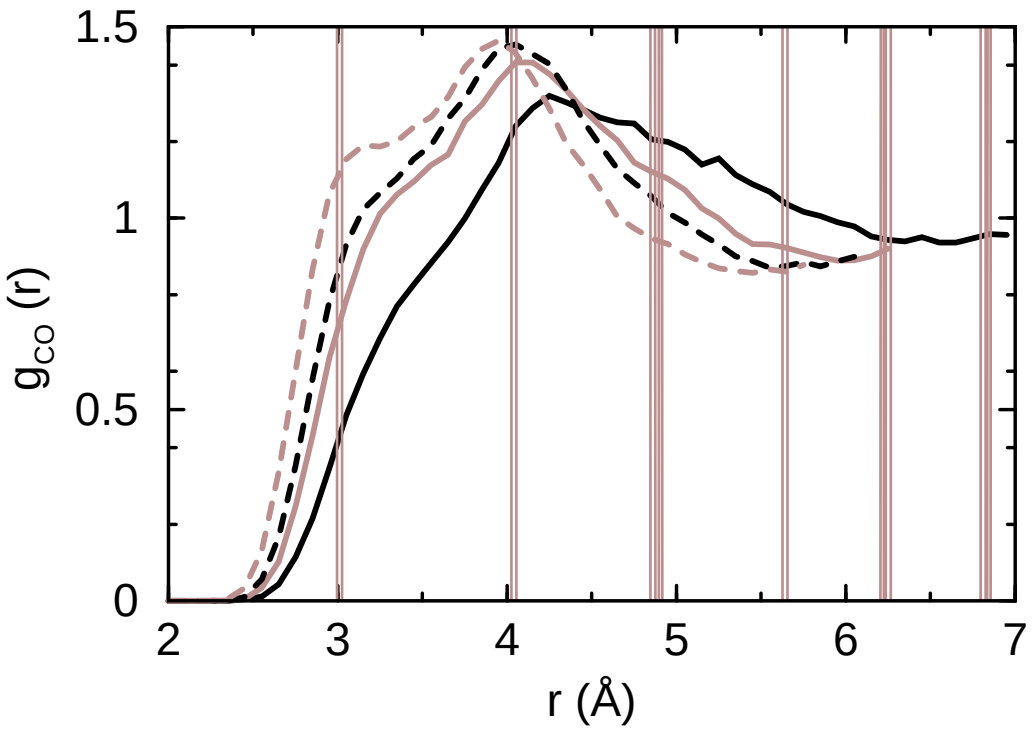

Figure 3.2: **Intermolecular partial radial distribution functions between C-O pairs of CO_2 molecules, with the same description as in Figure 3.1**

diagonals.

Shown in the same figure are the pair correlation functions obtained from the crystal. One can observe the presence of a strong peak at 3.0Å for the crystal which is quite close to the pre-peak observed in $scCO_2$ at 1.4 g/cc. It is worthy to point out here that the density of the crystal is 1.76 g/cc. Despite the difference in the density between $scCO_2$ at 1.4 g/cc studied in our simulations and that of the crystal, the distance from the nearest oxygen to a central carbon is approximately the same. This comparison is further validated by an examination of the second peak in theg_{CO}(r) which is present at 3.9Å and 4.05Å in the high density fluid and the crystalline phases respectively. Figure 3.3 shows the running coordination numbers of intermolecular oxygen atoms around a carbon in $scCO_2$ at 1.4 g/cc and in the crystal. The curve for the former closely follows the data for the crystal, indicating that near-neighbor spatial correlations in $scCO_2$ at the highest

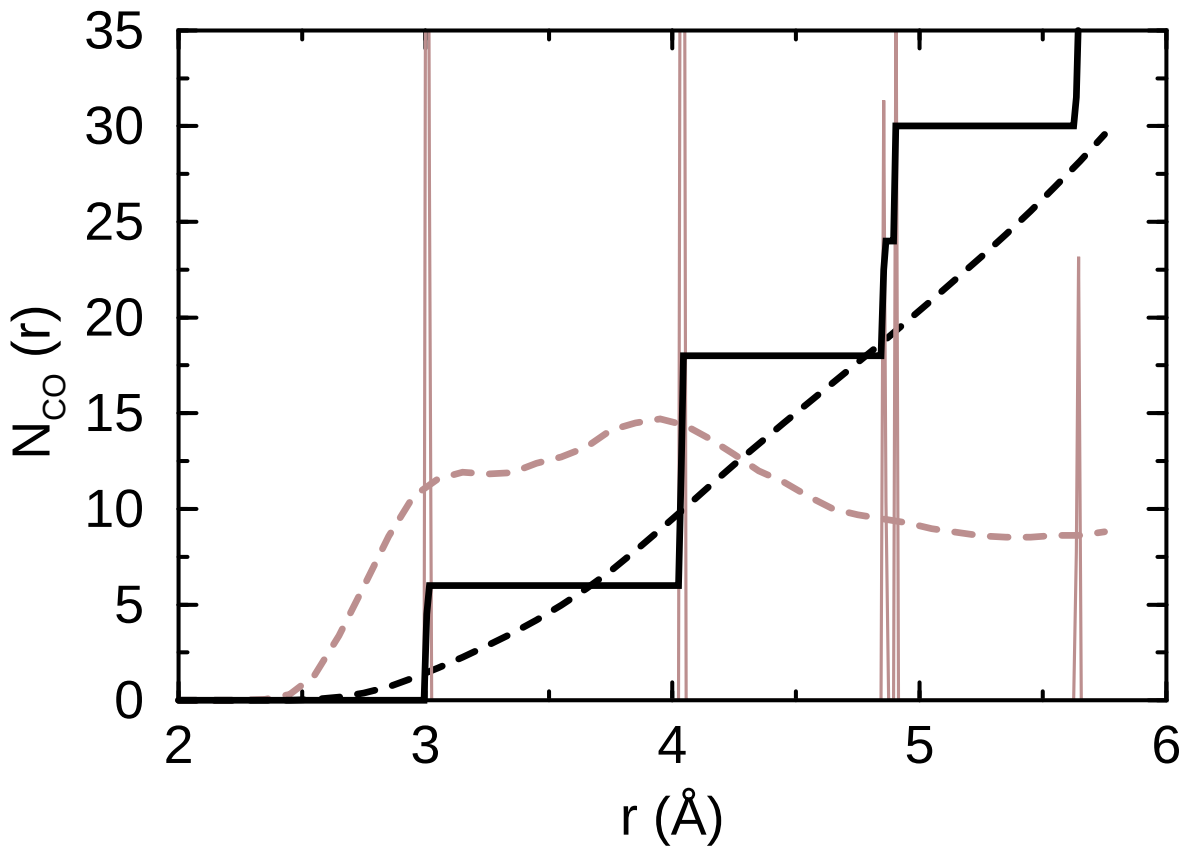

Figure 3.3: **Comparison between running coordination numbers $N_{CO}(r)$, of oxygen atoms surrounding a central carbon atom in the crystal (solid black) and in the supercritical fluid at 1.4 g/cc (dashed black). The corresponding pair correlation functions are also shown in solid gray and dashed gray lines respectively. The $g_{CO}(r)$ for the supercritical fluid has been multiplied by a factor of 10, and that for the crystal is incompletely shown.**

density studied here possesses features which are comparable to that in the crystal.

Atomic probability density map

In order to identify the location of the near neighbor oxygen atom around a central CO_2 molecule in $scCO_2$, we have calculated the three dimensional atomic probability density map. Shown in Figure 3.4(a) is this data for the system at 1.4 g/cc, where isosurfaces in two shades are seen.

The isosurface values for both are the same, 0.07 atoms/Å^3, which is about twice the

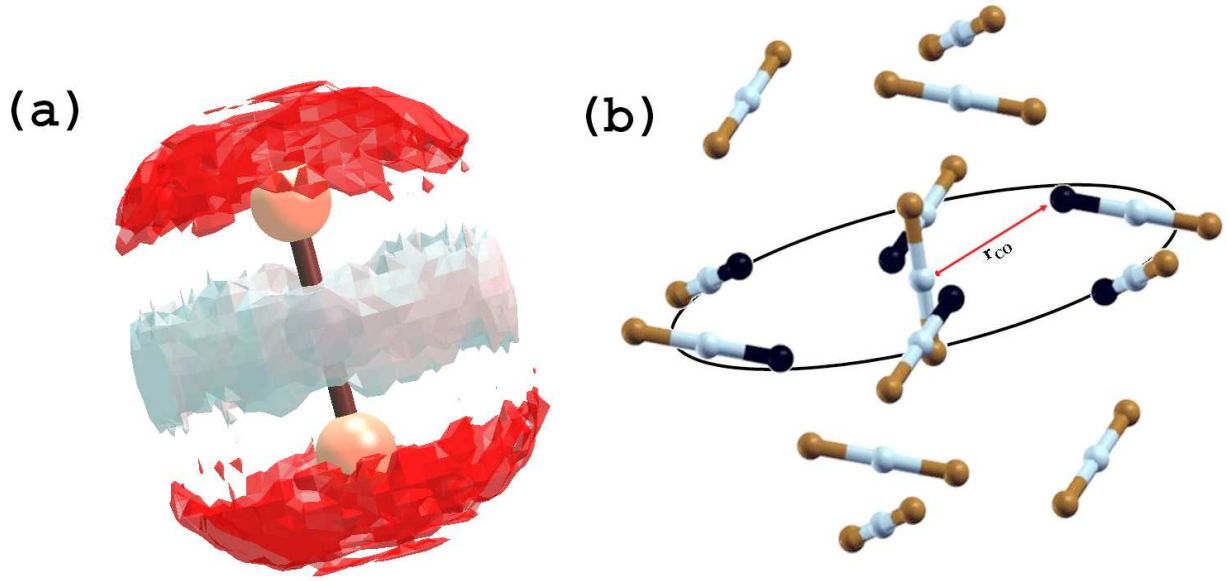

Figure 3.4: **(a) Probability density map for the occurrence of neighboring oxygen atoms around a central CO_2 molecule with two different conditions on the intermolecular C-O separation, r_{CO} : (i) $r_{CO} < 3.4$Å (gray isosurface) and (ii) $3.6 < r_{CO} < 4.3$Å (red isosurface). The isosurface values for both the surfaces is 0.07 oxygen atoms/Å^3 which is about twice the mean density of oxygen atoms in the system. (b) First coordination shell of CO_2 molecules in the crystal, where the C-C distance is 3.9Å . The six closest oxygen atoms which are located near the equatorial plane are shown as black spheres. The ellipse is a caricature of this plane. Carbon atoms are shown in white and oxygen atoms are in gray.**

mean density of oxygen atoms in this system. The surface in gray exhibits the location of oxygen atoms of neighboring CO_2 molecules which fall within a distance of 3.4Å from a central carbon atom, while that in black are for oxygens present at distances between 3.6 and 4.3Å. We can thus infer that the oxygen atoms which contribute to the new pre-peak at 3.1Å in the $g_{CO}(r)$ are mostly located on the equatorial plane around a central carbon dioxide molecule, while those which contribute to the primary first peak present at 3.9Å are predominantly located in the polar regions around a central CO_2. This interpretation is further aided by a comparison of the near neighbor structure in crystalline carbon dioxide. Shown in Figure 3.4(b) is the configuration of the closest twelve neighbors i.e., the first coordination shell (based on intermolecular C-C distance)

around a central CO_2 in the crystal. Around a molecule which is aligned along the z-axis, six molecules lie in or near the equatorial plane. Six oxygen atoms from this group, one from each molecule, form the first oxygen coordination shell around the carbon of a central molecule, at a distance of 3.02Å. Six other molecules are present near the poles of the central molecule. Their oxygen atoms form the second oxygen shell, at a distance of 4.05Å. The parallels between the crystal structure analyzed in this fashion, and the intermolecular structure in the fluid at the density of 1.4 g/cc is striking and lends further credence to our interpretation of the intermolecular structure in $scCO_2$ at high densities.

We shall now examine the orientational order of near neighbor molecules and its evolution with density.

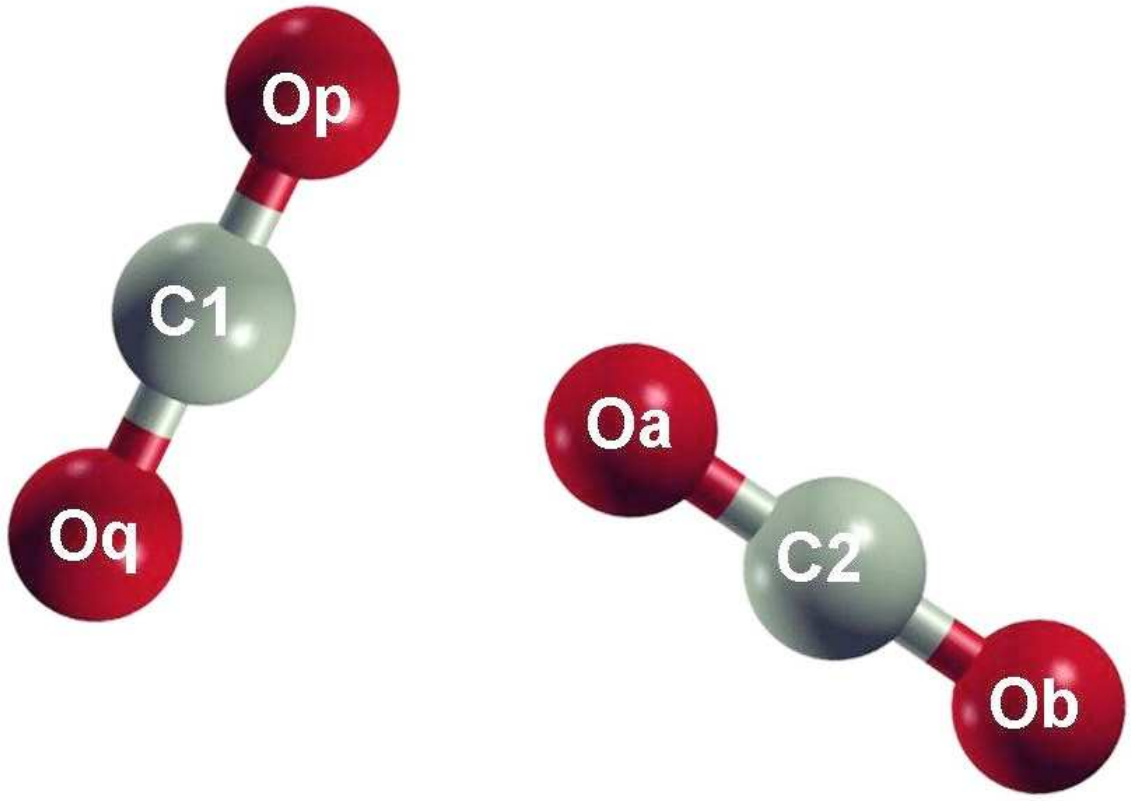

Figure 3.5: **Schematic depicting a typical near neighbor arrangement, which also defines the nomenclature used in the discussion. C_1 is the carbon of the central molecule and O_a is the intermolecular oxygen atom closest to it.**

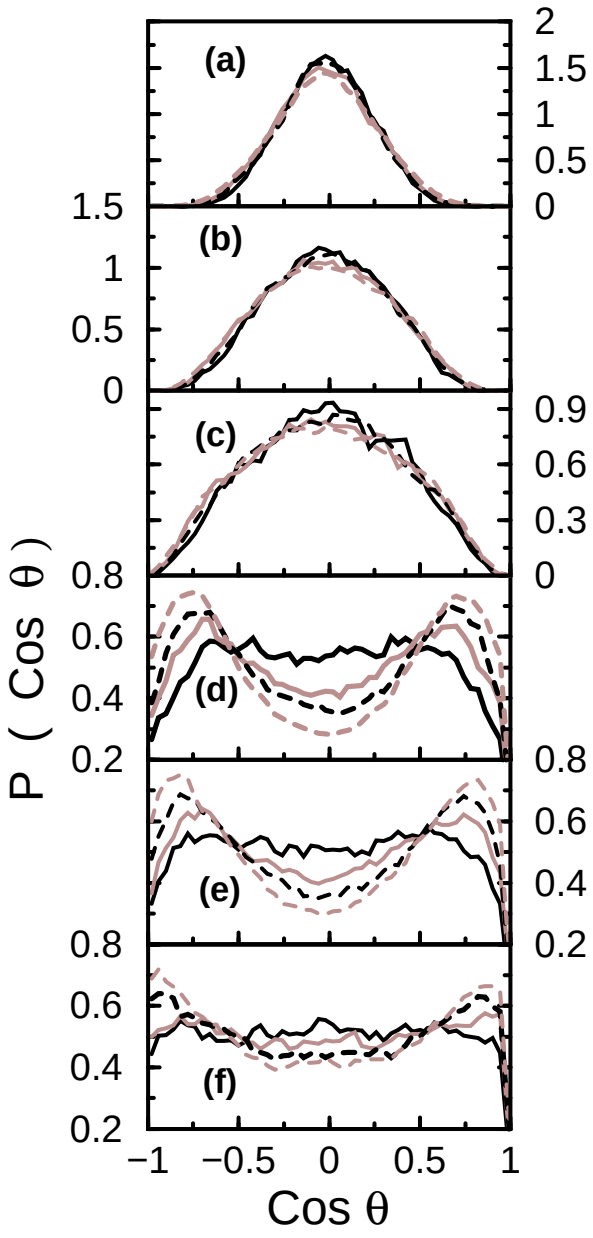

Figure 3.6: **Probability distributions of $\widehat{O_pO_q} \cdot \widehat{C_1O_a}$ (a, and d), $\widehat{O_pO_q} \cdot \widehat{C_1C_2}$ (b, and e), and $\widehat{O_pO_q} \cdot \widehat{C_1O_b}$ (c, and f) with C_1O_a cut-off (i) within 3.4Å (a, b, c); (ii) between 3.6 and 4.3Å (d, e, f). The distributions correspond to the following density values: 0.80444 (solid black line), 1.1 (solid gray line), 1.216 (dashed black line), and 1.4 g/cc (dashed gray line).**

In order to proceed further, we illustrate a typical near neighbor configuration in Figure 3.5. C_1 is the central carbon atom bonded to O_p and O_q. The intermolecular oxygen atom closest to a carbon is denoted as O_a and the farther one as O_b. We are interested in finding out the orientation of near neighbor pairs of molecules in $scCO_2$. The analysis has been divided into two parts, based on the C_1-O_a distance : (i) within the first pre-peak of $g_{CO}(r)$, i.e., within 3.4Å, and (ii) between 3.6-4.3Å. Figure 3.6 exhibits the probability distributions of angles between the unit vector, $\widehat{O_pO_q}$ and various intermolecular vectors at all the densities. The distributions in Figure 3.6a-c exhibit a preference for cosθ values around zero for a distance cut off of 3.4Å, indicating that the closest neighboring molecules prefer a T-shaped or to be more precise, a distorted T-shaped configuration. This feature in the near neighbor arrangement is present irrespective of the system density and only a marginal effect of pressure on these distributions is observed. On the other hand, P(Cos θ) plots for C_1-O_a distances between 3.6 and 4.3Å show (Figure 3.6d-f) a pronounced effect of pressure on intermolecular orientation. At the lowest density, 0.80444 g/cc, the distribution is almost isotropic in nature, whereas two distinct peaks at around 140 and 40^o angles appear at higher densities. Thus, a pair of CO_2 molecules separated by distances between 3.6 and 4.3Å favor the 'slipped parallel' configuration at high pressures.

CO_2 geometry

Having studied the intermolecular ordering as a function of pressure, we now examine the intramolecular geometry of CO_2 with increasing pressure. We have learnt that increasing pressure decreases intermolecular distances. In Figure 3.7, we show the probability distributions of intramolecular O-C and O-O distances in $scCO_2$.

Although the distributions narrow down with increasing pressure, the mean values of O-C and O-O distances decrease only negligibly, by about 0.002 to 0.003Å. Shown in Figure 3.8 are the intramolecular angle distributions calculated at different densities. The pressure dependence of the tail region of the O-C-O angle distribution clearly shows that

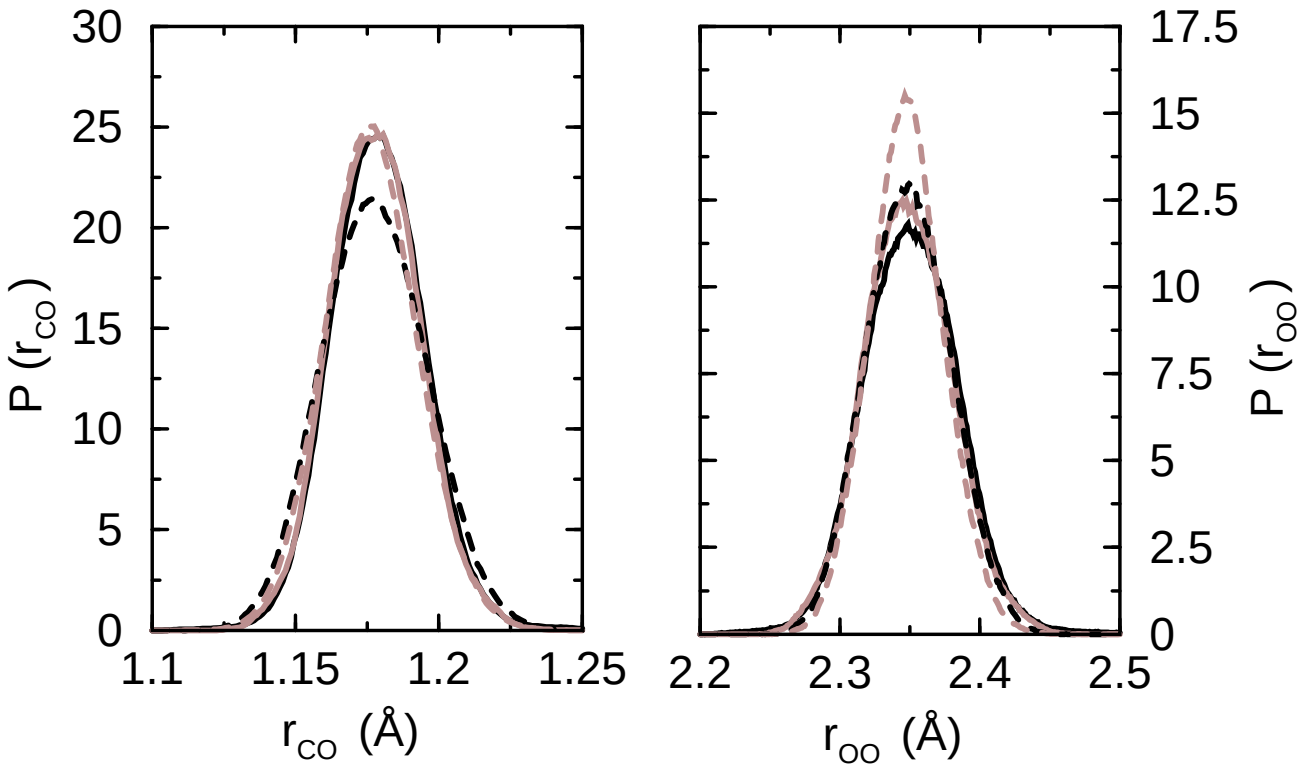

Figure 3.7: **Probability distributions of the intramolecular C-O (r_{CO}) and O-O (r_{OO}) distances. The distributions correspond to the following density values: 0.80444 (solid black line), 1.1 (solid gray line), 1.216 (dashed black line), and 1.4 g/cc (dashed gray line).**

increasing density tends to make the molecules closer to linearity.

The angle distributions obtained from the CPMD simulations are compared with those obtained from classical MD simulations which employed rigid bond lengths and a harmonic potential governing the O-C-O angle (k_θ = 1236 kJ/mol/rad^2). The distribution of instantaneous angles obtained from the classical simulations exhibits a much higher propensity for a linear geometry than the one from CPMD. This contrasting behavior between the classical and CPMD simulations and the pressure dependence observed in the CPMD angle distributions can be rationalized as due to polarization effects induced by a changing near neighbor environment.

We believe that the deviation from linearity in the instantaneous geometry of CO_2

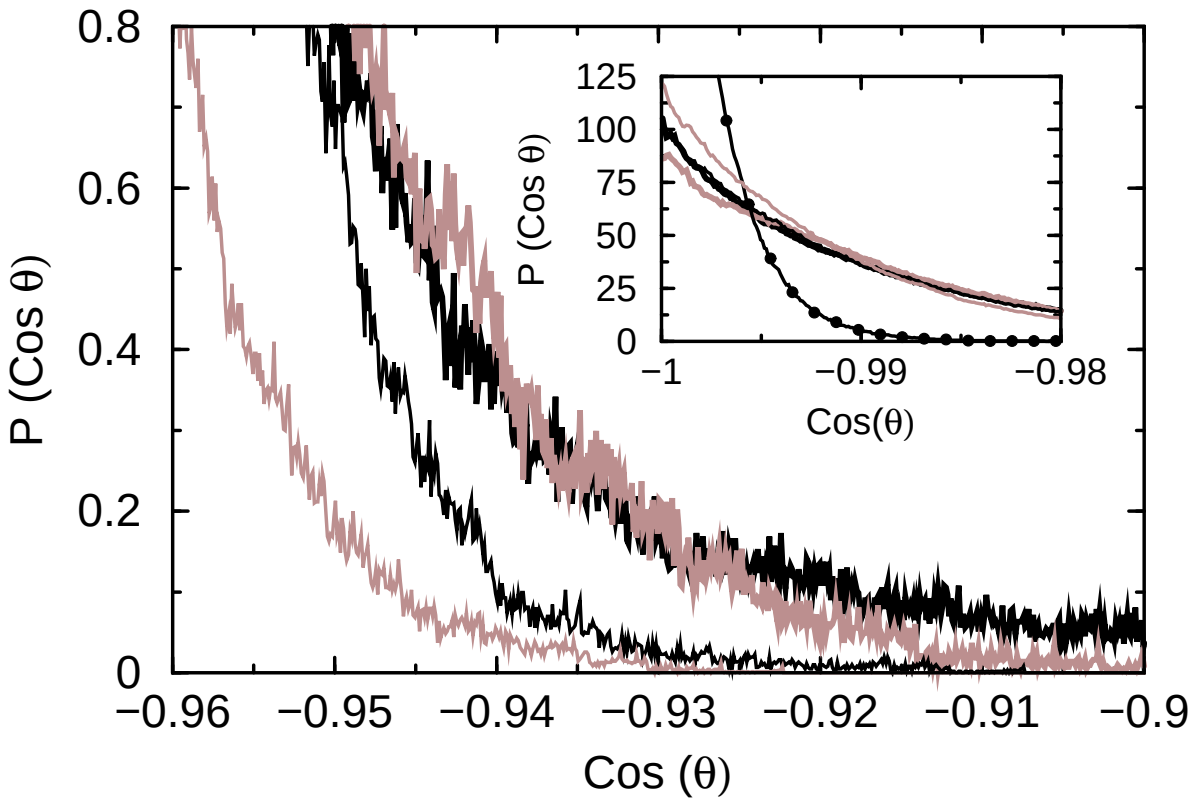

Figure 3.8: **Probability distributions of the intramolecular OCO angle θ, of CO_2 molecules at the following densities: 0.80444 (thick black line), 1.1 (thick gray line), 1.216 (thin black line), and 1.4 g/cc (thin gray line). The corresponding classical MD result with a harmonic bending potential for the system at a density of 1.4 g/cc is shown in black circles. Inset shows the full distributions, and the main body highlights the tail regions.**

could have two underlying causes: (i) thermal fluctuations and (ii) the geometric distribution of near neighbors on or close to the equatorial plane around a central CO_2 molecule. Thermal effects are identical for all the four systems studied as the simulations have been conducted at the same temperature, 318.15K. Hence any differences in the intramolecular angle distributions between the systems, however marginal, must be ascribed purely to an increase in density. Inhomogeneities of molecular density in the instantaneous near neighbor environment are likely to polarize a central CO_2, causing it to deviate away from a linear geometry. This is more likely to happen at lower densities than at higher densities. At lower densities in the supercritical state, a molecule is likely to be surrounded by fewer neighbors, leading to an anisotropic environment which in turn, can polarize a

central CO_2. At higher densities, the polarization effects from neighbors are likely to cancel each other, due to a progressively increasing homogeneous neighborhood. Our results on the intramolecular distance and angle distributions can thus be rationalized. Needless to state, in the crystalline PA-3 structure, the molecules are linear. Thus the trend towards an instantaneous linear geometry with increasing pressure in the supercritical state observed here is reasonable.

3.3.2 Dynamics

Rotational relaxation

Increasing solvent density can have a marked effect on solvent dynamics. A crucial quantity to study in this regard is the rotational relaxation of carbon dioxide molecules, which can be investigated through NMR experiments [27, 28]. In particular, these experiments probe the ^{17}O quadruple relaxation time of carbon dioxide, from which the reorientational relaxation time can be derived. Figure 3.9 depicts the calculated orientational correlation functions for CO_2 at different solvent densities. Consistent with earlier observations [29, 30], the rotational correlation functions are found to be quadratic in nature at low time scales at all densities.

The orientational correlation function is defined as,

$$C_\ell^r(t) = \frac{\langle P_\ell(\mathbf{u_i}(0) \cdot \mathbf{u_i}(t))\rangle}{\langle P_\ell(\mathbf{u_i}(0) \cdot \mathbf{u_i}(0))\rangle} \tag{3.1}$$

where $\mathbf{u}_i$ represents the unit backbone vector of i^{th} CO_2 molecule and ℓ represents the order of Legendre polynomial. The integral correlation time can be calculated as,

$$\tau_\ell^r = \int_0^\infty C_\ell^r(t)dt \tag{3.2}$$

The C_1^r correlation functions at 0.80444, and 1.1 g/cc decay to zero within 4 ps. τ_1^r at

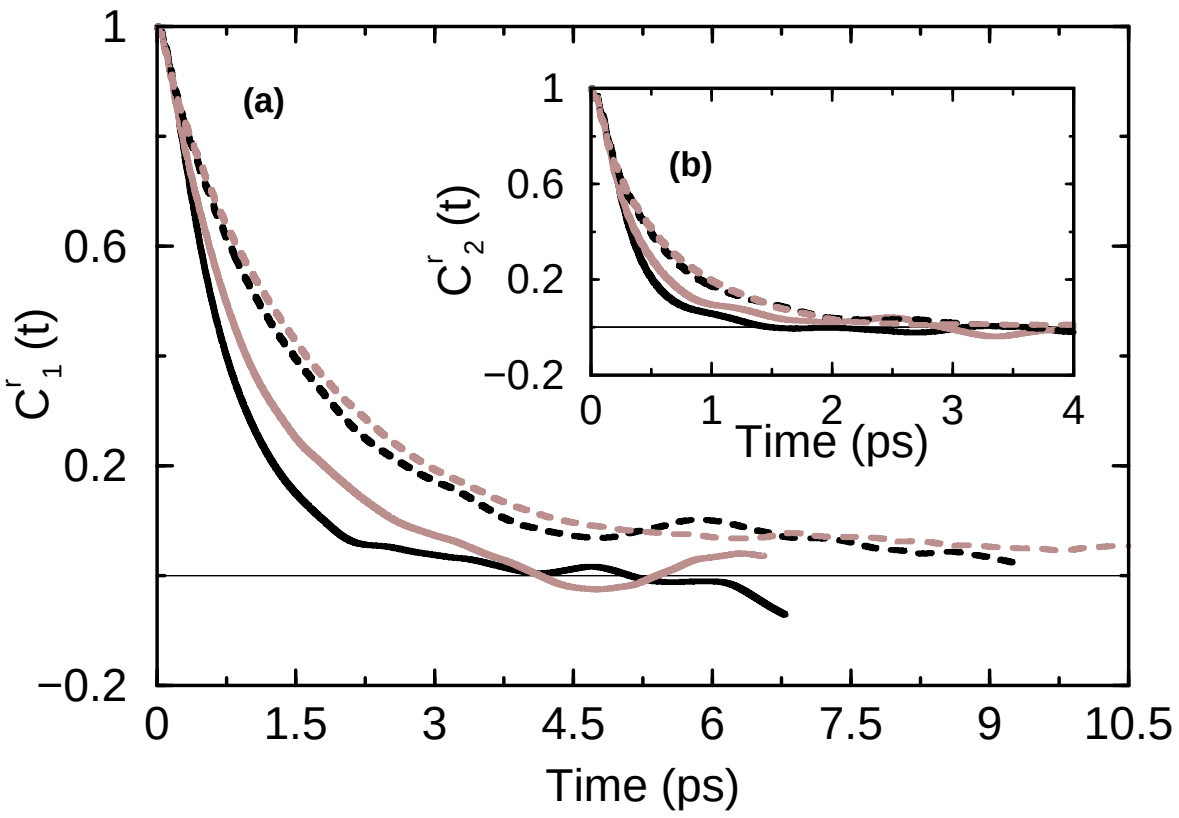

Figure 3.9: **Reorientational time correlation functions of CO_2 backbone at the following values of density: 0.80444 (solid black line), 1.1 (solid gray line), 1.216 (dashed black line), and 1.4 g/cc (dashed gray line). (a) First order time correlation function (C^r_1), (b) Second order time correlation function (C^r_2).**

these densities are 0.816 and 1.06 ps respectively while the same at 0.7 g/cc had earlier been calculated to be 0.62 ps [8]. At higher densities, C^r_1(t) decays much slower. τ^r_2 has been calculated by integrating C^r_2(t) (Figure 3.9b). We compare τ^r_2 obtained from our simulations with experiment [28] in Figure 3.10.

One finds a remarkably good agreement between experiment and our *ab initio* simulations. Although the experimental data at 319K is available only up to a density around 0.957 g/cc, our simulation results appear to match well with its extrapolation. For densities higher than 0.8 g/cc, the rotational relaxation time increases steeply with increase in CO_2 density.

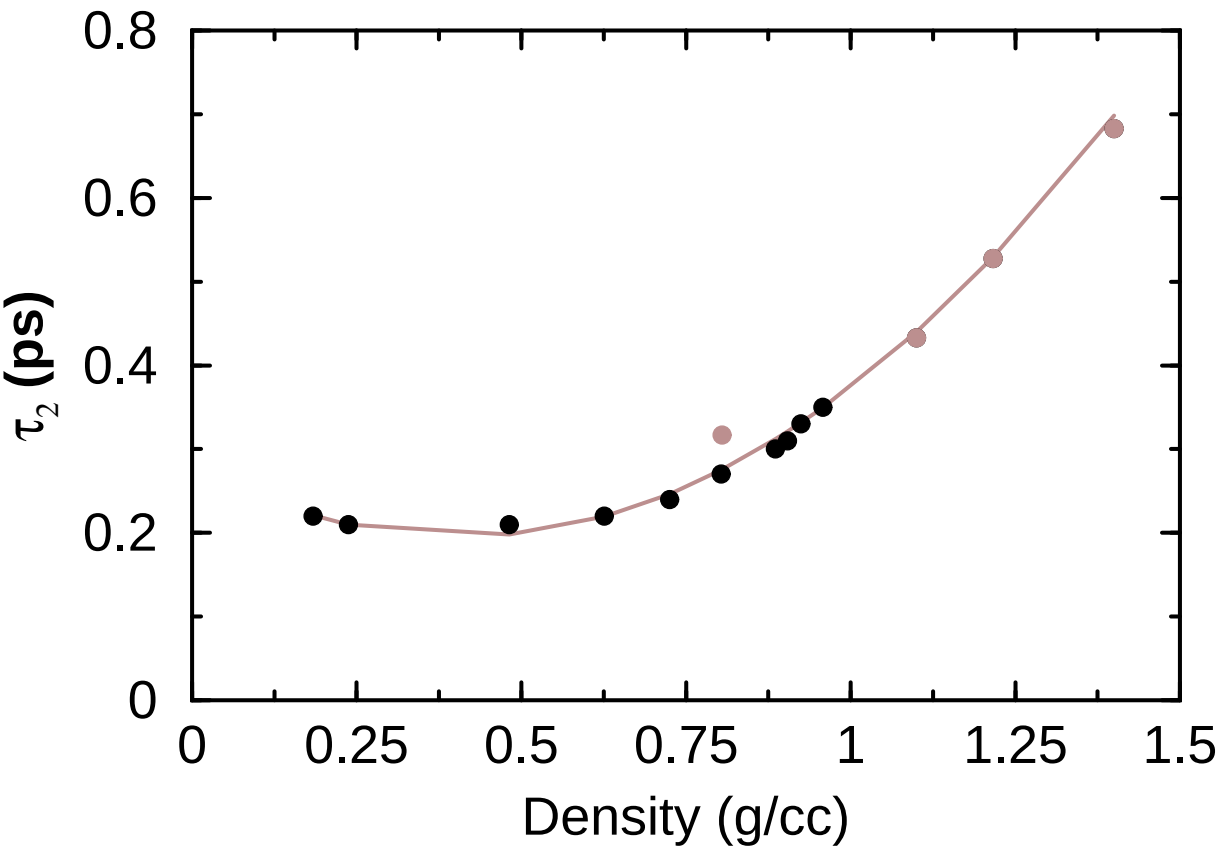

Figure 3.10: **Comparison of the relaxation times τ_2^r between experiment (dark circles) [28] and that obtained from our simulations (gray circles), as a function of density of scCO$_2$.**

Vibrational density of states

The density dependence of infrared [31, 32] and Raman [33] spectra of supercritical carbon dioxide have been studied extensively by several experiments. We report here the vibrational density of states that depict both intra- and intermolecular modes in scCO$_2$. The power spectrum at each density has been obtained as a Fourier transform of the velocity auto time correlation function of the atoms. The resolution in wavenumber is around 5 cm^{-1} at 0.80444 and 1.1 g/cc and around 3 cm^{-1} at 1.216 and 1.4 g/cc.

In the range of pressures examined here at 318.15K, no significant effect of pressure was observed on the frequencies of the fundamental modes of CO$_2$. Figure 3.11 shows

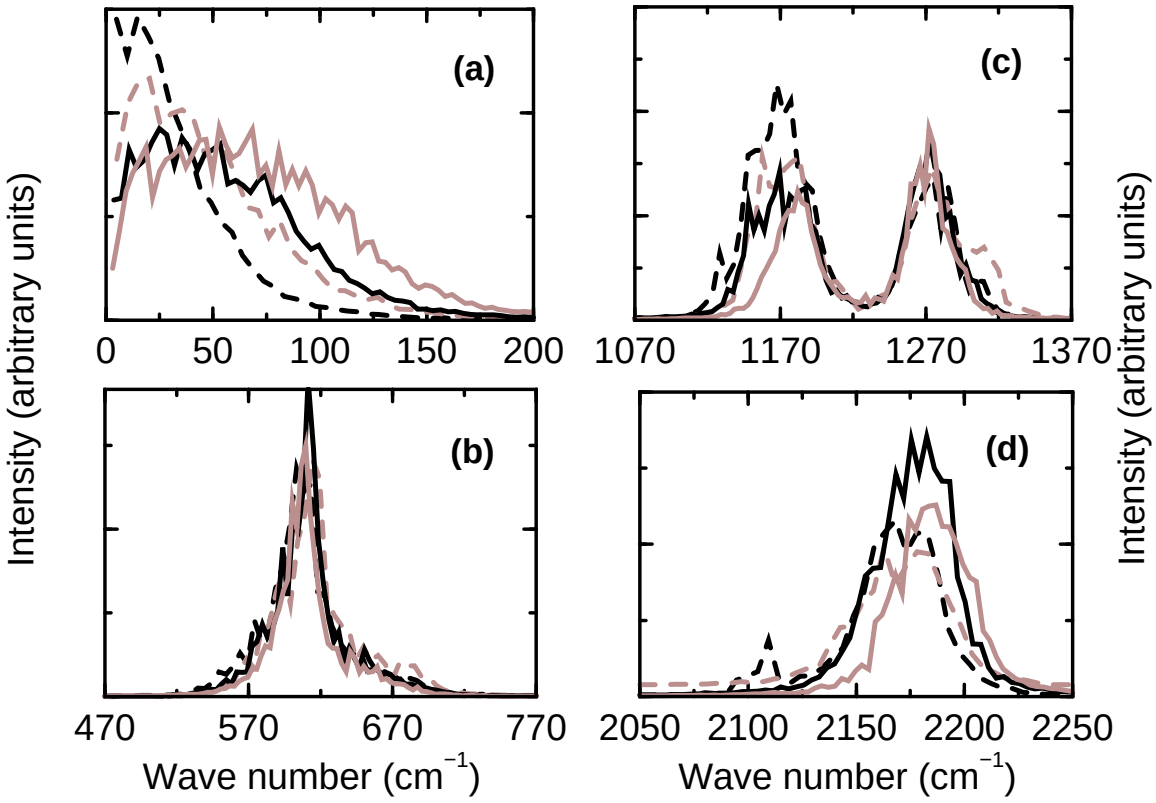

Figure 3.11: **Vibrational density of states of supercritical CO_2 obtained from the Fourier transformation of velocity auto-correlation functions of all the atoms at the following densities: 0.80444 (dashed black line), 1.1 (dashed gray line), 1.216 (solid black line), and 1.4 (solid gray line) g/cc. (a) Cage rattling, (b) Bending, (c) Symmetric stretching, and (d) Asymmetric stretching mode.**

the vibrational density of states of CO_2 at different state points. We do not observe any noticeable change in the peak positions of bending (ν_2) (Figure 3.11b), symmetric stretching (ν_1) (Figure 3.11c), and asymmetric stretching (ν_3) (Figure 3.11d) modes except for a relative contraction of the band width with increase in system pressure. These bands have been discussed in detail in our earlier work [8].

Crucial changes in the vibrational spectra of $scCO_2$ with pressure are observed in the external or intermolecular modes. Figure 3.11a shows the power spectra in the far-infrared region, between 0-200 cm^{-1}. With increasing density, we observe the emergence of a mode whose frequency shifts from around 15 cm^{-1} at 1.1 g/cc to 50 cm^{-1} at 1.4 g/cc. The blue shift is discernible with increasing pressure. This mode is likely due to the rattling of

molecules within cages formed by their neighbors. Cardini *et al* [34] had observed this broad mode in liquid-like clusters of CO_2 modeled using an empirical potential. Our results agree quantitatively with the frequency range in which they observed this mode. The non-zero value of the power spectrum at zero frequency is due to molecular diffusion. Note the decrease in its magnitude with increasing density, as expected.

3.4 Discussion and Conclusions

We have presented the results of *ab initio* molecular dynamics simulations of supercritical CO_2 performed under high pressures at T = 318.15K. As stated in the section on simulation details, the pressures reported here are experimental data [17] which correspond to the state conditions of our simulations. The main aim of this work was to elucidate the effect of pressure on the structural and dynamical properties of this solvent. Analysis of the local environment of a CO_2 molecule shows: (i) the progressive reorganization of first coordination shell with increasing pressure, (ii) that the distorted T-shaped arrangement of the closest neighbors around a central molecule changes gradually to a 'slipped parallel' like arrangement at farther distances. The distributions of the instantaneous O-C-O intramolecular angle shows a marginal preference towards linear geometry with increasing pressure. At higher densities, an increase in the coordination number can cause the polarization of a central molecule to cancel out which may explain this observation. In an interesting report, Ladanyi and Parson [35] had studied the polarization of iodide ions embedded in a CO_2 cluster. They observed a strong polarization of the solute when the bending force constant of CO_2 was reduced, i.e., in a hyperflexible model. Our *ab initio* results on the pressure dependence of the induced polarization in CO_2 molecules is thus relevant. The emergence of a pre-peak in the $g_{CO}(r)$ at a distance of around 3.1Å at high densities is an important finding from our study. We have rationalized its presence by a detailed comparison with the intermolecular structure in crystalline CO_2. This comparison also enabled us to understand the orientational preference exhibited by intermolecular

oxygen atom neighbors.

As regards the dynamics of the system, rotational relaxation times have been calculated from our simulations and an excellent agreement with experiment has been observed. As expected, the relaxation time τ_2^r derived from the second order reorientational correlation function increases with pressure. The vibrational density of states calculated from the simulations demonstrate negligible changes in the peak frequency of intramolecular modes. Interestingly, a blue shift in the low frequency intermolecular mode which occurs due to cage rattling, is observed, consistent with earlier MD calculations on CO_2 clusters [34]. At the highest density studied here, i.e., 1.4 g/cc, this mode is observed at 52cm^{-1}.

The current work offers microscopic details on the intra- and intermolecular structure and dynamics of scCO_2 with pressure. It would now be interesting to study the pressure dependence of solvent organization around solutes [36]. This issue and its relevance to the calculation of chemical reaction rates in this solvent are likely to be topics of our future investigations.

Bibliography

[1] T. Clifford *Fundamentals of Supercritical Fluids*, Oxford University Press, 1999.

[2] A. Hourri, J. M. St-Arnaud, T. K. Bose *Rev. Sci. Instr.* **69**, 2732-2737 (1998).

[3] R. Car, M. Parrinello *Phys. Rev. Lett.* **55**, 2471-2474 (1985).

[4] M. E. Tuckerman *J. Phys. Cond. Matt.* **14**, R1297-R1355 (2002).

[5] S. Chiappini, M. Nardone, F. P. Ricci, M. C. Bellissent-Funel *Mol. Phys.* **89**, 975-987 (1996).

[6] P. Cipriani, M. Nardone, F. P. Ricci *Physica B* **241-243**, 940-946 (1998).

[7] R. Ishii, S. Okazaki, I. Okada, M. Furusaka, N. Watanabe, M. Misawa, T. Fukunaga *J. Chem. Phys.* **105**, 7011-7021 (1996).

[8] M. Saharay, S. Balasubramanian *J. Chem. Phys.* **120**, 9694-9702 (2004).

[9] M. Saharay, S. Balasubramanian, *ChemPhysChem* **5**, 1442-1445 (2004); *ibid* **7**, 1167 (Erratum) (2006).

[10] I. I. Fedchenia, J. Schröder *J. Chem. Phys.* **106**, 7749-7755 (1997).

[11] Y. Zhang, J. Yang, Y. X. Yu, *J. Phys. Chem. B* **109**, 13375-13382 (2005).

[12] Z. Zhang, Z. Duan, *J. Chem. Phys.* **122**, 214507 (2005).

[13] E. Knozinger, P. Beichert *J. Phys. Chem.* **99**, 4906-4911 (1995).

[14] P. Raveendran, S. Wallen *J. Am. Chem. Soc.* **124**, 12590-12599 (2002).

[15] P. Cipriani, M. Nardone, F. P. Ricci, M. A. Ricci *Mol. Phys.* **99**, 301-308 (2001).

[16] J. Hutter, P. Ballone, M. Bernasconi, P. Focher, E. Fois, S. Goedecker, D. Marx, M. Parrinello, M. E. Tuckerman, CPMD Version 3.9.1, Max Planck Institut fuer Festkoerperforschung, Stuttgart, and IBM Zurich Research Laboratory, 1997-2001.

[17] Thermophysical properties of fluid systems, http://webbook.nist.gov/chemistry/fluid.

[18] M. Saharay, S. Balasubramanian *J. Phys. Chem. B* **110**, 3782-3790 (2006).

[19] J. G. Harris, K. H. Yung *J. Phys. Chem.* **99**, 12021-12024 (1995).

[20] A. D. Becke *Phys. Rev. A* **38**, 3098-3100 (1988).

[21] C. Lee, W. Yang, R. G. Parr *Phys. Rev. B* **37**, 785-789 (1988).

[22] N. Troullier, J. L. Martins *Phys. Rev. B* **43**, 1993-2006 (1991).

[23] F. Tassone, G. L. Chiarotti, R. Rousseau, S. Scandolo, E. Tosatti *ChemPhysChem* **6**, 1752-1756 (2005).

[24] G. J. Martyna, M. L. Klein, M. Tuckerman *J. Chem. Phys.* **97**, 2635-2643 (1992).

[25] M. Suzuki, O. Schnepp *J. Chem. Phys.* **55**, 5349-5356 (1971).

[26] B. Olinger *J. Chem. Phys.* **77**, 6255-6258 (1982).

[27] T. Umecky, M. Kanakubo, Y. Ikushima *J. Phys. Chem. B* **107**, 12003-12008 (2003).

[28] M. Holz, R. Haselmeier, A. J. Dyson, H. Huber *Phys. Chem. Chem. Phys.* **2**, 1717-1720 (2000).

[29] A. S. Haghighi, J. E. Adams *J. Phys. Chem. A* **105**, 2680-2686 (2001).

[30] J. E. Adams, A. S. Haghighi *J. Phys. Chem. B* **106**, 7973-7980 (2002).

[31] Y. Yagi, H. Tsugane, H. Inomata, S. Saito *J. Super. Crit. Fluids* **6**, 139-142 (1993).

[32] C. Yokoyama, Y. Kanno, M. Takahashi, K. Ohtake, S. Takahashi *Rev. Sci. Instrum.* **64**, 1369-1370 (1993).

[33] M. Poliakoff, S. M. Howdle, S. G. Kazarian *Angew. Chem. Ed. Engl.* **34**, 1275-1295 (1995).

[34] G. Cardini, V. Schettino, M. L. Klein *J. Chem. Phys.* **90**, 4441-4449 (1989).

[35] B. M. Ladanyi, R. Parson *J. Chem. Phys.* **107**, 9326-9338 (1997).

[36] M. Kanakubo, T. Aizawa, T. Kawakami, O. Sato, Y. Ikushima, K. Hatakeda, N. Saito *J. Phys. Chem. B* **104**, 2749-2758 (2000).

Chapter 4

Electron Donor-Acceptor Interactions in Ethanol-CO_2 Mixtures: An *Ab Initio* Molecular Dynamics Study of Supercritical Carbon dioxide

4.1 Introduction

Although $scCO_2$ is being used widely as a solvent for non-polar solutes such as fluorocarbons, its ability to solvate polar solutes is limited. Despite the reported enhancement of induced molecular multipole moments in the supercritical phase [1], $scCO_2$ is less capable to dissolve polar solutes. This disadvantage can however be circumvented by using other polar compounds as cosolvents [2–7]. The most commonly used cosolvents are short chain alcohols [8–11], and water [12, 13]. The addition of small amounts of cosolvents such as methanol or ethanol in $scCO_2$ can enhance the solubility of moderately polar

compounds [14] and solid solutes [15]. This experimental observation has not yet been explored from a microscopic perspective. In this work, we attempt to study such a solvent mixture and provide molecular level details on the interactions between the solvent species.

The carbon atom in a CO_2 molecule is electron deficient, while the oxygen has two lone pairs of electrons. Thus depending on its environment, CO_2 can act either as a Lewis acid or base [16,17], conditions which can induce a dipole moment in CO_2 [1,18]. In the former situation, the carbon atom behaves as an electron acceptor (partial charge transfer) from another molecule in the vicinity while in the latter, the oxygen atom acts as an electron donor. The miscibility of cosolvents such as alcohols in CO_2 is closely linked to this aspect of the carbon dioxide molecule. The earliest quantitative data on the association between an alcohol and carbon dioxide was established by King and coworkers [19, 20], who determined large negative values for the cross second virial coefficient. However, alcohols are also known to aggregate in $scCO_2$ due to the stronger alcohol-alcohol [21] hydrogen bonding that can prevail over the weak association between alcohol and the solvent [22, 23]. In a pioneering study, Smith and coworkers [24, 25] carried out infrared spectroscopic measurements identifying such hydrogen bonds through a red shift in the stretching frequency (ν_1) of the functional group relative to that in gas phase. On the other hand, static dielectric constant data [26] suggests favourable interaction between ethanol and CO_2 under supercritical conditions. The variation in the dielectric constant upon mixing is found to be lesser than what is expected from an ideal, linear dependence on the mole fraction of ethanol. This can be understood as due to the disruption of the orientations of the linear ethanol molecules present in the electric field by CO_2 molecules. More recently, the interaction between ethanol and CO_2 in $scCO_2$ has been studied using vibrational spectroscopy that probe the O-D stretching in the alcohol as well as by *ab initio* calculations in the gas phase by Besnard and coworkers [27, 28]. Han and co-workers [29] have studied the phase diagram of ethanol-CO_2 and CO_2-*n*-pentane mixtures. They have

found that as the solvent pressure tends towards criticality, the local density of solvent molecules reduces whereas the specific heat at constant volume increases.

There is astrophysical interest as well in the interaction between carbon dioxide and alcohols. Recent experiments carried out by the infrared space observatory have identified large amounts of CO_2 ice and methanol in protostellar environments [30–33]. The observed spectra have been interpreted based on vibrational spectroscopic experiments carried out on mixtures of methanol and CO_2 in the laboratory under different thermal conditions. These experiments were augmented by quantum chemical calculations on isolated complexes of the two molecules. The results show that while the bending mode of an isolated CO_2 molecule is doubly degenerate, it is split into two peaks in the complex. The lifting of the degeneracy in the associated complex is a consequence of CO_2 becoming non-linear. The interaction is surmised to be of Lewis acid-base type wherein the electrons belonging to the interacting lone pair of the ethanol oxygen repel the oxygen atoms of the CO_2, causing it to bend. The intramolecular O-C-O angles have been calculated to be around 177^o [33]. These results confirm the original gas phase calculations of Jamroz *et al* [34] on EDA complexes of CO_2.

Numerous computer simulation studies have been carried out to understand the properties of pristine $scCO_2$ as well as mixtures of CO_2 with other cosolvents/solutes. Most of these studies are simulations that employ an empirical potential [35,36] looking at various bulk properties of the solvent as well as its miscibility with solutes [37,38]. Recently, Stubbs and Siepmann have performed Monte Carlo calculations [38] of methanol-CO_2 mixtures with empirical potentials, in order to examine its phase behavior and to study the formation of methanol aggregates in $scCO_2$. They observed the formation of hydrogen bonds between methanol molecules and more importantly, the formation of a hydrogen bond between the hydroxyl hydrogen and the carbonyl oxygen. Configurations indicating the presence of EDA interactions between the carbonyl carbon and the alcohol oxygen were not reported. Earlier, we have studied pure $scCO_2$ at 140 bar and 318.15K using the Car-

Parrinello molecular dynamics (CPMD) method [1, 39]. Our calculations examined the evolution of the intramolecular bond angle in CO_2 and its deviation from linearity due to (i) thermal fluctuations and (ii) charge polarization from near neighbor interactions. The polar attributes of carbon dioxide molecules in its interaction with other molecules have attracted much attention recently [4]. The *ab initio* MD (AIMD) work on $scCO_2$ [1, 39] has spurred researchers to find better interaction models for carbon dioxide [40], a salient feature of which is the requirement of a flexible CO_2 in order to reproduce the experimental values of the dielectric constant as a function of pressure. It is thus crucial that such AIMD calculations, that inherently include flexibility and polarizability are performed for cosolvent mixtures as well.

In this article, we study a mixture of carbon dioxide and ethanol under supercritical conditions. Our *ab initio* MD calculations employ only one ethanol molecule in a bath of 64 carbon dioxide molecules. Thus, our simulations cannot be used to study the phenomenon of alcohol aggregation in $scCO_2$, by construction. AIMD calculations of alcohol aggregates present in solvent would require very large system sizes and are beyond the scope of the current work. Thus, we limit this study to the investigation of microscopic interactions between alcohol and carbon dioxide molecules in $scCO_2$. Hence despite its widespread use as a cosolvent in $scCO_2$, we call ethanol as a "solute" within this paper. Calculations with larger mole fractions which include the effects of aggregation are planned to be performed in future. The AIMD trajectory provides us data on the structure around the ethanol, the dynamics of the molecules, and solute-solvent interactions. Inherently devoid of adjustable parameters, these calculations enable us to obtain an insight into the microscopic organization of carbon dioxide molecules around ethanol. Anticipating our results, we find strong evidence, both in terms of structure and as well as in dynamics for Lewis acid-base type of interaction between CO_2 and ethanol in this bulk mixture. We follow this Introduction by providing details of the simulation and discuss the results of our analyses.

4.2 Simulation Details

Car-Parrinello MD simulations [41] were performed using the CPMD program [42], while the classical MD calculations were carried out using the PINY_MD code [43]. The system consisted of one ethanol molecule soaked in a bath of 64 carbon dioxide molecules at a temperature of 318.15K and a density of 0.699 g/cc (system A). This thermodynamic condition is well above the critical point of carbon dioxide and that of the mixture as well. The mole fraction of ethanol in the solution is 0.0154. CPMD calculations were carried out within the density functional approximation. The exchange and correlation functionals were from the works of Becke [44], and Lee, Yang, and Parr [45] respectively, and thus fall into the category of generalized gradient approximated (GGA) functionals. Such functionals have been used in *ab initio* MD studies of proton transport in methanol earlier [46]. The electronic orbitals of valence electrons were expanded in a plane wave basis set with an energy cutoff of 70Ry for the orbitals. Norm conserving pseudopotentials of the Troullier-Martins form [47] were employed for the treatment of the core electrons. In order to elucidate the influence of the ethanol molecule on the solvent structure, and to compare the structure of pure $scCO_2$ obtained using the BLYP functionals against our earlier LDA calculations, we have also carried out a bulk CPMD simulation of pure $scCO_2$ (32 CO_2 molecules, system B) at the same state point using the same procedures as described above, for a total run length of 10ps with 2.9 ps for equilibration.

Two types of interactions are possible between ethanol and CO_2:

i. Hydrogen bonding between the hydroxyl hydrogen of ethanol and the oxygen of CO_2

ii. Lewis acid-Lewis base (LA-LB) interaction between the oxygen of ethanol and the carbon of CO_2.

These were investigated using gas phase calculations on isolated dimers of CO_2 and a ethanol-CO_2 complex. Different initial configurations that varied in the locations of CO_2 with respect to ethanol were investigated. Calculations on the optimization of geometry of CO_2 clusters as well as the energy of dimerization using the functionals described above

yielded results that are in good agreement with results reported in the literature using other methods. These are summarized and compared with data obtained from quantum chemical calculations in Table 4.1. The latter were carried out using the Gaussian [48]

Species	Angle	Method	Bond length (Å)	Dimerization energy (kcal/mol)
CO_2 Monomer	180.0 (O=C=O)	CPMD	1.176	-
	180.0 (O=C=O)	Gaussian98	1.169	-
CO_2 Dimer (slipped parallel)	78.9 (O_1-C_2-O_2) 100.9 (C_2-O_2-C_1)	CPMD	∼1.176	-0.170
	84.1 (O_1-C_2-O_2) 138.5 (C_2-O_2-C_1)	Gaussian98 Ref. 29	-	-
	-	Gaussian98 Ref. 12	-	-0.290
ethanol-CO_2 EDA complex	123.1(θ_1) 128.5(θ_2)	CPMD	2.833 (O_e-C_C)	-2.627
	120.9(θ_1) 129.7(θ_2)	Gaussian98	2.746 (O_e-C_C)	-2.720
	114.7(θ_1)	Gaussian98 Ref. 23	2.754 (O_e-C_C)	-2.417
ethanol-CO_2 h-bonded complex	179.4 (O=C=O)	CPMD	2.212 (O_C-H_e)	-0.840

Table 4.1: Geometry and energetics of optimized clusters. The subscripts '1' and '2' in the angle representation of CO_2 dimer represent molecular indices.

suite of programs with 6-31++g* basis set and electron correlations have been included according to density functional theory using Becke's three-parameter hybrid formalism [49] and Lee-Yang-Parr functionals [45] (B3LYP). These calculations show that the complex with Lewis acid-base interaction between ethanol and CO_2 is energetically more favourable than the one with hydrogen bonded interaction between them. In order to aid further discussion, we provide in Figure 4.1, a schematic of atom nomenclature and parameters

which are used to characterize the geometry of the EDA complex. For the study of vibrational spectra of such clusters, CPMD trajectories of these systems present in a cubic box of edge length 13Å were generated, in the absence of periodic boundaries.

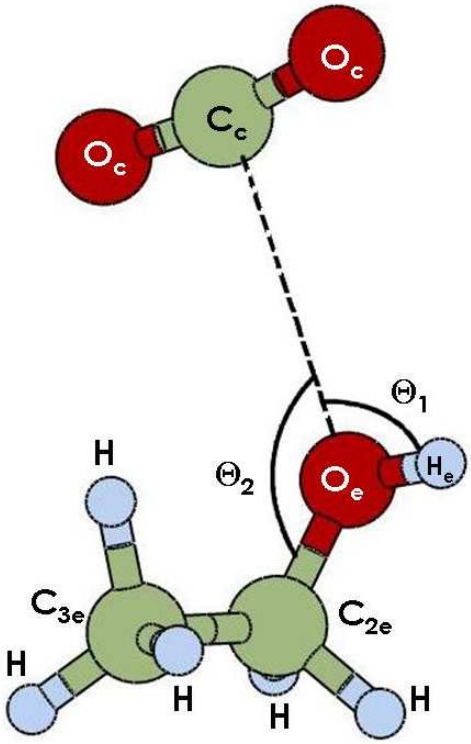

Figure 4.1: **The nomenclature of atoms and angles for a typical EDA geometry of a ethanol-CO_2 complex.**

The 1:64 ethanol-CO_2 bulk system was equilibrated for around 40ps using classical CHARMM all-atom potential model for ethanol [50] and the EPM2 model for CO_2 molecules [51]. Lorentz-Berthelot combination rules were employed for the cross interactions. The CPMD calculations were performed starting from the final configuration obtained from this classical MD simulation. All the hydrogen atoms in ethanol were replaced by deuterium in order to be able to use a larger time step in CPMD calculations. The electronic wavefunctions were initially quenched to the Born-Oppenheimer surface. The fictitious dynamics of the electronic degrees of freedom was carried out with an electron mass of 500 a.u. which maintained the electrons at that surface. The equations of motion were integrated with a conservative time step of 4 a.u. (around 0.096fs). Three di-

mensional periodic boundary conditions consistent with a simple cubic box of edge length 18.843Å were employed. In all, the system consisted of 201 atoms and 1044 valence electrons. Although the system contained only 64 CO_2 molecules, the box size is quite large when compared to a system of 64 molecules of say, liquid water under ambient conditions (a well studied case). The latter requires a cubic box of edge length of only 12.4Å, and possesses only 512 valence electrons. Thus, in comparison to a CPMD calculation of liquid water at the same system size, the current calculations are far more computationally demanding. Temperature control was achieved by the use of two Nosé-Hoover chain thermostats [52], one for the ions and another for the electrons. The target kinetic energy for the electrons was set to 0.04 a.u., a value determined from preliminary NVE runs. The total run length was around 9.5 ps that included a 1.85 ps trajectory devoted for equilibration. As the system is in the supercritical phase, the diffusion coefficients of molecules are rather large [39], and hence these run lengths are large enough to obtain meaningful properties. The fluctuation in the total energy was around one part in 10^5.

Classical molecular dynamics simulations of this binary mixture at the same state point and composition as in the CPMD run were performed using the TraPPE-UA potential [53] for the sake of comparison. The TraPPE-UA potential is an united atom model for ethanol, in which the CH_3 and CH_2 groups are replaced by pseudoatoms. In these runs, the system was equilibrated for 240ps followed by a productive run of 360ps during which the coordinates were stored at a regular interval of 40 fs. The non-bonded interactions were truncated at 9.25 Å. Note that the TraPPE-UA potential model prescribes an interaction cutoff of 14Å, which could not be accommodated in the 1:64 classical MD run due to the smaller box size. In order to check if the decreased interaction cutoff leads to any changes in the intermolecular structure, we performed MD simulations of a large system, that of 1 ethanol molecule soaked in a bath of 240 CO_2 molecules. For these latter simulations, an interaction cutoff of 14Å was employed. The radial distribution functions obtained for the smaller system were compared to those obtained from the 1:240 system. The only

marked difference was that the first hump (which signifies hydrogen bonding) as well as the first peak in the g(r) of the ethanol hydrogen to carbon dioxide's carbon was found to be marginally smaller in the larger system. Radial distribution functions (RDF) were calculated using a bin width of 0.2Å.

In a seminal work, Stubbs and Siepmann [54] have provided a microscopic interpretation of the vibrational spectra of alcohol aggregates in a hydrocarbon solvent, using *ab initio* MD methods. We draw inspiration from their work in the analyses of vibrational spectra of the bulk ethanol-CO_2 mixture. The vibrational density of states (VDOS) of CO_2 and ethanol were determined using regularized resolvent transformation (RRT) [54,55] of the velocity autocorrelation function of atoms. The RRT method enables one to obtain the spectrum at a higher resolution than a discrete Fourier transform. All spectra derived by RRT were compared against those obtained from a discrete Fourier transform to guard against numerical artifacts. Features in the VDOS spectra of the bulk 1:64 mixture have been interpreted by examining the VDOS of three clusters: (i) CO_2 monomer at 10K, (ii) CO_2 dimer [17,56] in slipped parallel geometry at 10K, (iii) CO_2 and ethanol forming an EDA complex maintained at a temperature of 10K. Each of these systems was studied by generating CPMD trajectories of duration around 8 ps.

4.3 Results and Discussion

4.3.1 Structure

Isolated Molecules and Complexes

The carbon atom in a CO_2 molecule can act as Lewis acid and can accept partial electronic charge. This charge could come from another molecule possessing a lone pair on any one of its atoms so that the pair of molecules could form a weak EDA complex. In the present study, we deal with the ethanol-CO_2 system where CO_2 can be treated as a Lewis acid (while forming an EDA complex with ethanol) as well as a Lewis base while forming a

hydrogen bonded complex with ethanol. Even in the absence of a solute, such LA-LB interactions are possible between CO_2 molecules themselves. The optimized configurations of isolated ethanol-CO_2 complexes obtained from CPMD are exhibited in Figure 4.2.

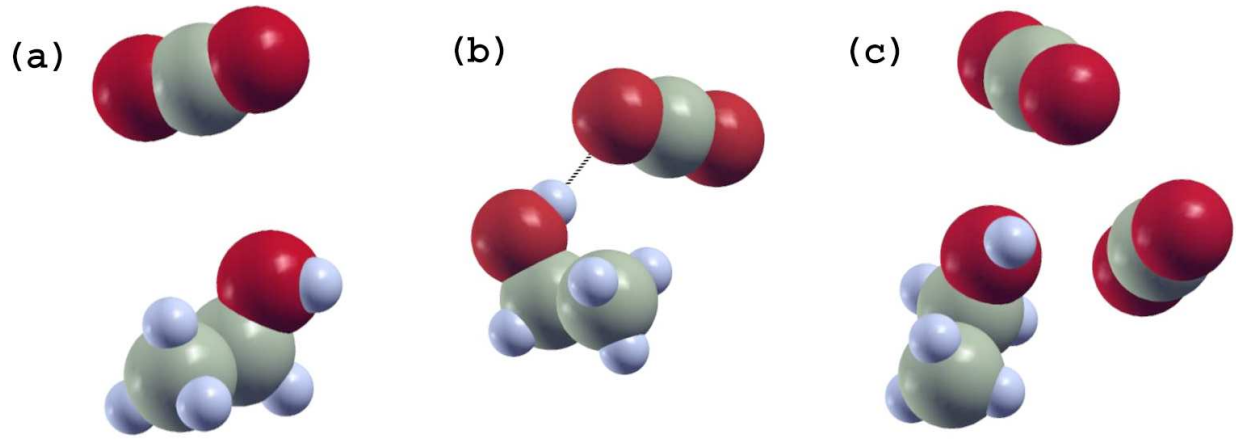

Figure 4.2: **Snapshots of cluster configurations. (a) ethanol-CO_2 EDA complex obtained by geometry optimization within CPMD. (b) ethanol-CO_2 hydrogen bonded configuration obtained from geometry optimization within CPMD. (c) An EDA complex containing two CO_2 and one ethanol molecule, obtained as a snapshot from the CPMD trajectory of the bulk ethanol-CO_2 mixture. Oxygen atoms are shown in black, carbon atoms are in white, and hydrogen atoms are in gray.**

In Table 4.1, we compare the geometry and energetics of these clusters with earlier investigations and that obtained from our Gaussian98 calculations. Although the binding energy and O_e-C_C distance for the EDA complex are in good agreement with the work of Tassaing *et al* [27], the angle θ_1 is slightly different. This difference may arise due to the different basis sets used for the optimization. It can be noticed that in the CPMD method, the EDA complex with ethanol is energetically more stable than the hydrogen bonded one. Note that the difference in the binding energies between the EDA and hydrogen bonded states are accessible to thermal fluctuations at and near ambient conditions. However rare, it is also possible for two carbon dioxide molecules to be simultaneously proximal to the ethanol oxygen in an EDA-like geometry, as oxygen possesses two lone pairs of electrons. A snapshot of an occurrence of such a kind observed in the bulk ethanol-CO_2 system is shown in Figure 4.2c. We isolated such a complex of one ethanol molecule associated

with two CO_2 molecules from the bulk system, and used it as a starting configuration for geometry optimization. This run did not converge, and we noticed large separations between the molecules of the complex at the end of the run. Hence it is possible that such a double EDA complex could be stabilized by entropic factors alone.

Bulk Calculations

3.1.2.1 Pair Correlation Functions

The purpose of this work is to provide a molecular level insight into the solvent structure around the solute. The radial distribution function is an important tool to investigate the arrangement of near neighbor molecules around a central one. Figure 4.3 compares the partial intermolecular RDFs between CO_2 molecules in the solution, obtained from both *ab initio* and classical MD calculations. All the RDF curves are observed to nearly reach their uncorrelated value of unity within half boxlength, which indicates that the system size studied here is probably large enough for a proper simulation of the fluid phase. The first minima of $g_{CC}(r)$ (Figure 4.3a) are observed at 6.15Å and 5.90Å for the CPMD and MD calculations, with corresponding coordination numbers of 9.5 and 8.4 respectively. Figure 4.3b shows the $g_{CO}(r)$. Here too we observe a higher population of oxygen atoms around carbon in CPMD than in MD simulations. In Figure 4.3c, we compare the CO pair correlation functions obtained from systems A and B. The two curves are nearly identical which indicates that the influence of ethanol on the solvent structure is negligible in its present concentration. It also indicates that a system size of 32 molecules is large enough to capture the crucial features of intermolecular structure in $scCO_2$, at this state point. The hump at 3.2Å that was observed in our earlier work on pure $scCO_2$ [39] is present only as a weak shoulder in the current ethanol-$scCO_2$ system. It thus appears that the LDA calculation generates a fluid that is more structured than the current simulations that employ the BLYP functionals. Results from the classical simulations using empirical potentials lie in between the data obtained from LDA and

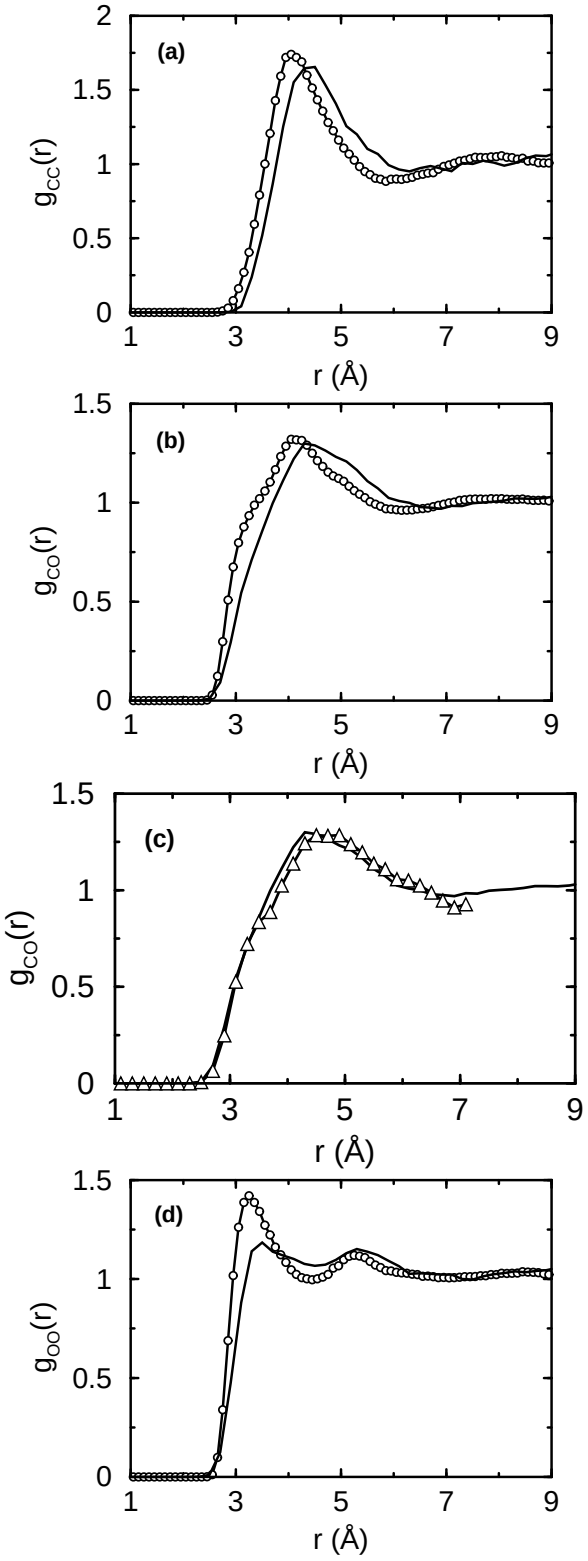

Figure 4.3: **CO_2-CO_2 intermolecular pair correlation functions obtained from the 1:64 system. Solid lines represent CPMD results, lines with open circles represent classical MD results, and line with open triangle in (c) represents result from system B.**

BLYP based simulations. Similar differences between LDA and GGA functionals have been well documented in the literature, specifically for the case of liquid water [57]. The same trend has been observed in $g_{OO}(r)$ (Figure 4.3d), where the first maxima is less peaked than in neat CO_2.

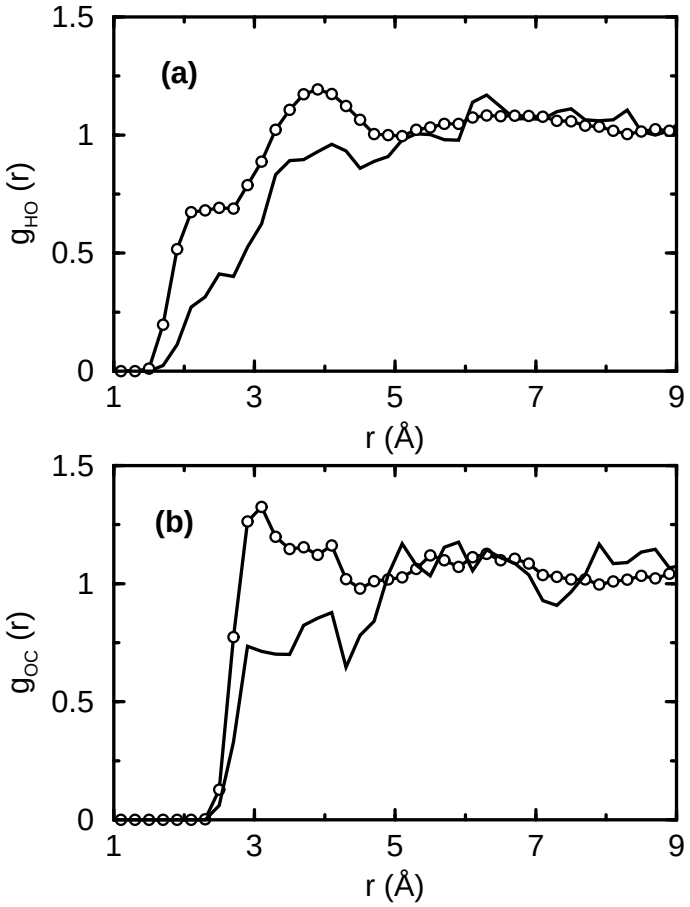

Figure 4.4: **Ethanol-CO_2 intermolecular pair correlation functions obtained from the 1:64 system. Solid lines represent CPMD results and lines with open circles represent classical MD results.**

The distribution of CO_2 molecules around a central ethanol molecule has been investigated by two partial radial distribution functions shown in Figure 4.4. The first hump at around 2.5Å in the RDF for CO_2's oxygen around a central hydroxyl hydrogen of ethanol obtained from both CPMD and classical MD data, indicates hydrogen bonded interaction between these two species (Figure 4.4a). The same has been observed in the Monte Carlo work of Stubbs and Siepmann [38] in the methanol-CO_2 system. However,

hydrogen bonding between the species is found to be much weaker in the corresponding CPMD results. The coordination number for the two g(r)s integrated up to the standard hydrogen bond length of 2.5Å is around 0.28 and 0.64 obtained from CPMD and MD calculations respectively. It may be pertinent to confirm the relative weakening of the hydrogen bonded configuration in CPMD by studies using other exchange-correlation functionals. If the current results are validated, the interaction potential for classical MD may have to be refined so as to reproduce the *ab initio* results. The radial distribution function of C_C with respect to O_e (Figure 4.4b) is peaked at around 4.1Å in CPMD and at 3Å in MD simulations. The first minimum of this g(r) is at 4.3Å. The coordination number upto the first minimum is around 2.0 and 3.0 from CPMD and classical MD simulations respectively. We choose this distance as the upper limit for C_C-O_e separation in the formation of EDA complexes in bulk.

3.1.2.2 Characterization of electron donor-acceptor and hydrogen bonded complexes

Probability density map : An idea of the geometry of the EDA complex can be obtained by studying the atomic probability density map (also called the spatial distribution function). Figure 4.5 shows the probability distribution for the location of carbonyl carbon (C_c) situated within 4.3Å of the oxygen(O_e) atom of ethanol, the data averaged over the full trajectory. The two shades represent different probabilities of finding C_c around the central O_e. The two distinct lobes of high probability point to the directional nature of the EDA interaction between the lone pair of ethanol's oxygen with CO_2's carbon. Note that the lobes appear to be along the direction of the central oxygen's lone pairs.

Hydrogen bonds are often identified in molecular simulations using a set of geometric criteria that limit the oxygen-oxygen distance to 3.5Å, the donor hydrogen-oxygen distance to 2.5Å, and the oxygen-oxygen-donor hydrogen angle to be greater than 140^o [38, 58]. Since the EDA interactions reported here are also quite directional just as hydrogen bonds are, we could develop a similar set of conditions. As mentioned earlier, we choose a

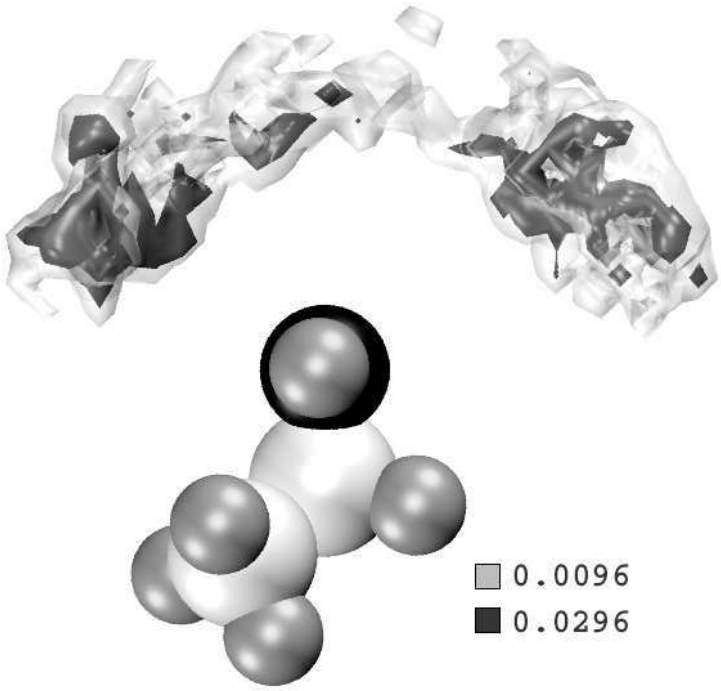

Figure 4.5: **Probability density map for the location of CO_2's carbon atom within a distance of 4.3Å from O_e, obtained from CPMD data of the bulk mixture. Gray and black regions represent low and high probability respectively. Oxygen atoms are shown in black, carbon atoms are in white, and hydrogen atoms are in gray. The OH vector of the hydroxyl group points along the normal to the paper. The density values are in units of $Å^{-3}$.**

4.3Å cutoff for the distance between ethanol oxygen and carbonyl carbon. This distance corresponds to the first minimum in the corresponding pair correlation function. In addition, two angle conditions need to be employed, as the EDA interaction is directional – a part of the lone pair electrons of the ethanol oxygen being donated to the acidic carbon of CO_2. In the following, we provide a rationale for the choice of these angle conditions, by studying their probability distributions.

The probability distribution of cosines of C_c-O_e-H_e (θ_1) and C_c-O_e-C_{2e} (θ_2) angles for carbon dioxide molecules that satisfy the C_c-O_e distance cut-off (of 4.3Å) are shown in Figure 4.6. The distribution for θ_1 exhibits a rather weak preference for the tetrahedral angle and that for θ_2 shows a peak at a cosine value of -0.33. Thus, carbon dioxide molecules are seen to have a preferred orientation with respect to the oxygen atom of the

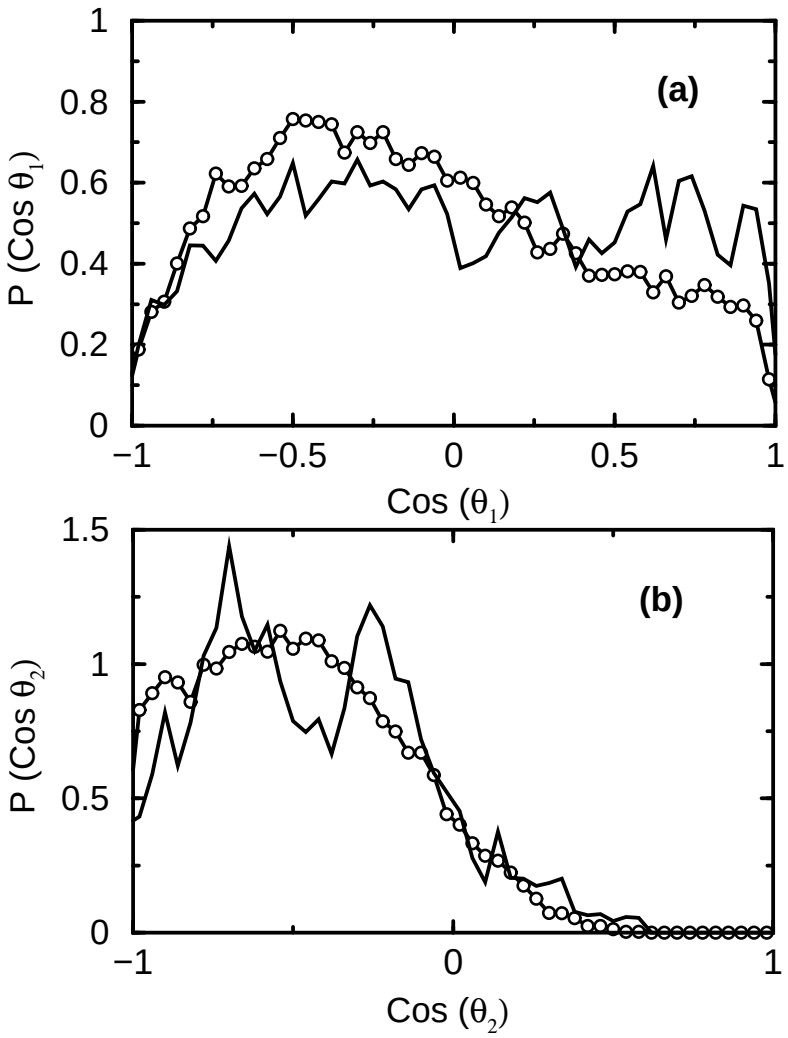

Figure 4.6: **Probability distributions for the angles θ_1 and θ_2 obtained for C_c-O_e pairs present within a distance of 4.3Å. Solid lines represent CPMD results and lines with open circles represent classical MD results.**

ethanol molecule, a consequence of the Lewis acid-base interaction between them.

In order to arrive at reasonable angular limits to define the EDA complex, we have analyzed the O_e-C_c pair correlation functions with different angular ranges of θ_1 and θ_2. We have obtained these functions for C_c atoms which fall within a given angular range in both θ_1 and θ_2, around the ethanol molecule. The volume element required for normalization of the function was estimated numerically by generating uniform random numbers which fall within the spherical shell of the required radius, a procedure akin to the numerical calculation of the value of π using an elementary Monte Carlo procedure [59]. Pair

correlation functions of those C_c atoms which do not satisfy the two angular conditions were also obtained for purposes of reference. These are compared in Figure 4.7 for three different angular limits placed on θ_1 and θ_2. Note the presence of sharp peaks in the

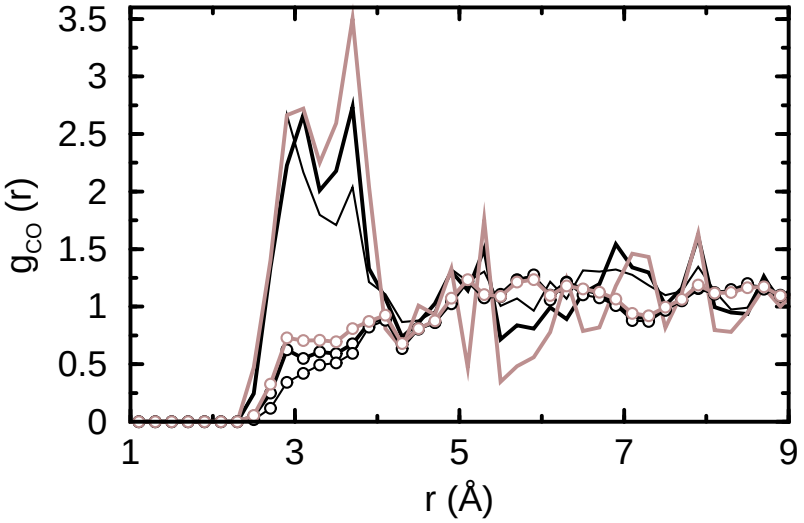

Figure 4.7: **Radial distribution functions of O_e-C_c pair obtained from the CPMD calculation. Solid lines represent $g_{CO}(r)$ within the angular range defining the EDA complex and lines with open circles represent outside the angular range. $90^O \leq \theta_1, \theta_2 \leq 130^O$ (thick black), $80^O \leq \theta_1, \theta_2 \leq 140^O$ (thin black), $100^O \leq \theta_1, \theta_2 \leq 120^O$ (gray).**

functions that satisfy the angular conditions relative to the ones that do not satisfy them. This behavior shows the presence of a preferred window of angle in the formation of the EDA complex. The intensity of the first peak in the g(r) that satisfies the angular condition, upon increasing the angular limits, is gradual and not dramatic. This implies that the EDA interaction is only weakly angle dependent (in these ranges of angles). In the following discussion, we choose the range of θ_1 and θ_2 angles for the existence of a LA-LB complex to be between 90^o and 130^o. The results to be discussed on the concentration of EDA complex in bulk and its properties do depend on this choice. We have provided results on sensible alternate choices of these angular limits as well, in order to provide a perspective.

Armed with this set of criteria for defining the EDA complex (and a similar well established one to define the hydrogen bond), we proceed to calculate the ratio of occurrence of

these types of configurations in the ethanol-CO_2 mixture. Within our trajectory of length 7.7 ps, the signatures of the EDA complex were observed in several segments together spanning a length of 3.0ps, while the hydrogen bonded configuration was observed for a total duration of around 0.6ps. In the remaining duration of the trajectory, the ethanol molecule did not satisfy either the EDA criteria or the hydrogen bond criteria. The EDA interaction is thus favored even in the bulk phase at finite temperature, consistent with our observations on the energetics of these complexes in the gas phase. We can assume that these two states exist in a dynamical equilibrium along with another state in which the ethanol and the carbon dioxide are not associated either through a hydrogen bond or through a EDA type arrangement. In the rest of the discussion, we ignore the "dis-associated" state. The equilibrium constant, K between the EDA arrangement and the hydrogen bonded complex is equal to the ratio of their concentrations, and thus of the ratio of the durations that they were observed for. K is related to the free energy difference between these two states, ΔA as,

$$\Delta A = -RTlnK \tag{4.1}$$

where R is the universal gas constant. ΔA is determined to be -0.88 kcal/mol, for the choice of angular domain of 40^o (with limits on θ_1 and θ_2 being 90^o and 130^o). This free energy difference changes to -0.24 kcal/mol and -1.36 kcal/mol for the angle choices of 100^o-120^o and 80-140^o respectively. Note that the energy difference between the EDA and hydrogen bonded complex in gas phase is -1.79kcal/mol. Thus, irrespective of the choice of the angle limits, relative to the hydrogen bonded moiety, the EDA complex is more stable in gas phase than in the bulk system, as the free energy difference is found to be smaller than the energy difference between the gas phase (zero Kelvin) complexes.

Earlier investigations [33, 34] on the ethanol-CO_2 complex have shown that the CO_2 molecules prefer two possible orientations with respect to the ethanol: "parallel" (or horizontal) and "perpendicular" (or vertical) arrangements. In the "parallel" orientation,

the plane of CO_2 lies parallel to the H_e-O_e-C_{2e} plane of ethanol while it is perpendicular in the "perpendicular" orientation. Based on quantum chemical calculations of isolated EDA complexes, the "parallel" configuration has been reported to be more stable than the perpendicular one [33]. In Figure 4.8, we show the probability distribution of the

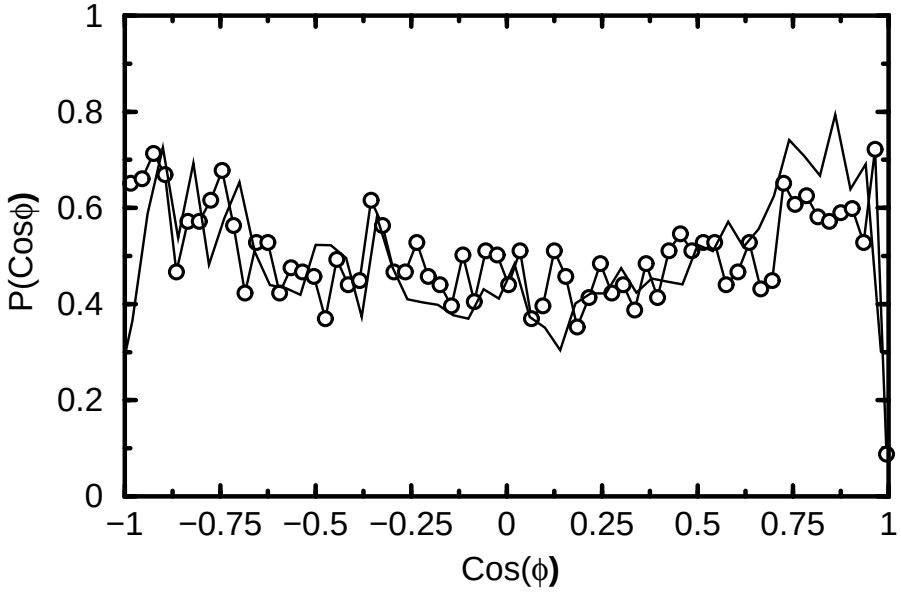

Figure 4.8: **Probability distribution of Cos(ϕ), where ϕ represents the angle between the instantaneous O_C-C_C-O_C and C_{2e}-O_e-H_e planes. Solid line represents CPMD results and line with open circles represents the classical MD result.**

cosine of the angle (ϕ) between the H_e-O_e-C_{2e} plane of ethanol and the plane of CO_2 during instances in the CPMD trajectory when the EDA complex is formed. Such distributions obtained from both CPMD and classical MD exhibit peaks at $\cos\phi = \pm 1$ which is consistent with the gas phase work of Dartois and coworkers [33].

Linearity of CO_2 : As discussed in the Introduction, interactions with ethanol can influence the carbon dioxide molecule to assume a non-linear geometry. Our earlier work [1,39] showed that instantaneous non-linear CO_2 configurations are possible at high enough pressures, due to interactions between CO_2 molecules themselves. This could be caused both by thermal fluctuations, as well as by instantaneous anisotropic distributions of neighbors in the first coordination shell. The latter would polarize the electron density of a central

CO_2 molecule leading to deviations from a linear geometry, as well as imparting a molecular dipole moment to the instantaneous configuration [1]. It would thus be interesting to investigate the geometry of the carbon dioxide molecule(s) which interact favorably with ethanol. We provide results on the intramolecular O_C-C_C-O_C angle of CO_2 in various contexts in Figure 4.9. The probability distribution for the instantaneous value of the

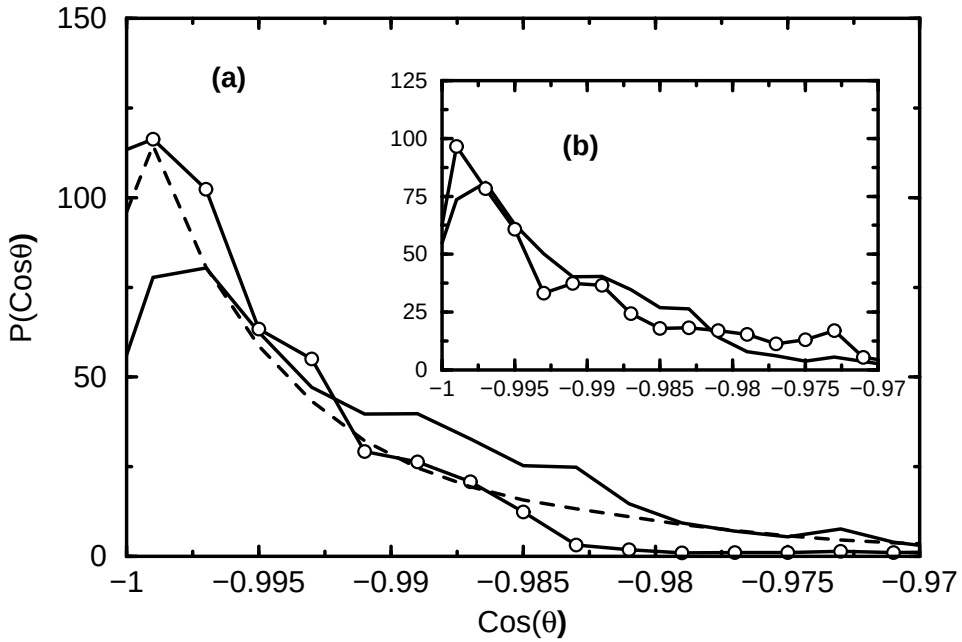

Figure 4.9: **Probability distribution for the intramolecular O_C-C_C-O_C angle of CO_2 molecules for 'free' CO_2 (dashed line), CO_2 while forming an EDA complex with ethanol (solid line), CO_2 while forming a hydrogen bond with ethanol (open circles). Inset: The same for CO_2 while forming an EDA complex with ethanol (solid line, same as in the main body), and two CO_2 molecules simultaneously forming an EDA complex with ethanol (line with open circles). The data are obtained from the CPMD run of the bulk 1:64 mixture.**

intramolecular angle of CO_2 molecules which satisfy the conditions of the hydrogen bond (with ethanol) is marginally narrower than that for molecules interacting with ethanol via the EDA interaction. The latter forces the CO_2 molecule to adopt a more bent geometry. Note that, a value of -0.985 in cosine of the angle implies that the O_C-C_C-O_C angle is 170^o, a deviation of 10^o from linearity. This is significant and may not be entirely captured in zero Kelvin quantum chemical calculations of isolated ethanol-CO_2 dimers. The distribution for molecules that neither form a hydrogen bond with ethanol nor interact

via the EDA interaction, i.e., *free CO_2* is also shown. This distribution is again narrower relative to the one for EDA interaction. As discussed earlier, it is also possible for two CO_2 molecules to simultaneously interact with the two lone pair electrons on the oxygen of the ethanol molecule. Such configurations are however rare. In the inset to Figure 4.9, we show the distribution of the intramolecular O_C-C_C-O_C angle for such CO_2 molecules. This distribution appears to be quite similar to that for a single EDA complex, although slightly narrower.

4.3.2 Vibrational Dynamics

Experimentally, ethanol-CO_2 interactions in the supercritical phase have been explored by examining the O-H stretching mode in ethanol. This mode is known to undergo a red shift in frequency relative to its value in gas phase [24]. Besnard and coworkers [28] have observed a red shift in the OD stretching frequency ν_{OD} as a function of increasing pressure for deuterated ethanol present in scCO_2. The ν_{OD} stretching mode of the ethanol monomer was observed to be at 2700 cm^{-1} at 120^{o}C. The spectral shift with increase in pressure was attributed to an attractive interaction between ethanol and carbon dioxide. Early spectroscopic experiments focused on the aggregation of methanol molecules themselves in scCO_2 at high concentrations [25]. Thus the shifting of the OH stretching mode to lower frequencies in these samples could also be due to the formation of hydrogen bond between alcohol molecules themselves. Here, we study the effect of the interactions between the single alcohol molecule and CO_2 in the supercritical phase on their vibrational spectra. First, we discuss the spectral features associated with the bending mode of carbon dioxide, and follow it up with those observed for the stretching of the hydroxyl group of d-ethanol.

CO_2 in bulk

Figure 4.10 compares the ν_2 bending mode of CO_2 in the bulk mixture and in the gas phase. It can be clearly observed that both the curves are peaked at 613 cm^{-1}. CO_2

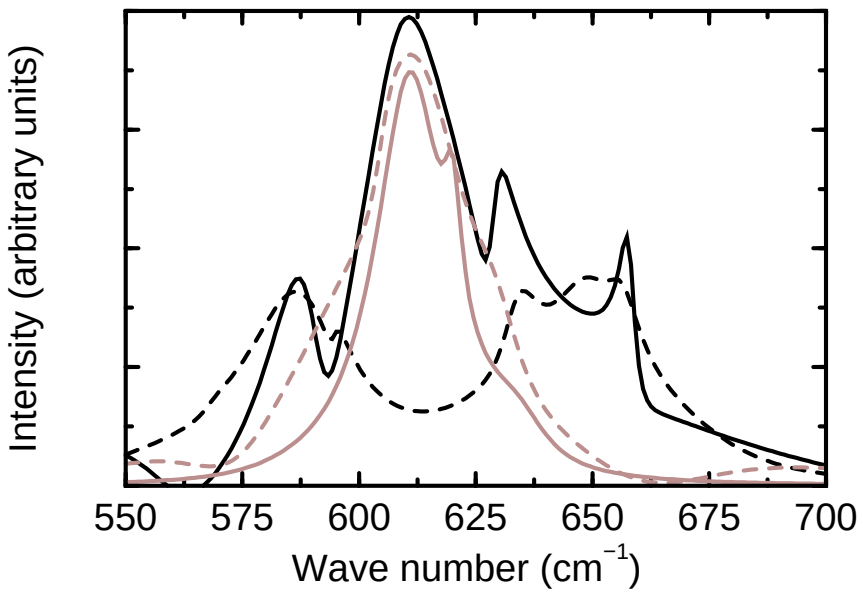

Figure 4.10: **Power spectrum of CO_2 molecules in the bending region. Total bending mode in the bulk mixture (black solid line), In-plane (black dashed line) and out-of-plane (gray/brown solid line) modes in bulk, and for the CO_2 monomer (gray/brown dashed line) at 318.15K.**

in bulk shows an additional peak at 633 cm^{-1} and a shoulder at 589 cm^{-1}. In contrast, the isolated CO_2 monomer does not show any split in the bending mode, consistent with its $D_{\infty h}$ symmetry. Thus the CO_2 bending mode is doubly degenerate under isolated conditions. This degeneracy gets lifted due to near neighbour interaction with other molecules, as will be discussed in sections 3.2.2 and 3.2.3.

A recent study on Raman spectroscopy of CO_2-acetone and CO_2-ethanol binary mixtures [60], shows that the removal of degeneracy in the bending mode of CO_2 is due to charge transfer interactions between the two species. A similar kind of spectral behaviour of CO_2 has been observed by Kazarian *et al* [61] for molecules of CO_2 gas interacting with the carbonyl side group of poly(methyl methacrylate) (PMMA), and by Dartois *et al* [32] at low temperatures in CO_2-methanol mixtures. The PMMA-CO_2 work shows a change in the behavior of the bending mode of CO_2 under three different conditions – when CO_2 is in gas phase, when the PMMA film is impregnated with CO_2, and after removal of gaseous CO_2 from the system. For the second case, three peaks in this mode were assigned to

free CO_2 (at 667 cm^{-1}), in-plane mode (654 cm^{-1}), and out-of-plane (662 cm^{-1}) mode, the last two arising due to the EDA interaction between the polymer and CO_2 molecule. Our calculations agree with experiments on the fact that multiple peaks are observed for the CO_2 part of the infrared spectrum [62]. However the calculations consistently predict lower values for these peak positions relative to the experiments. This red shift could arise due probably to the nature of the exchange and correlation approximations as well as due to the lower value of the energy cutoff employed here. Determination of exact frequencies of vibration would require calculations with probably a 120Ry cutoff, which is beyond the scope of this work. In addition, the state point of our calculations is 45^oC and 140 bar, while the experimental data is at 40^oC and 400 bar.

We delve further into the microscopic origin of these multiple peaks. In order to accomplish this task, we have decomposed the total CO_2 bending mode into two parts: in-plane and out-of-plane modes which are defined with respect to the instantaneous O_C-C_C-O_C plane of each CO_2 molecule. The in-plane bending mode of CO_2 in the ethanol-CO_2 supercritical fluid shows two distinct peaks at around 589 cm^{-1} (present as a shoulder in the total CO_2 spectra) and at 636 cm^{-1}. The out-of-plane mode is peaked at 613 cm^{-1} which corresponds to the fundamental ν_2 mode of CO_2 in the ethanol-CO_2 mixture. Experimental studies on mixtures of CO_2 and Lewis bases using FTIR spectroscopy reveals the splitting of the CO_2 bending mode with red shifted in-plane and blue shifted out-of-plane bending modes where the definition of plane was different [63] from ours.

We can infer two reasons for the splitting of the in-plane bending mode of CO_2. These are: (i) the formation of an EDA complex between CO_2 and ethanol, and (ii) the formation of an EDA-like complex between CO_2 molecules themselves. In order to understand this further, we have compared the CO_2 spectrum of the bulk ethanol-CO_2 solution with those obtained from a ethanol-CO_2 EDA cluster, and a CO_2 dimer cluster. The latter spectra are obtained once again from individual MD runs at a low temperature of 10K, each of length around 8ps. The low temperature was employed in order to prevent the EDA

complex from disintegrating as well as to obtain sharp spectral features.

Isolated ethanol-CO_2 EDA complex

The spectrum for the ethanol-CO_2 EDA complex shows two clear peaks (Figure 4.11), one at 604 cm^{-1} and another at 618 cm^{-1}. Importantly, the spectrum has no feature at 612

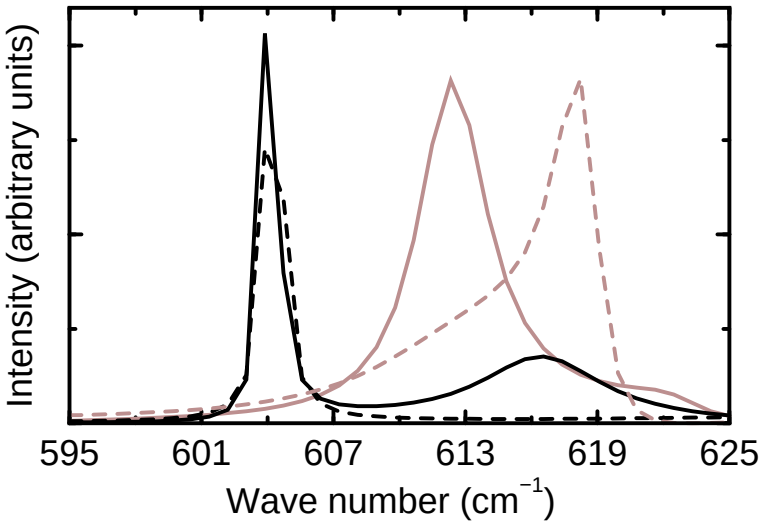

Figure 4.11: ν_2 **bending mode of ethanol-CO_2 EDA complex and of CO_2 monomer at 10K obtained as power spectrum from CPMD runs. Total EDA bending mode (black solid line), in-plane (black dashed line) and out-of-plane (gray/brown dashed line) modes, and for the CO_2 monomer (gray/brown solid line).**

cm^{-1}, the frequency of vibration observed for an isolated CO_2 molecule. In the isolated ethanol-CO_2 EDA complex, the in-plane bending mode is present at 604 cm^{-1} and the out-of-plane mode is at 618 cm^{-1}.

Isolated CO_2-CO_2 EDA complex

We now examine the vibrational spectrum of a dimer cluster of CO_2 in Figure 4.12. Here, the in-plane modes are present at 592, 611, and 625 cm^{-1} while the out-of-plane bending mode is present at 614 cm^{-1} with a small hump at 596 cm^{-1}. The in-plane bending mode of CO_2 in the dimer and in bulk exhibit similar behaviour leaving aside the thermal broadening in the bulk data. It is thus confirmed that the lone pair on the donating oxygen

atom of a CO_2 molecule interacts with the carbon atom of an acceptor CO_2 molecule, thus giving rise to the distorted T-shaped EDA complex. From these spectral analyses one can

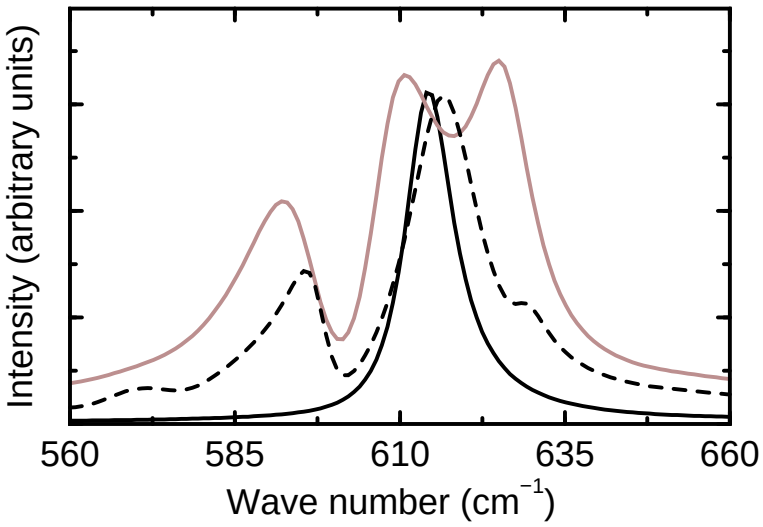

Figure 4.12: ν_2 **bending mode of CO_2 dimer at 10K. Total bending mode (black solid line), in-plane (gray/brown solid line) and out-of-plane (black dashed line) modes.**

conclude that the character of Lewis acid-base interaction between the two categories of EDA complexes are likely to be different. In the CO_2-CO_2 EDA complex the out-of-plane mode remains unaffected by LA-LB interaction and in the ethanol-CO_2 EDA complex it gets shifted to 618 cm^{-1}.

Thus the ν_2 mode of the CO_2 dimer exhibits a close resemblance to that in bulk. This is to be expected as the concentration of ethanol in our solution is small. In conclusion, one can argue that the major reason for the splitting in the bending mode of CO_2 in the 1:64 system is due to CO_2-CO_2 LA-LB interaction, and the minor contribution is the Lewis acid-base interaction between ethanol and CO_2.

Ethanol spectrum

The vibrational density of states of d-ethanol in this 1:64 bulk solution as well as in the isolated configuration are shown in Figure 4.13. The inset shows the same in the region of the OD stretching in expanded scale. The stretching frequency is observed at 2536

cm^{-1} for the isolated ethanol which is found to be shifted to around 2400 cm^{-1} in 1:64 bulk mixture. This is to be compared to the experimental value of 2690 cm^{-1} [28]. Note

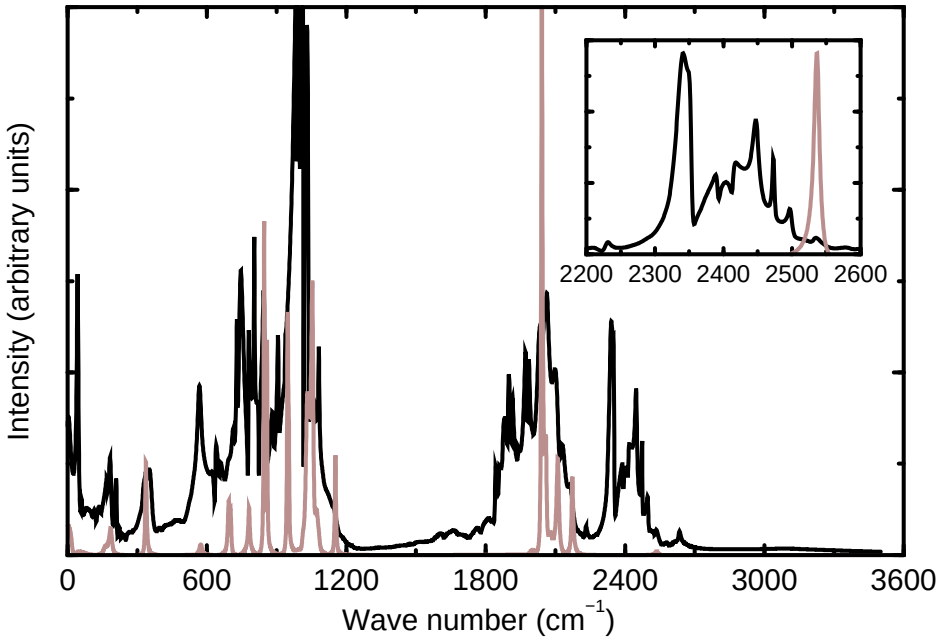

Figure 4.13: **Total vibrational spectrum of d-ethanol in the bulk mixture at 318.15K (black line) and as a monomer in gas phase (gray/brown line) at 10K. Inset shows vibrational spectra of hydroxyl oxygen of ethanol molecule for both the cases in the OD stretching region. In the inset, the intensity of the monomer spectrum has been scaled by an order of magnitude for the sake of comparison.**

that the concentration of ethanol in the recent experiments of Besnard and coworkers [28] is 6×10^{-3} mol.L^{-1}, while it is 0.248 mol.L^{-1} in our simulations. Also, the experiments were conducted at a temperature of 120^{o}C, while our simulations were performed at 45^{o}C. These differences in the state conditions of the sample could also explain the difference in OD stretching frequency between our calculations and experiment, apart from the DFT approximation. However, crucially we agree with experiments in the observation of a red shift in the OD stretching frequency upon complexation.

4.4 Conclusions

We have carried out Car-Parrinello molecular dynamics simulation studies of a system containing one ethanol molecule soaked in 64 molecules of carbon dioxide, under supercritical conditions. The current calculations improve upon our earlier work on pure $scCO_2$ in two aspects: (i) the system size is twice as large, and (ii) the use of exchange and correlation functionals which include correction terms in the gradient of the electronic density in lieu of the local density approximation. The increase in system size is expected to address issues related to the absence of a clear second neighbor shell in our previous work, while the gradient corrections enhances the accuracy of weak interactions in this solvent. The focus of this work is to shed light on microscopic interactions prevailing in a mixture of carbon dioxide and ethanol – the latter is widely used as a cosolvent to enhance the solubility of polar solutes in $scCO_2$. The important observations from our study are as follows: Carbon dioxide and ethanol can favorably interact with each other by either forming an electron donor-acceptor complex or through the formation of a hydrogen bond. Both interactions are directional. In the EDA complex, the oxygen atom of ethanol acts as an electron donor and the carbon atom of CO_2 acts as an acceptor. Our observations on both isolated (gas phase) complexes as well as on the bulk mixture at finite temperature show that the EDA interaction is favored more than hydrogen bonding. The EDA complex is thus the preferred one both in terms of potential energy as well as in free energy terms. The ratio of their occurrence in bulk solution is around 4:1. The dependence of this ratio as a function of increasing ethanol concentration needs to be explored.

The directionality of the EDA interaction is such that the preferred orientation of the carbon atom of an approaching CO_2 molecule is along the direction of the lone pair of electrons on the ethanol oxygen. This Lewis acid-base interaction leads to a considerable deviation from linearity of the carbon dioxide molecule. We have also found evidence for the occurrence of two CO_2 molecules simultaneously interacting with ethanol via LA-LB type of an arrangement. However, their population is relatively rare, and only 10% of

EDA complexes are of such a variety. The non-linearity in the backbone angle of CO_2 lifts the degeneracy of its ν_2 bending mode. Thus in this region of frequency, several spectral features are observed. These have been interpreted through our simulations on isolated complexes as well as by projection of atomic velocities on the O_C-C_C-O_C plane, as due to in-plane and out-of-plane bending vibrations. The distinction between these bending vibrations are caused by the association of a central CO_2 molecule with other carbon dioxide molecules or with ethanol. The current calculations have provided a microscopic perspective to ethanol-CO_2 interactions in the bulk, supercritical phase. Further simulations on higher mole fractions of ethanol need to be performed in order to complete this understanding. It may also be pertinent to employ other exchange-correlation functionals such as the PBE [64] to verify and augment the current results. Modeling of industrially relevant solutes such as caffeine in such solvent mixtures are also being pursued.

Bibliography

[1] M. Saharay, S. Balasubramanian, *ChemPhysChem* **5**, 1442-1445 (2004).

[2] X. Zhang, B. Han, Z. Hou, J. Zhang, Z. Liu, T. Jiang, J. He, H. Li, *Chem. Eur. J.* **8**, 5107-5111 (2002).

[3] T. Tassaing, P. Lalanne, S. Rey, F. Cansell, M. Besnard, *Ind. Eng. Chem. Res.* **39**, 4470-4475 (2000).

[4] P. Raveendran, Y. Ikushima, S. L. Wallen, *Acc. Chem. Res.* **38**, 478-485 (2005).

[5] S. Li, S. Hartland, *J. Supercrit. Fluids* **5**, 7-12 (1992).

[6] M. J. Noh, T. G. Kim, I. K. Hong, K. P. Yoo, *J. Chem. Eng.* **12**, 48-55 (1995).

[7] J. C. Gonzalez, M. R. Vieytes, J. M. Vieites, L. M. Botana, *J. Am. Oil Chem. Soc.* **78**, 77-81 (2001).

[8] D. L. Tomasko, B. L. Knutson, F. Pouillot, C. L. Liotta, C. A. Eckert, *J. Phys. Chem.* **97**, 11823-11834 (1993).

[9] J. Lu, B. Han, H. Yan, *Phys. Chem. Chem. Phys.* **1**, 3269-3276 (1999).

[10] D. L. Tomasko, B. L. Knutson, F. Pouillot, C. L. Liotta, C. A. Eckert, *J. Phys. Chem.* **97**, 11823-11834 (1993).

[11] J. Lu, B. Han, H. Yan, *Phys. Chem. Chem. Phys.* **1**, 3269-3276 (1999).

[12] Y. Iwai, M. Uno, H. Nagano, Y. Arai, *J. Supercrit. Fluids* **28**, 193-200 (2004).

[13] B. Y. Shekunov, P. Chattopadhyay, J. Seitzinger, R. Huff, *Pharm. Res.* **23**, 196-204 (2006).

[14] J. Jin, C. Zhong, Z. Zhang, Y. Li, *Fluid Phase Equilibria* **226**, 9-13 (2004).

[15] Q. Li, Z. Zhang, C. Zhong, Y. Liu, Q. Zhou, *Fluid Phase Equilibria* **207**, 183-192 (2003).

[16] P. W. Bell, A. J. Thote, Y. Park, R. B. Gupta, C. B. Roberts, *Ind. Eng. Chem. Res.* **42**, 6280-6289 (2003).

[17] P. Raveendran, S. L. Wallen, *J. Am. Chem. Soc.* **124**, 12590-12599 (2002).

[18] R. D. Amos, A. D. Buckingham, J. H. Williams, *Molec. Phys.* **39**, 1519-1526 (1980).

[19] B. Hemmaplardh, A. D. King, *J. Phys. Chem.* **76**, 2170-2175 (1972).

[20] S. K. Gupta, R. D. Lesslie, A. D. King, *J. Phys. Chem.* **77**, 2011-2015 (1973).

[21] C. M. V. Taylor, S. Bai, C. L. Mayne, D. M. Grant, *J. Phys. Chem. B* **101**, 5652-5658 (1997).

[22] M. Kanakubo, T. Aizawa, T. Kawakami, O. Sato, Y. Ikushima, K. Hatakeda, N. Saito, *J. Phys. Chem. B* **104**, 2749-2758 (2000).

[23] M. Yamamoto, Y. Iwai, T. Nakajima, Y. Arai, *J. Phys. Chem. A* **103**, 3525-3529 (1999).

[24] G. G. Yee, J. L. Fulton, R. D. Smith, *J. Phys. Chem.* **96**, 6172-6181 (1992).

[25] Fulton, J. L.; Yee, G. G.; Smith, R. D. *J. Am. Chem. Soc.* **113**, 8327-8334 (1991).

[26] A. Wesch, N. Dahmen, K. H. Ebert, *Ber. Bunsenges. Phys. Chem.* **100**, 1368-1371 (1996).

[27] Y. Danten, T. Tassaing, M. Besnard, *J. Phys. Chem. A* **106**, 11831-11840 (2002).

[28] P. Lalanne, T. Tassaing, Y. Danten, F. Cansell, S. C. Tucker, M. Besnard, *J. Phys. Chem. A* **108**, 2617-2624 (2004).

[29] H. Li, X. Zhang, B. Han, J. Liu, J. He, Z. Liu, *Chem. Eur. J.* **8**, 451-456 (2002).

[30] P. Ehrenfreund, A. C. A. Boogert, P. A. Gerakines, A. G. G. M. Tielens, E. F. Dishoeck, *Astron. Astrophys.* **328**, 649-669 (1997).

[31] P. Ehrenfreund, E. Dartois, K. Demyk, L. d'Hendecourt, *Astron. Astrophys.* **339**, L17-L20 (1998).

[32] E. Dartois, K. Demyk, L. d'Hendecourt, P. Ehrenfreund, *Astron. Astrophys.* **351**, 1066-1074 (1999).

[33] A. Koltz, T. Ward, E. Dartois, *Astron. Astrophys.* **416**, 801-810 (2004).

[34] M. H. Jamroz, J. Cz. Dobrowolski, K. Bajdor, M. A. Borowiak, *J. Mol. Struct.* **349**, 9-12 (1995).

[35] S. R. P. Rocha, K. P. Johnston, R. E. Westacott, P. J. Rossky, *J. Phys. Chem. B* **105**, 12092-12104 (2001).

[36] Z. Zhang, Z. Duan, *J. Chem. Phys.* **122**, 214507-214515 (2005).

[37] S. Nugent, B. M. Ladanyi, *J. Chem. Phys.* **120**, 874-884 (2004).

[38] J. M. Stubbs, J. I. Siepmann, *J. Chem. Phys.* **121**, 1525-1534 (2004).

[39] M. Saharay, S. Balasubramanian, *J. Chem. Phys.* **120**, 9694-9702 (2004).

[40] Y. Zhang, J. Yang, Y. Yu, *J. Phys. Chem. B* **109**, 13375-13382 (2005).

[41] R. Car, M. Parrinello, *Phys. Rev. Lett.* **55**, 2471-2474 (1985).

[42] J. Hutter, P. Ballone, M. Bernasconi, P. Focher, E. Fois, S. Goedecker, D. Marx, M. Parrinello, M. E. Tuckerman, CPMD Version 3.9.1, Max Planck Institut fuer Festkoerperforschung, Stuttgart, and IBM Zurich Research Laboratory, 1990-2005.

[43] M. E. Tuckerman, D. A. Yarne, S. O. Samuelson, A. L. Hughes, G. Martyna, *J. Comput. Phys. Commun.* **128**, 333-376 (2000).

[44] A. D. Becke, *Phys. Rev. A* **38**, 3098-3100 (1988).

[45] C. Lee, W. Yang, R. G. Parr, *Phys. Rev. B* **37**, 785-789 (1988).

[46] J. A. Morrone, M. E. Tuckerman, *J. Chem. Phys.* **117**, 4403-4413 (2002).

[47] N. Troullier, J. L. Martins, *Phys. Rev. B* **43**, 1993-2006 (1991).

[48] M. J. Frisch, G. W. Trucks, H. B. Schlegel, G. E. Scuseria, M. A. Robb, J. R. Cheeseman, V. G. Zakrzewski, J. A. Montgomery, R. E. Stratmann, J. C. Burant, S. Dapprich, J. M. Millam, A. D. Daniels, K. N. Kudin, M. C. Strain, O. Farkas, J. Tomasi, V. Barone, M. Cossi, R. Cammi, B. Mennucci, C. Pomelli, C. Adamo, S. Clifford, J. Ochterski, G. A. Petersson, P. Y. Ayala, Q. Cui, K. Morokuma, D. K. Malick, A. D. Rabuck, K. Raghavachari, J. B. Foresman, J. Cioslowski, J. V. Ortiz, B. B. Stefanov, G. Liu, A. Liashenko, P. Piskorz, I. Komaromi, R. Gomperts, R. L. Martin, D. J. Fox, T. Keith, M. A. Al-Laham, C. Y. Peng, A. Nanayakkara, C. Gonzalez, M. Challacombe, P. M. W. Gill, B. G. Johnson, W. Chen, M. W. Wong, J. L. Andres, M. Head-Gordon, E. S. Replogle, J. A. Pople, Gaussian 98, revision A.9; Gaussian,Inc.: Pittsburgh, PA, 1998.

[49] A. D. Becke, *J. Chem. Phys.* **98**, 5648-5652 (1993).

[50] MacKerell, A. D.; Bashford, D.; Bellott, M.; Dunbrack, R. L.; Evanseck, J. D.; Field, M. J.; Fischer, S.; Gao, J.; Guo, H.; Ha, S.; Joseph-McCarthy, D.; Kuchnir, L.; Kuczera, K.; Lau, F. T. K.; Mattos, C.; Michnick, S.; Ngo, T.; Nguyen, D. T.; Prodhom, B.; Reiher, W. E.; Roux, B.; Schlenkrich, M.; Smith, J. C.; Stote, R.; Straub, J.; Watanabe, M.; Wiorkiewicz-Kuczera, J.; Yin, D.; Karplus, M. *J. Phys. Chem. B* **102**, 3586-3616 (1998).

[51] J. G. Harris, K. H. Yung, *J. Phys. Chem.* **99**, 12021-12024 (1995).

[52] G. J. Martyna, M. L. Klein, M. Tuckerman, *J. Chem. Phys.* **97**, 2635-2643 (1992).

[53] B. Chen, J. J. Potoff, J. I. Siepmann, *J. Phys. Chem. B* **105**, 3093-3104 (2001).

[54] J. M. Stubbs, J. I. Siepmann, *J. Am. Chem. Soc.* **127**, 4722-4729 (2005).

[55] J. Chen, A. J. Shaka, V. A. Mandelshtam, *J. Magn. Reson.* **147**, 129-137 (2000).

[56] E. Knozinger, P. Beichert, *J. Phys. Chem.* **99**, 4906-4911 (1995).

[57] K. Laasonen, M. Sprik, M. Parrinello, *J. Chem. Phys.* **99**, 9080-9089 (1993).

[58] A. Chandra, *Phys. Rev. Lett.* **85**, 768-771 (2000).

[59] M. P. Allen, D. J. Tildesley, *Computer Simulation of Liquids*; Clarendon Press; Oxford, 1987.

[60] M. I. Cabaco, Y. Danten, T. Tassaing, S. Longelin, M. Besnard, *Chem. Phys. Lett.* **413**, 258-262 (2005).

[61] S. G. Kazarian, M. F. Vincent, F. V. Bright, C. L. Liotta, C. A. Eckert, *J. Am. Chem. Soc.* **118**, 1729-1736 (1996).

[62] Figure 3B of Yee et al [24], exhibits multiple peaks for the vibrational spectrum in the ν_2 bending region of pure $scCO_2$ at 40^oC and 400 bar. The splittings were however not commented upon in this original work.

[63] J. C. Meredith, K. P. Johnston, J. M. Seminario, S. G. Kazarian, C. A. Eckert, *J. Phys. Chem.* **100**, 10837-10848 (1996).

[64] J. P. Perdew, K. Burke, M. Ernzerhof, *Phys. Rev. Lett.* **77**, 3865-3868 (1996).

Chapter 5

Ab initio Molecular Dynamics Investigations of Structural, Electronic, and Dynamical Properties of Water in Supercritical Carbon dioxide

5.1 Introduction

In the previous chapter, we have characterized the nature of specific interactions between ethanol and carbon dioxide in ethanol/scCO_2 mixtures, where ethanol has been treated as a solute, using Car-Parrinello molecular dynamics (CPMD) simulations. The present chapter presents an extended study on the water/scCO_2 mixture. This binary mixture increases the solvation of organic molecules such as natural oil and waxy materials [1] due to enhanced interactions between the cosolvent (here, water), solvent, and the solute.

The solubility of water [2] in compressed CO_2 at various temperatures has been stud-

ied experimentally by measuring the second cross virial coefficients. The large negative values of these coefficients suggested chemical association between water and CO_2. Apart from conventional measurements of solubility [3], Fourier transform infrared (FTIR) spectroscopic measurements [4, 5] have demonstrated that water is less soluble in scCO_2 ($<$ 2.0 mol%). Three types of intermolecular interactions exist in a binary mixture : (i) solute/solute, (ii) solute/solvent, and (iii) solvent/solvent. Our recent work discussed in Chapter 3 has addressed the nature of solvent-solvent interactions in scCO_2 at different pressures [6]. In addition to the attractive forces due to induced dipole/dipole, and induced dipole-induced dipole interactions, dipole-quadrupole interactions can also contribute in water-CO_2 solutions. Danten et al. [7] have characterized the interaction of a solitary water in supercritical CO_2 through molecular dynamics simulations using empirical potentials. The results obtained from experiments and simulations show that electron donor-acceptor (EDA) interaction (where the oxygen of water is the donor and the carbon of carbon dioxide is the acceptor) plays a crucial role in the red shift and the broadening of the mid-infrared profiles associated with the ν_1 symmetric and ν_3 asymmetric OD stretching modes of D_2O. In a characterization of the water-CO_2 interface using MD simulations, Rossky and coworkers have demonstrated the existence of attractive interactions between the two molecules [8]. In this study, we employ *ab initio* molecular dynamics (AIMD) simulations to understand EDA and hydrogen bonded interactions in water/scCO_2 mixture.

AIMD simulation is a powerful tool that provides atomistic details of chemical processes and plays a major role in enabling the interpretation of experimental data of disordered systems [9]. Unlike classical MD simulations with empirical force fields, AIMD captures the effects of polarization due to a changing environment. Here we report results of AIMD simulations of a solitary water molecule solvated in supercritical carbon dioxide at three densities. Anticipating our results, we find significant changes in the molecular properties of the water molecule and its interaction with carbon dioxide with increasing

density. We follow this Introduction by providing the details of simulation. Subsequent to a discussion of the results, conclusions are drawn.

5.2 Simulation Details

Ab initio molecular dynamics simulations using the Car-Parrinello method [10] have been carried out for a system containing one molecule of heavy water (D_2O) in supercritical carbon dioxide (W/C). The structural, electronic and dynamical properties of this W/C mixture were obtained at densities, 0.84, 1.03, and 1.33 g/cc along an isotherm at 305.15K. As the convergence of pressure in such *ab initio* simulations would require the use of very large plane wave energy cutoffs, we use the experimentally determined equation of state [11], in order to estimate the pressure of the simulated system. Thus, the simulated systems would correspond to state points with pressures of 141, 612, and 3330 atm respectively. The concentration of water is 3.1 mol%. At such low concentrations of the solute, the critical properties of the binary mixtures with different solutes [12,13] remain nearly the same as that of pure $scCO_2$. The box length of each cubic supercell has been determined from the experimental density [11] of CO_2 at the corresponding temperature and pressure. All these systems were initially equilibrated by classical molecular dynamics simulations using the PINY-MD code [14] with model force fields for both CO_2 [15] and water [16]. The final configurations were then fed into density functional theory based Car-Parrinello molecular dynamics (CPMD) [10] simulations performed using the CPMD package [17]. Generalized gradient approximated functional for the exchange energy part in the form proposed by Becke [18], and a correlation functional of Lee, Yang, and Parr [19] (LYP) have been employed. In order to be able to use a larger time step, the hydrogen nuclei were treated as classical particles with the use of the mass of the deuterium isotope [20]. Other specifications for the CPMD calculations are similar to that of previously studied $scCO_2$ systems [6] (Chapter 3). Using this set of parameters, the adiabaticity between electronic and ionic part of the system was maintained throughout

the MD trajectory. Productive run lengths at 0.84, 1.03, and 1.33 g/cc were around 20, 20, and 21 ps respectively, leaving 2 ps of trajectory for equilibration at each density.

The main goal of this work is to characterize the solute-solvent interactions and organization in W/C binary mixtures. The properties of the solitary water molecule in these systems has been compared with liquid water. As a reference system, we generated a 15 ps CPMD trajectory for bulk liquid water consisting of 32 D_2O molecules at 305.15K in a cubic supercell of box length 15Å. In addition, for the sake of completeness, properties of molecular clusters of water have also been compared.

5.3 Results and Discussion

5.3.1 Structure

Pair Correlation Function

The density dependence of the intermolecular radial distribution functions between CO_2 molecules in the solution is similar to that in pure $scCO_2$ [6] (Chapter 3). This result is also consistent with our previous work on binary mixtures of $scCO_2$ at infinite dilution of solute [21] (Chapter 4). The pair correlation functions (rdf) between water and CO_2 molecules provide insights into the nature of interactions between these two molecular species. These are shown in Figure 5.1. The rdf, $g_{O_W C_C}(r)$ (Figure 5.1a) between the oxygen (O_W) atom of water and the carbon (C_C) atom of CO_2 exhibits a broad peak at 4.0Å at the lowest density along with a hump around 3.1Å. With increasing density, one can observe a shift in the peak positions to shorter distances and a formal pre-peak developing at 3.1Å. Using an empirical potential, Danten *et al* [7] have observed similar features, although weaker, under different thermodynamic conditions. We now investigate the origin of the two distinct peaks at the highest solvent density which appear at 3.1 and 4.0Å respectively. As reported in gas phase studies [22], the most stable configuration of a water-CO_2 molecular complex is planar and T-shaped, wherein the protons are directed

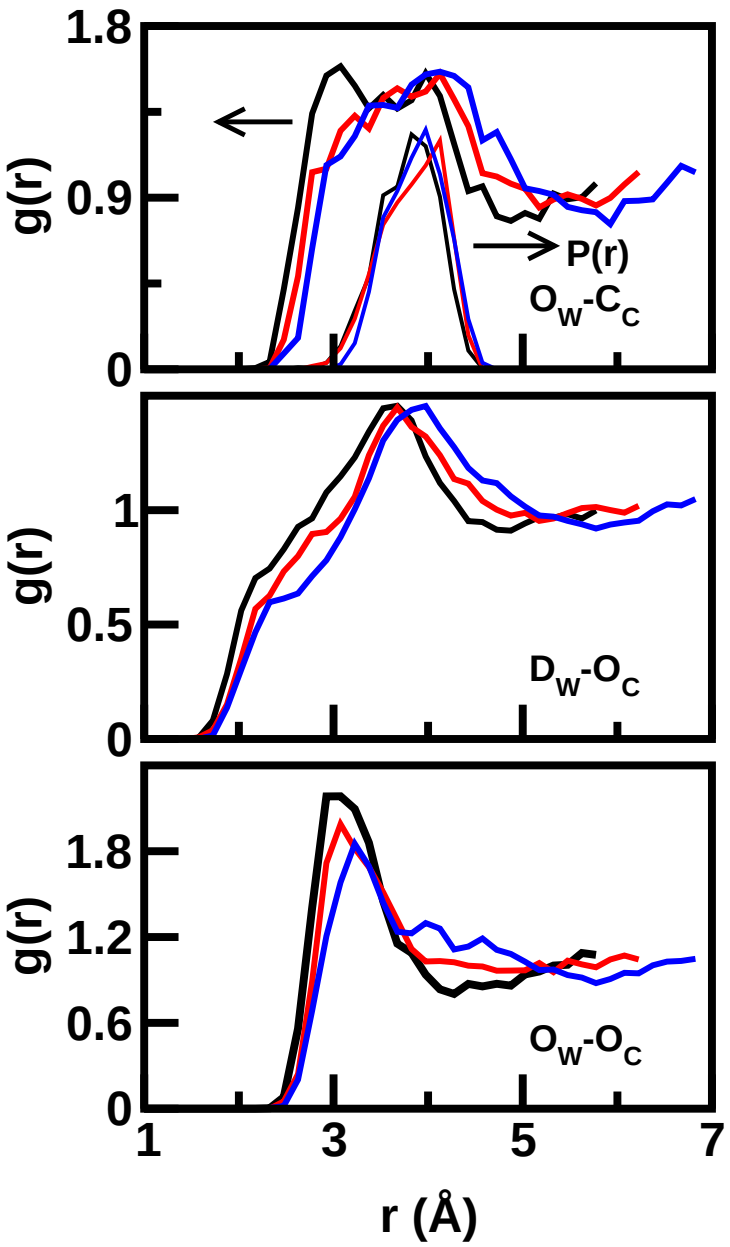

Figure 5.1: **Intermolecular partial radial distribution functions between D_2O and CO_2 for (a) oxygen atom (O_W) of D_2O and carbon atom (C_C) of CO_2, (b) oxygen atom (O_C) of CO_2 and hydrogen (D) of D_2O, (c) oxygen atom (O_C) of CO_2 and oxygen atom (O_W) of D_2O at solvent densities 0.84 (thick blue), 1.03 (thick red), and 1.33 g/cc (thick black). Also shown are probabilities of distances P(r) (thin lines), between the same pair when they satisfy the criteria for hydrogen bond.**

away from CO_2. This result is also supported by several experiments, the earliest being matrix isolation infrared spectroscopy [23]. The distance between C_C and O_W for this

electron donor-acceptor configuration in gas phase is around 2.9Å. Although the intensity of the first pre-peak in $g_{O_WC_C}(r)$ at the lowest density is less, its position suggests the possibility of EDA type interaction even in the fluid mixture.

In order to identify the peak at 4.0Å, we employ the standard geometric criteria [24] to define the hydrogen bond between D_2O and CO_2. These include conditions on the distance between the oxygen atoms, between D_W and O_C, as well as on the hydrogen bond angle. Shown in the same Figure 5.1a is the probability distribution of O_W-C_C distances when the molecules satisfy the hydrogen bond criteria. A comparison of this data with the $g_{O_WC_C}(r)$ indicates that the second peak in the radial distribution function at 1.33 g/cc arises due to a hydrogen bonded arrangement between CO_2 and D_2O.

FTIR spectroscopy investigations [23,25] on the role of hydrogen bonding in the water-CO_2 complex show that there is no marked difference in the OH stretching frequency in this complex from that of the water monomer. Thus, experimentally no hydrogen bond was found in this complex, under the conditions studied. In our simulations, the rdfs $g_{D_WO_C}(r)$ (Figure 5.1b) were studied at different densities of the solution. We notice similar effect of pressure on these pair correlation functions as has been observed in $g_{O_WC_C}(r)$. Interestingly, a weak shoulder appears around 2.5Å at the lowest pressure. Its position decreases and intensity increases with increasing density. The position of the first peak at all densities is between 3.5 and 3.9Å.

The enhanced local arrangement of solvent molecules around heavy water can also be noticed in $g_{O_WO_C}(r)$ (Figure 5.1c) in which the position of the first peak decreases from a value of 3.3Å at 0.84 g/cc to 2.9Å at 1.33 g/cc. The positions of the weak shoulder in $g_{O_CD_W}(r)$ and the first peak in $g_{O_CO_W}(r)$ closely resemble the conditions [24] for the presence of a hydrogen bonded complex. Thus, the local ordering of CO_2 molecules around heavy water indicates the possibility of existence of both EDA and hydrogen bonded moieties. An elaborate discussion on these interactions is provided in the following sections.

Intermolecular Angle Distribution

To characterize the intermolecular orientational preferences in the formation of a D_2O-CO_2 EDA complex, we define three parameters, d_{OC}, θ, and ϕ which are defined in a schematic, Figure 5.2. The cut-off distance (d_{OC}) between O_W and C_C for the EDA molecular complex was chosen to be 3.1Å, which is slightly larger than the first peak position in $g_{O_W C_C}(r)$.

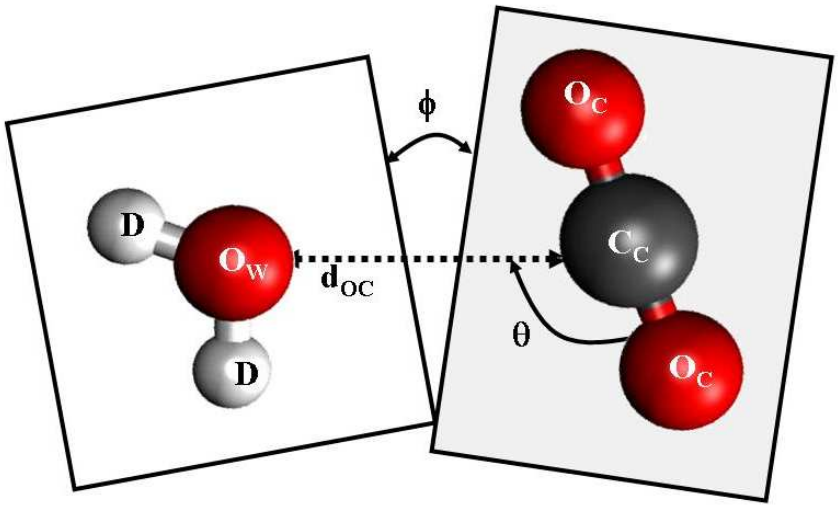

Figure 5.2: **Schematic illustration of D_2O-CO_2 EDA complex. ϕ represents the angle between the molecular planes of D_2O and CO_2; θ is the angle between CO_2 backbone vector and the vector (d_{OC}) connecting O_W and C_C.**

Figure 5.3a illustrates the distribution of the angle between the normal vectors to D_2O and CO_2 planes within this d_{OC} distance cut-off. At all solvent densities, these distributions show a preference for $Cos\phi = \pm 1$, i.e., the most probable ϕ value is around 180, or 0^o. The probability of water and CO_2 molecules to be coplanar decreases marginally with increasing density. At higher densities, a solute molecule gets surrounded by more number of solvent molecules. Thus, it is reasonable to visualize having two acceptor atoms (C_C) along the lone pair directions of O_W rather than a single C_C atom along the direction of D-O_W-D bisector vector. The deviation from coplanarity can thus be rationalized. For the representative configuration of the T-shaped EDA complex with C_{2v} symmetry, the

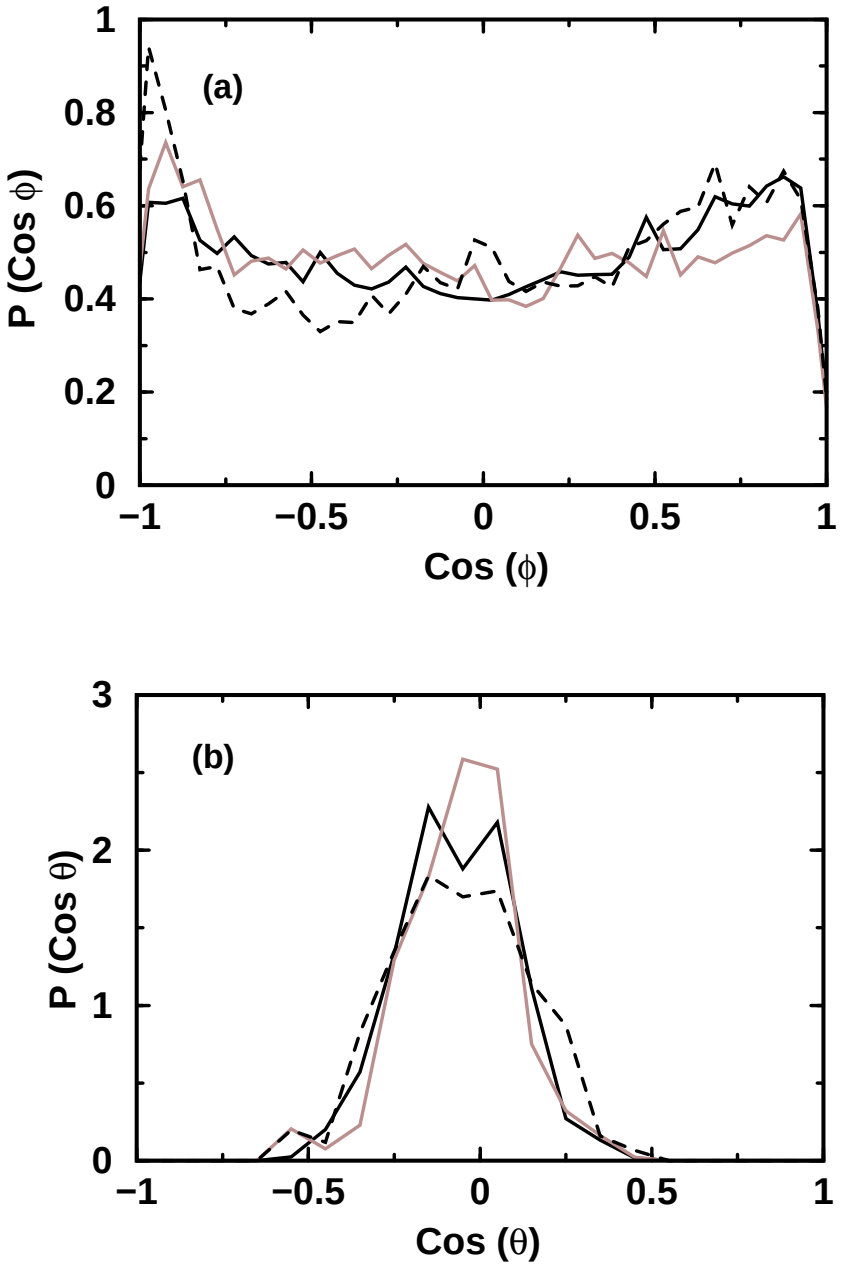

Figure 5.3: **Probability distribution of (a) Cos ϕ and Cos (b) θ at system densities: 0.84 (black dashed), 1.03 (gray), and 1.33 (black solid) g/cc for d_{OC} < 3.1Å . The cut-off value for d_{OC} was chosen from the position of first pre-peak in $g_{O_W C_C}(r)$.**

range of the angle (ϕ) between water and CO_2 planes was chosen to be $|\mathrm{Cos}(\phi)| > 0.87$. The intermolecular angle distribution, P(Cosθ), satisfying the constraints on d_{OC} and ϕ is shown in Figure 5.3b. The distributions are centered around cos(θ)=0, exemplifying the coplanarity of the EDA complex.

Hydrogen Bond

As discussed in the previous section, $g_{O_C D}(r)$ enables one to identify the formation of a hydrogen bond. In general, h-bonds are identified using one angle (O_W-D...O_C) and two distance ($d_{O_W O_C}$ and $d_{D_W O_C}$) constraints [24] between the participating molecules. In this paper, the hydrogen bond has been defined by: (i) $d_{DO_C} < 2.5$Å, (ii) $d_{O_W O_C} < 3.5$Å, (iii) angle $O_W - D \cdots O_C > 140^O$.

In the bulk W/C mixture, a water molecule could be singly or doubly hydrogen bonded to carbon dioxide molecules at a particular instant in time. This occurrence is sensitive to system density. The total occurrence of hydrogen bonded neighbors at the lowest and highest densities were found to be 32% and 64% respectively. Among these, around 4 and 13% are situations where the water molecule was found to be doubly hydrogen bonded. Similar to our earlier observations on the ethanol-CO_2 system [21], it is possible that the doubly hydrogen bonded species is at least partly entropically stabilized. Efforts to optimize its structure, hoping to preserve both its hydrogen bonds, under isolated conditions were futile.

D_2O-CO_2 Cluster

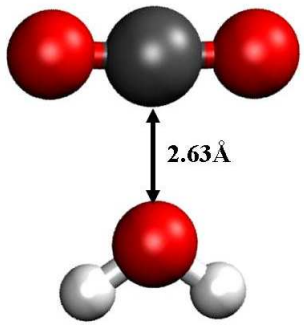

Figure 5.4: **Geometry optimized structure of D_2O-CO_2 EDA complex.**

Gas phase studies of D_2O-CO_2 complexes show that the T-shaped (Figure 5.4), planar geometry with the water hydrogen atoms directed away from the CO_2 molecule, is most stable [22,26–28]. The equilibrium distance between O_W and C_C in this structure is 2.63Å.

Our gas phase calculations within CPMD, shows that this structure is more stable over a hydrogen bonded one by 3.25 kcal/mol, in agreement with earlier work [22]. The experimentally observed induced dipole moment [22] of a CO_2 molecule upon complexation with water is 0.175 D. Also, *ab initio* calculations [29] of H_2O-CO_2 dimers report a non-linear geometry of CO_2 molecule in the T-shaped structure with a backbone angle of 177^o [29]. Our results on the electrostatics of the solute as well as on the geometry of the solvent molecules through simulations of the bulk system add support to these observations.

D_2O Structure

In Figure 5.5, we show the probability distributions of O-D bond distances and the D-O-D angle for the solitary water solvated in CO_2 at each density. The bond length distribution shows a unimodal behavior at the two lower densities, and a bimodal one at 1.33g/cc. The longer distance corresponds to that O-D bond in which the proton forms a hydrogen bond with carbon dioxide. It is remarkable that even a simple quantity such as the distribution of bond lengths in water can serve as a signature of molecular association. Such a transition from a state that is essentially like a free molecule to one that interacts strongly with the solvent can also be noticed in the distribution of D-O-D bond angles, shown in Figure 5.5b. Here, the distribution changes from a bimodal one at lower densities to a unimodal one at the highest density. The former behavior is also seen in CPMD simulations of an isolated water molecule, while the latter is seen in calculations of bulk, liquid water. The two peaks in the angle distribution for the isolated water or water in CO_2 at low densities, signifies the turning points of the oscillator. The damping of the amplitude of motion at higher densities (or in general, at higher strengths of interaction) leads to merging of the two peaks. Again, the behavior of the angle distributions is consistent with the conclusions drawn from the bond length distributions.

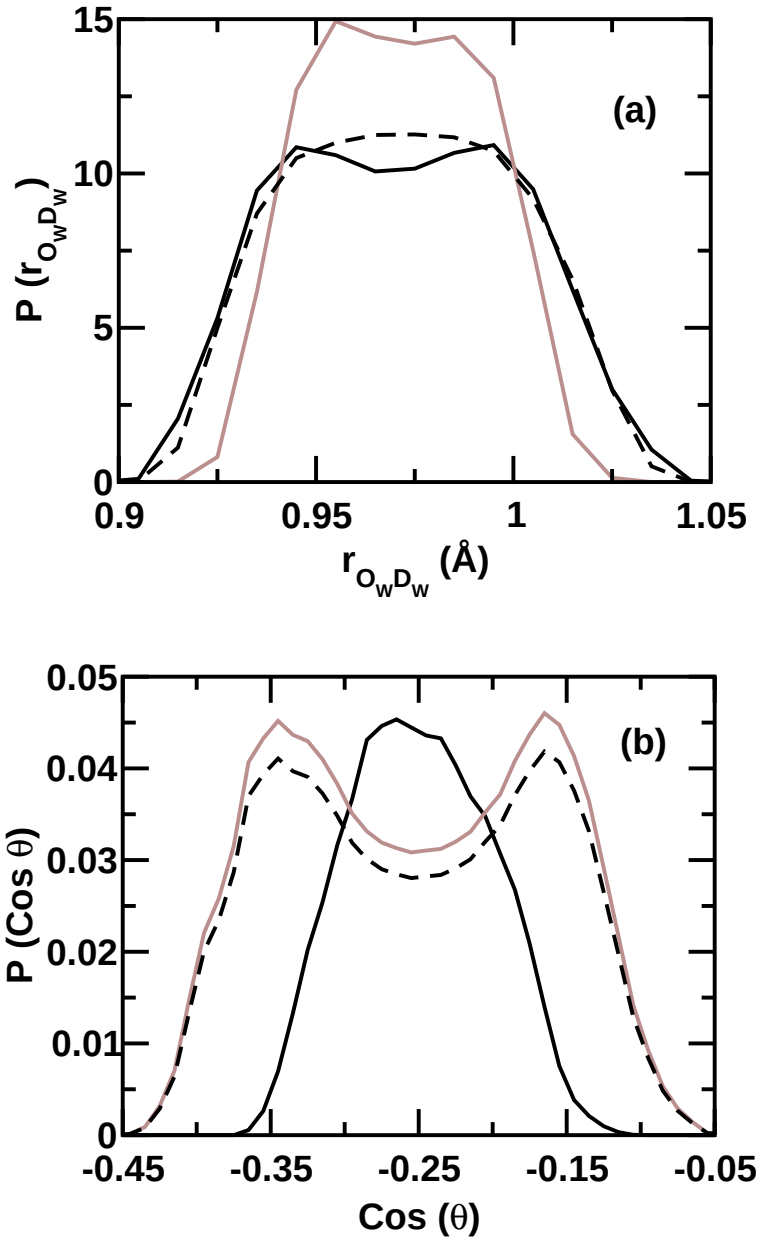

Figure 5.5: **Probability distributions of intramolecular (a) bond length and (b) angle of D_2O. Line descriptions are same as in Figure 5.3.**

CO_2 Structure

Figure 5.6 shows the intramolecular angle distributions (O-C-O) of CO_2 at two different conditions: when $r_{O_WC_C}$ is (i) less than 2.9Å, the distance between O_W and C_C in the optimized EDA complex and (ii) beyond this distance cut-off. A careful examination of these distributions for the first condition shows an increasing trend for attaining instanta-

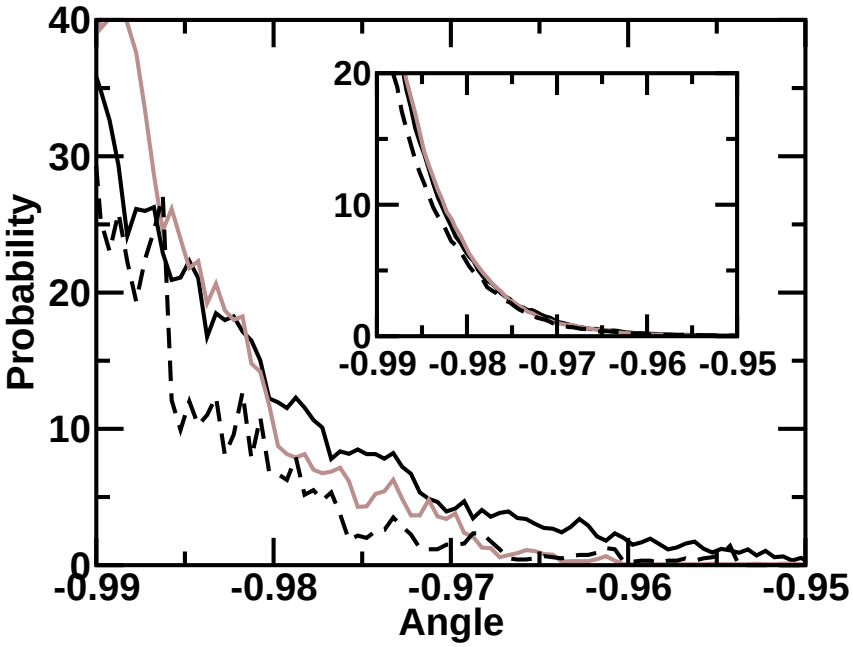

Figure 5.6: **Intramolecular O-C-O angle distributions of CO_2 in two environments depending upon the separation between O_W and C_C at 0.84 (black dashed line), 1.03 (gray line), and 1.33 (black solid line) g/cc.The distance cut-off has been chosen from the optimized geometry of electron-donor acceptor complex of D_2O-CO_2 under isolated conditions. Main body: For an interacting pair of D_2O and CO_2 with $d_{O_WC_C} < 2.9$Å. Inset: Non-interacting CO_2, i.e. $d_{O_WC_C} > 2.9$Å.**

neous CO_2 geometries away from linearity. On the other hand, the intramolecular angle distributions of non-interacting CO_2 molecules shows negligible change with density. To summarize, with increasing solvent density, CO_2 polarizes the solute (water) and in turn, exhibits stronger deviations from its gas phase structure.

5.3.2 Electrostatics

D_2O Dipole Moment

We use the maximally localized Wannier function [30, 31] method to study the effect of solute-solvent interactions on the dipole moment of water.This representation of the electronic ground state of periodic systems by the localized Wannier orbitals has been used to investigate the bonding properties in amorphous silicon [32], hydrogen bonding in

water [33] and many other systems. In particular, we show in the following discussion that the knowledge of the positions of Wannier function centers (WFC) captures the effect of EDA and hydrogen bonded interactions between different molecular species. Eight valence electrons per water molecule accounts for four doubly occupied WFCs, two along the O-D covalent bonds, and the other two along the lone pair directions of the oxygen atom.

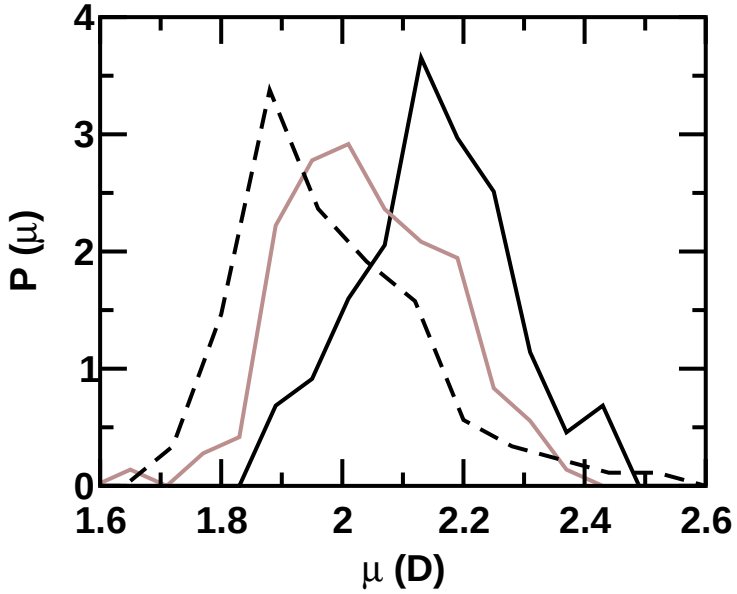

Figure 5.7: **Probability distributions P(μ) of the magnitude of D_2O dipole moment at densities 0.84 (dashed black line), 1.03 (gray line), and 1.33 (black solid line) g/cc.**

At each density in our simulations, one hundred configurations were collected from the productive trajectory at equal intervals. The electronic contribution to the dipole moment ($\vec{\mu}$) of the water molecule obtained through WFC analyses and the ion contributions from their coordinates were used in the calculation of the molecular dipole moment. Figure 5.7 shows the probability distribution of μ (the magnitude of the dipole moment) at the three densities. A progressive shift of the peak position towards higher values can be seen with increasing system density. The most probable values for these distributions at densities of 0.84, 1.03, and 1.33 g/cc are around 1.88, 2.0, and 2.13 Debye respectively. The value at the lowest density is in good agreement with the gas phase experiments [34]. First

principle calculations on pure water clusters [35] show that the change in the geometry of hydrogen bonding between water molecules with the increase in cluster size is one of the causes for enhancement in the molecular dipole moment.

The weakening of the D_2O covalent bond upon formation of a hydrogen bond with near neighbors is a well known phenomenon. This observation can explain the enhanced dipole moment of water in this solution by two ways : (i) out-of-plane inclination (θ_1) of the dipole vector ($\vec{\mu}$), (ii) deviation (θ_2) of $\vec{\mu}$ from the D-O_W-D bisector vector. Figure 5.8 compares the probability distributions of the cosines of these angles in the water-CO_2 mixtures with that in pure, liquid water. Note that in the binary mixtures, the dipole vector of water is almost coplanar to its molecular plane (Figure 5.8a) although at the highest density, deviations of $\vec{\mu}$ away from this plane are not as forbidding as at lower densities. With increasing density, one finds a gradual change towards the behavior in neat water in these distributions. The deviation of the orientation of $\vec{\mu}$ from the vector that bisects the two O-D bonds (Figure 5.8b) also increases with solvent density. This is likely due to the formation of a hydrogen bond with one of the protons of water which will cause the molecule to lose its C_2 rotation symmetry, in a strict sense. Thus, in water-scCO_2 binary mixtures, the deviation of the dipole angle (θ_2) from the bisector plays a crucial role in the enhanced dipole moment of water.

Our simulation results indicate that water in scCO_2 is almost immiscible in the lowest solvent density, as the value of the most probable dipole moment is close to that of a monomer. Despite the peak position, the distribution of the dipole magnitude shows a long tail up to 2.6 D which indicates the presence of weak interactions with the surrounding environment. Not only the hydrogen bond, but the EDA interaction also plays a prominent role in the solvation of D_2O.

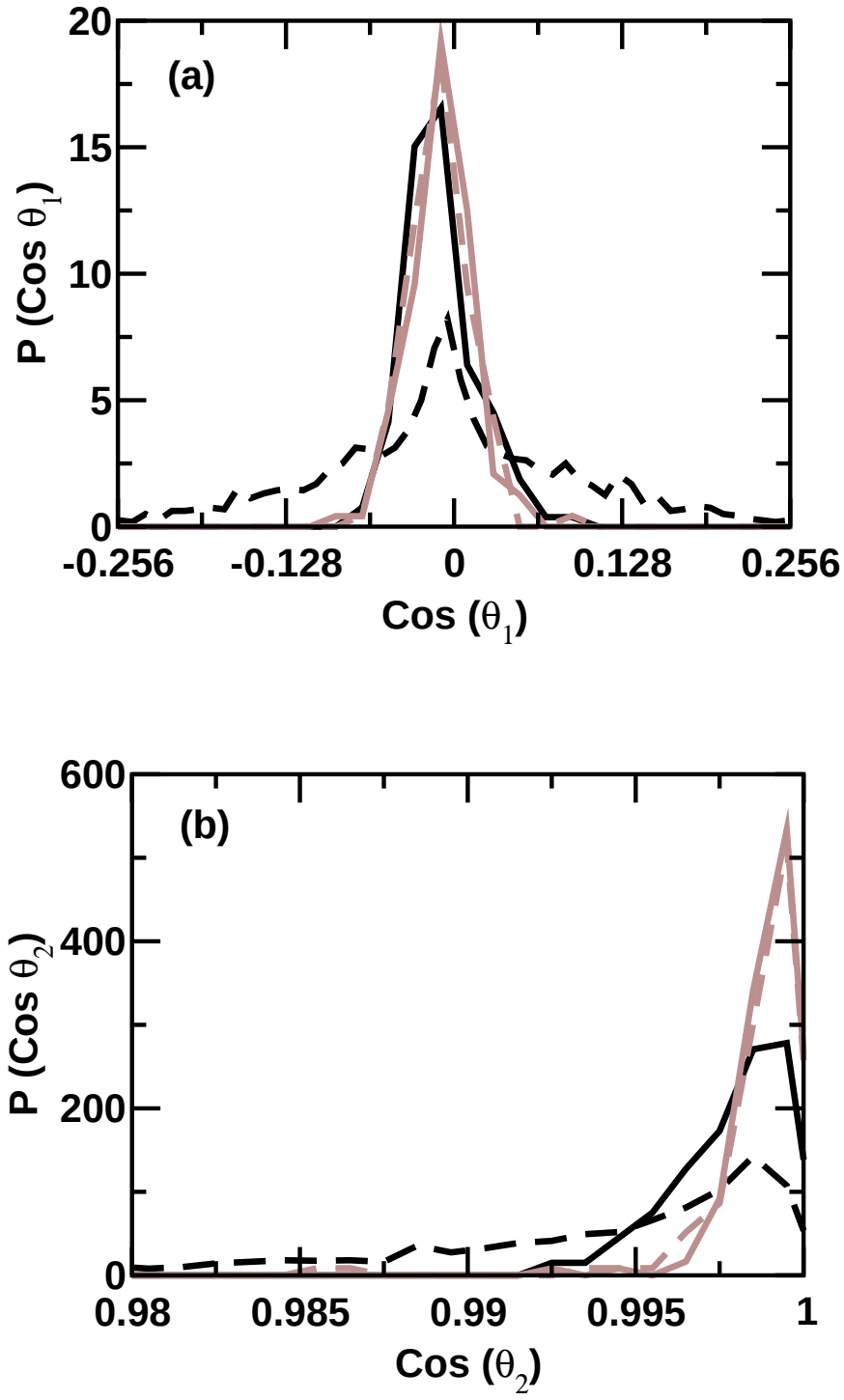

Figure 5.8: **Probability distributions of (a) Cos(θ_1) where θ_1 is the angle between the D_2O dipole vector and the normal to its plane (b) Cos(θ_2) where θ_2 is the angle between the dipole and bisector vectors of D_2O at densities 0.84 (dashed gray), 1.03 (gray), 1.33 (black solid) g/cc and for liquid D_2O (dashed black).**

5.3.3 Dynamics

Vibrational Density of States

We have reported the vibrational density of states of pure $scCO_2$ at different pressures along an isotherm, elsewhere [6] (Chapter 3). Our investigations showed that under the conditions studied, the effect of pressure on the bending, symmetric, and asymmetric stretch modes of CO_2 was almost negligible, except in the far-IR region. Thus, we report here only the effect on the vibrational density of states of the solitary heavy water upon increasing the density of the solution. A large number of experimental [36–38] and theoretical [39] studies have been performed on the vibrational spectrum of liquid water. The spectrum is characterized by four major features: libration-translation, bending, and OH stretching modes. The experimentally [40] obtained peak positions for heavy water corresponding to these modes appear at 165, 505, 1220, and 2500 cm^{-1}, respectively.

Low-frequency mode

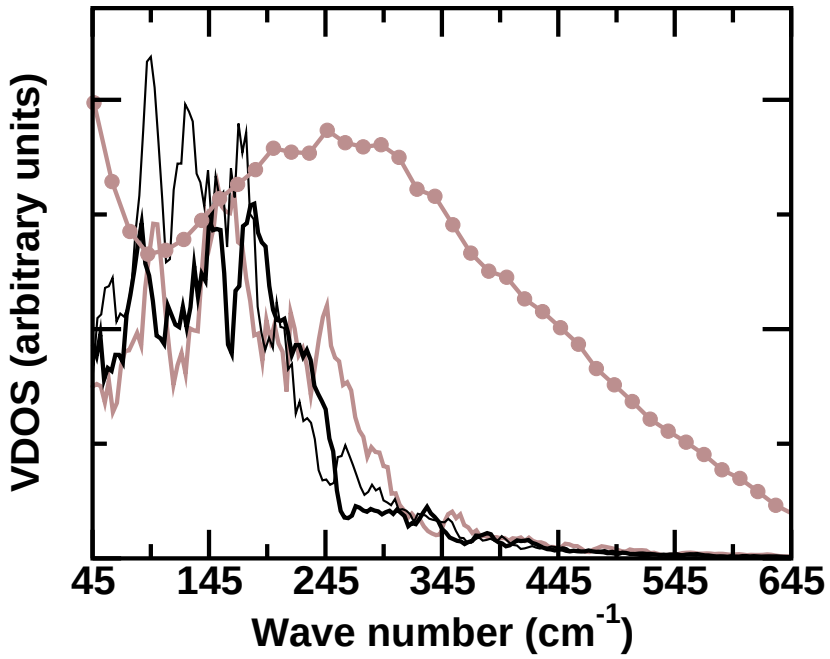

Figure 5.9: **Vibrational density of states (VDOS) of D_2O in the far infra-red region for W/C mixtures at 0.84 (thin black line), 1.03 (thick black line), and 1.33 (gray line) g/cc and for liquid D_2O (line with gray circle).**

The spectra in the low frequency region (Figure 5.9) at different densities (for $\overline{\nu} < 300$ cm^{-1}) are almost identical, with the peak position around 168 cm^{-1} and are red shifted with respect to the spectrum of bulk water. This spectral aspect has been shown to signify specific solute-solvent interaction [41–43] wherein water is dissolved in a hydrophobic solvent.

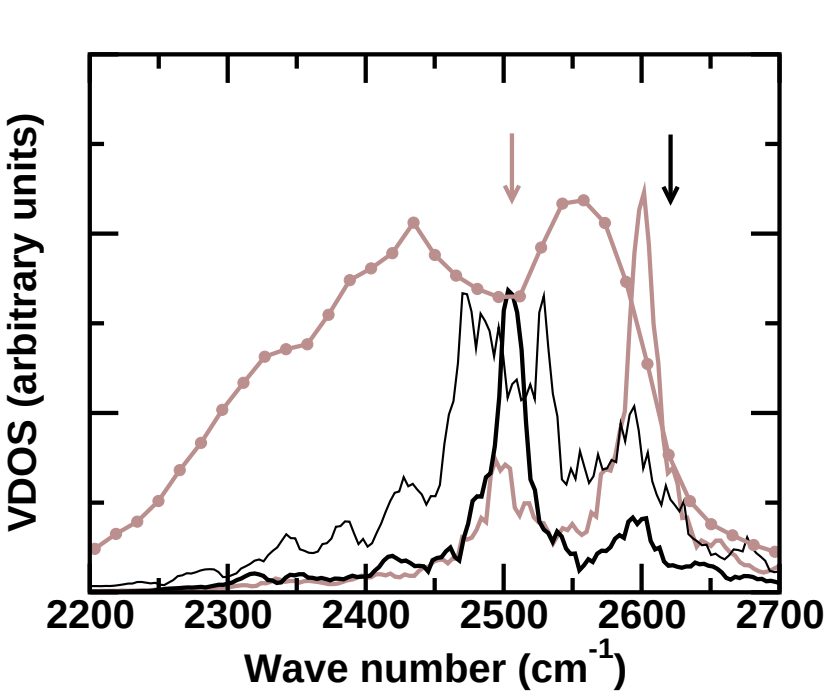

Figure 5.10: **VDOS in the stretching mode region of D_2O. Line descriptions are same as in Figure 5.9. The gray and black arrows represent the positions of symmetric and anti-symmetric stretching mode frequencies for a D_2O monomer, respectively.**

Figure 5.10 highlights the OD stretching region in heavy water under different conditions. The simulated profile of OD stretching mode in liquid water exhibits two broad bands between 2412-2553 cm^{-1}. These two peaks correspond to the symmetric and asymmetric OD stretching frequencies. In comparison with the liquid spectrum, the symmetric stretch mode in the water-CO_2 mixture at the lowest solvent density shows a sharp peak at 2500 cm^{-1} which is equal to the corresponding frequency in isolated D_2O [40]. In general, we observe a marginal red shift in these vibrational modes with respect to that of an isolated D_2O molecule, particularly in the asymmetric stretching mode. A blue

shift is observed for the spectra of the W/C mixture with respect to the liquid spectrum. These observations are consistent with expectations of molecular association. Tassaing et al. [44] have studied the shift in vibrational frequency with system pressure using infrared spectroscopic measurements. The red shift with increasing solvent density has been attributed to the attractive forces between the water-CO_2 pair. They observed a steeper frequency shift at lower densities, and an asymptotic behavior at higher solvent densities for reduced density values greater than 2.0 (or density around 0.93 g/cc). In comparison, our work corresponds to reduced system densities of 1.8, 2.24, and 2.84 at 32^{O}C. Our observation on the lack of a shift in the frequencies of the O-D stretching modes as a function of solvent density is not inconsistent with the experimental finding.

Bending (ν_2)

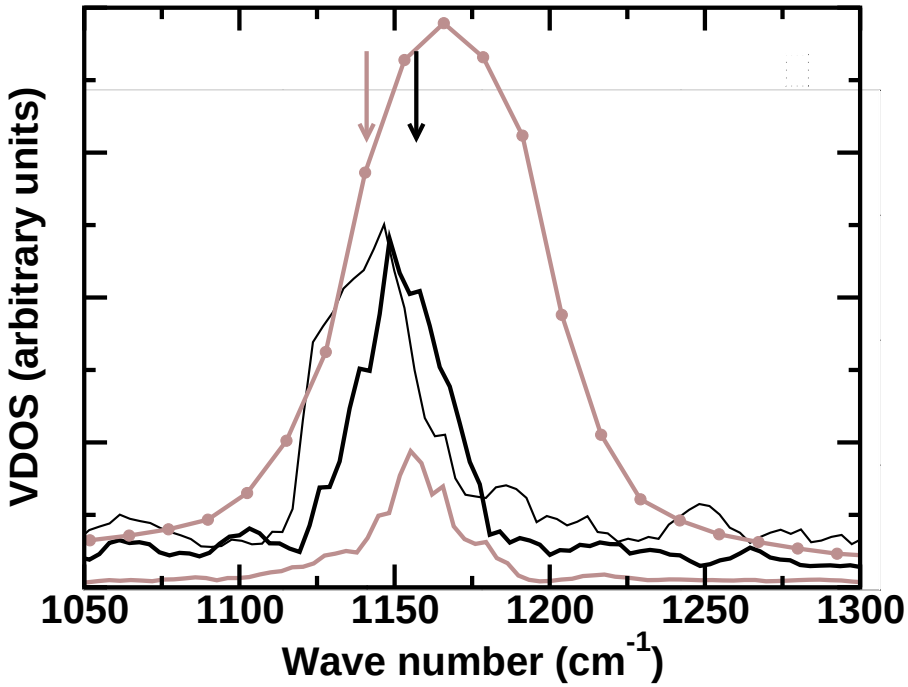

Figure 5.11: **VDOS in the bending mode region of D_2O. Line descriptions are same as in Figure 5.9. The gray and black arrows represent the bending mode vibrational frequencies for an isolated D_2O and a D_2O which is hydrogen bonded to CO_2 under isolated conditions, respectively.**

The vibrational density of states in the D-O_W-D bending (ν_2) region of the D_2O molecule in pure liquid, gas, and the D_2O-CO_2 mixtures are reported in Figure 5.11.

The nature of the spectral line shapes with increasing fluid density appears similar in the mixtures. In contrast to the observed red shift in the OD stretching frequency of D_2O in the mixture relative to an isolated molecule, an opposite behavior was noticed in the bending mode. In the mixture, the bending mode is present at around 1155 cm^{-1} whereas the same for isolated D_2O molecule appears at 1140 cm^{-1}. The ν_2 mode for the bulk liquid is even further shifted towards higher frequency with a peak at 1168 cm^{-1}. This blue shift in the ν_2 bending mode [45] with respect to the D_2O monomer is a common feature in water and is interpreted as due to the formation of hydrogen bonds with neighboring molecules [46]. To obtain a better understanding of the contribution from this type of interaction, an isolated hydrogen bonded D_2O-CO_2 molecular cluster maintained at T=5K has been studied using CPMD simulations. The hydrogen bonded dimer cluster exhibits a peak at precisely the same wavenumber as the water-CO_2 solution at the highest density, unequivocally identifying the cause for the blue shift (with respect to the gas phase value) as due to hydrogen bonding. We also observe a marginal, but significant blue shift in the bending mode of D_2O with increasing density. This shift signifies the hardening of the potential energy surface for this mode, and is likely due to the higher propensity for the formation of a hydrogen bond between D_2O and CO_2 at higher densities. The bending vibration of the water molecule distorts the hydrogen bond and the intermolecular geometry which causes the blue shift in this mode, with increase in density.

Rotational Relaxation

The rotational motion of water molecule has also been used to understand the specific interaction between water and surrounding CO_2 [41]. The influence of local solvent environment on the solute molecule can be measured by the study of reorientational time correlation functions. At short times, an inertial (free rotor) motion is expected for a solute molecule which gets hindered by its collision with the surrounding molecules. Here,

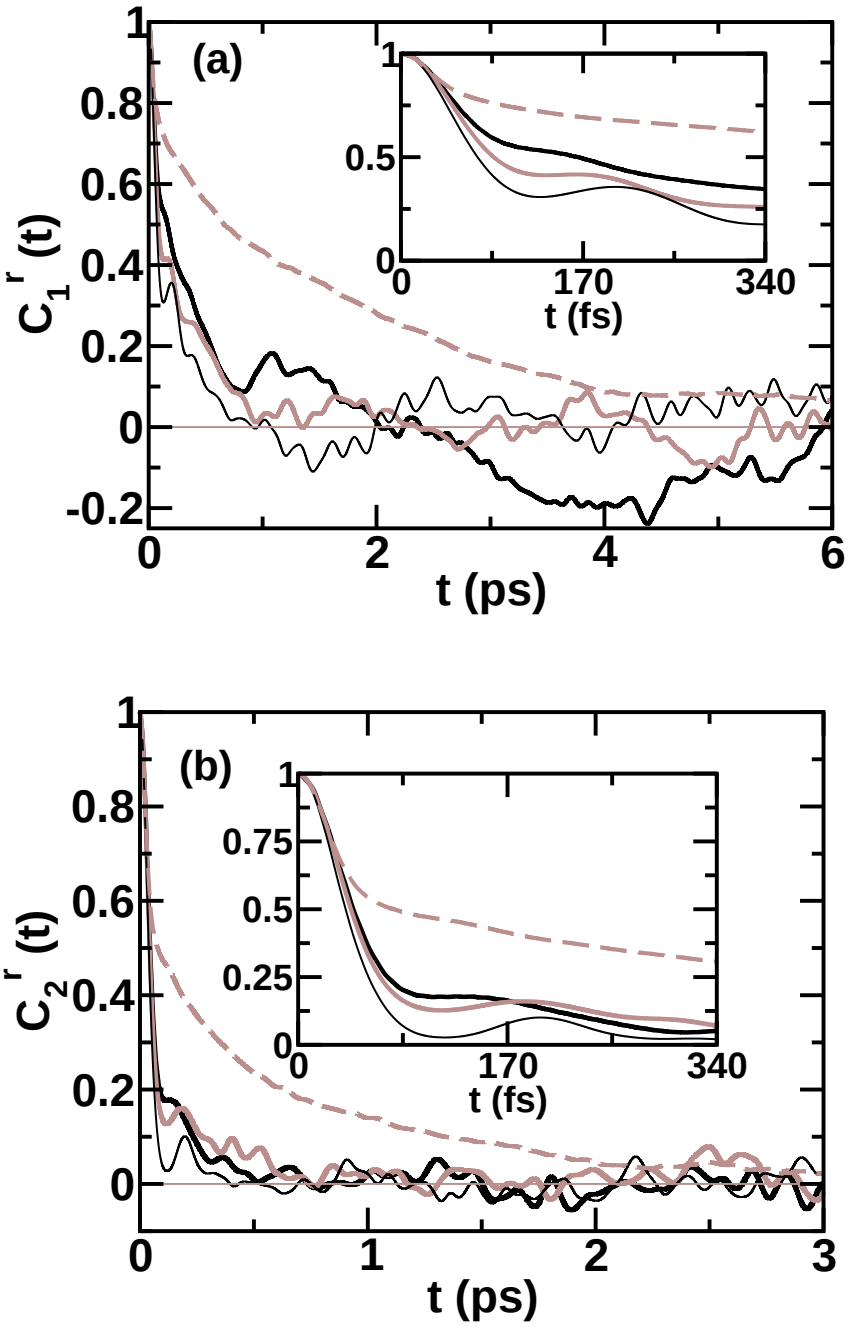

Figure 5.12: **Reorientational time correlation functions of D_2O bisector vector obtained from Eqn 1. We show here correlations for (a) first, and (b) second order Legendre polynomials in W/C binary mixtures at densities of 0.84 (thin black), 1.03 (thick gray), and 1.33 (thick black) g/cc and in liquid D_2O (dashed gray). Insets display initial decay.**

we report the first and second order Legendre polynomial reorientation correlation func-

tion (C_ℓ^r) of D_2O (Figure 5.12) which are defined as follows,

$$C_\ell^r(t) = \langle P_\ell(\mathbf{u}(0) \cdot \mathbf{u}(t)) \rangle \tag{5.1}$$

where, $\mathbf{u}$(t) is the D_2O bisector vector and ℓ represents the order of Legendre polynomial. Both C_1^r (Figure 5.12a) and C_2^r (Figure 5.12b) correlation functions indicate overall faster decay at lower densities. With increasing pressure, the time correlation functions (TCF) decay slower, an observation that is in agreement with the data of Tassaing et al [13]. The oscillations in the first order correlation function at shorter times are more prominent at the lowest density and the peak arises around 200 fs. Although the initial decay of the TCF in the 1:31 W/C solution and in liquid water [47] are similar, C_1^r(t) decays much faster in the hydrophobic environment of $scCO_2$ than in the hydrogen bonded network neighborhood present in liquid bulk water.

Interestingly, the peak positions of the oscillations at short times are similar in both C_1^r and C_2^r although C_2^r decorrelates much faster. In view of Fecko et al.'s [47] work on liquid water, we assign the peak that occurs around 200 fs in the water-CO_2 systems to the oscillatory motion of the intermolecular hydrogen-bond coordinate. Another investigation on OD oscillatory motion [13] of D_2O in supercritical CO_2 shows that the rotational motion along the C_2 symmetry axis of D_2O gets specifically perturbed by the local environment due to electron donor-acceptor type interaction between these molecular species.

5.4 Conclusions

We have carried out ab initio MD simulations of a solitary water existing in supercritical carbon dioxide at three densities, in order to understand the microscopic structure and dynamics. Such a study is important both from the point of view of practical uses of $scCO_2$ where it is employed along with water, as well as from the point of view of studying water in a hydrophobic medium under varied thermodynamical conditions [48].

Let us summarize our main conclusions. An electron donor-acceptor interaction mediates water and carbon dioxide, where the oxygen atom of water is the electron donor (Lewis base) and the carbon atom of CO_2 acts as the electron acceptor (Lewis acid). With increasing density, signatures of hydrogen bonding between the two species is also observed as a pre-peak or hump in the D_W-O_C g(r). The existence of the latter has also been identified through the observation of two distinct peaks in the O_W-C_C pair correlation function. The geometry of the water-carbon dioxide EDA complex is planar with the water oxygen lying in the equatorial plane around a carbon dioxide molecule. We also observe an increase in the dipole moment of the dissolved water molecule with increasing density of the solvent. At low densities, the mean dipole moment is found to be around 1.85D, similar to the gas phase value. However, at the highest density studied, this value increases to 2.15D, which is to be compared to the effective dipole moment in liquid water of 2.65D [49, 50]. A significant part of the increased dipole moment must come from the creation of a hydrogen bond through one of the protons of the water. This would increase the corresponding O-D covalent bond length, thus increasing the dipole moment of water.

Earlier, we had shown [6] (Chapter 3) that non-linear instantaneous geometries of CO_2 in the supercritical state are more likely to occur at lower densities (Chapter 3). The increasing density in the water-CO_2 solution influences the geometry of those carbon dioxide molecules which are present in the immediate neighborhood of water, in a non-negligible fashion. Such CO_2 molecules tend to exhibit a larger deviation from linearity at higher densities. The geometry of the water molecule too exhibits subtle changes with density. The distribution of O-D bond length splits at the highest density, the longer bond being identified with the proton that forms a hydrogen bond with CO_2. Interestingly, the distribution of the D-O-D angle exhibits two peaks at lower densities, and a single peak at the highest density. The change in the nature of this angle distribution signifies the transition of D_2O in this solution from a "free molecule" to a strongly interacting one.

The formation of a weak hydrogen bond between D_2O and CO_2 affects the vibrational

modes of water along expected lines. The O-D stretching frequency is red shifted with respect to the gas phase data, while the D-O_W-D bending mode is blue shifted. The former is consistent with the lengthening of the O-D intramolecular bond, while the latter results from the stronger near neighbor interaction present at higher densities in the solution. In essence, the structure and dynamics of water in this moderately hydrophobic solvent spans the range of properties between a water molecule in the gas phase and one that is present in low density, liquid water. Studies on the other end of the phase diagram, i.e., carbon dioxide dissolved in water, leading to the possible formation of carbonic acid [51] are likely to be taken up in future.

Bibliography

[1] E. Stahl, D. Gerard, *Perfum. Flavor.* **10**, 29 (1985).

[2] C. R. Coan, A. D. King, *J. Am. Chem. Soc.* **93**, 1857-1862 (1970).

[3] R. D. Smith, H. R. Udseth, B. W. Wright, Microscale Methods for Characterization of Supercritical Fluid Extraction and Fractionation Processes. In *Supercritical Fluid Technology*; J. M. L. Penninger, M. Radosz., M. A. McHugh., V. J. Kmkonis, Eds.; Elsevier Science Publishers: Amsterdam, 191 (1985).

[4] K. Jackson, L. E. Bowman, J. L. Fulton, *Anal. Chem.* **67**, 2368-2372 (1995).

[5] Y. Iwai, M. Uno, H. Nagano, Y. Arai, *J. Supercrit. Fluids* **28**, 193-200 (2004).

[6] M. Saharay, S. Balasubramanian, *J. Phys. Chem. B* **111**, 387 (2007).

[7] Y. Danten, T. Tassaing, M. Besnard, *J. Mol. Liq.* **117**, 49-61, (2005).

[8] S. R. P. da Rocha, K. P. Johnston, R. E. Westacott, P. J. Rossky, *J. Phys. Chem. B* **105**, 12092-12104 (2001).

[9] M. Parrinello, *Comput. Sci. Engg.* **2**, 22 (2000).

[10] R. Car, M. Parrinello, *Phys. Rev. Lett.* **55**, 2471-2474 (1985).

[11] Thermophysical properties of fluid systems, http://webbook.nist.gov/chemistry/fluid.

[12] A. Haghighi, J. E. Adams, *J. Phys. Chem. A* **105**, 2680 (2001).

[13] Y. Danten, T. Tassaing, M. Besnard, *J. Chem. Phys.* **123**, 074505-074511 (2005).

[14] M. E. Tuckerman, D. A. Yarne, S. O. Samuelson, A. L. Hughes, G. Martyna, *J. Comput. Phys. Commun.* **128**, 333-376 (2000).

[15] J. G. Harris, K. H. Yung, *J. Phys. Chem.* **99**, 12021-12024 (1995).

[16] L. X. Dang, B. M. Pettitt, *J. Phys. Chem.* **91**, 3349-3354 (1987).

[17] J. Hutter, P. Ballone, M. Bernasconi, P. Focher, E. Fois, S. Goedecker, D. Marx, M. Parrinello, M. E. Tuckerman, CPMD Version 3.11.1, Max Planck Institut fuer Festkoerperforschung, Stuttgart, and IBM Zurich Research Laboratory, 1990-2005.

[18] A. D. Becke, *Phys. Rev. A* **38**, 3098-3100 (1988).

[19] C. Lee, W. Yang, R. G. Parr, *Phys. Rev. B* **37**, 785-789 (1988).

[20] K. Lassonen, M. Sprik, M. Parrinello, *J. Chem. Phys.* **99**, 9080 (1993).

[21] M. Saharay, S. Balasubramanian, *J. Phys. Chem. B* **110**, 3782-3790 (2006).

[22] K. I. Peterson, W. Klemperer, *J. Chem. Phys.* **80**, 2439-2445 (1984).

[23] L. Fredin, B. Nelander, G. Ribbegard, *Chem. Scr.* **7**, 11 (1975).

[24] J. M. Stubbs, J. I. Siepmann, *J. Chem. Phys.* **121**, 1525-1534 (2004).

[25] T. Tso, E. K. C. Lee, *J. Phys. Chem.* **89**, 1612-1618 (1985).

[26] B. Jonsson, G. Karlstrom, H. Wennerstrom, *Chem. Phys. Lett.* **30**, 58 (1975).

[27] J. Sadlej, J. Makarewicz, G. Chalasinski, *J. Chem. Phys.* **109**, 3919-3927 (1998).

[28] A. Schiver, L. Schriver-Mazzuoli, P. Chaquin, E. Dumont, *J. Phys. Chem. A* **110**, 51-56 (2006).

[29] N. R. Zhang, D. D. Shillady, *J. Chem. Phys.* **100**, 5230-5236 (1994).

[30] G. H. Wannier, *Phys. Rev.* **52**, 191 (1937).

[31] N. Marzari, D. Vanderbilt, *Phys. Rev. B* **56**, 12847 (1997).

[32] P. L. Silvestrelli, N. Marzari, D. Vanderbilt, M. Parrinello, *Solid State Commun.* **107**, 7-11 (1998).

[33] P. L. Silvestrelli, M. Parrinello, *J. Chem. Phys.* **111**, 3572-3580 (1999).

[34] S. A. Clough, Y. Beers, G. P. Klein, L. S. Rothman, *J. Chem. Phys.* **24**, 1139 (1956).

[35] S. S. Xantheas, T. H. Dunning, *J. Chem. Phys.* **99**, 8774-8792 (1993).

[36] G. D'Arrigo, G. Maisano, F. Mallamace, P. Migliardo, F. Wanderligh, *J. Chem. Phys.* **75**, 4264 (1981).

[37] R. Bansil, J. Wiafe-Akenten, J. L. Taaffe, *J. Chem. Phys.* **76**, 2221 (1982).

[38] Y. Yeh, J. H. Bilgram, W. Kanzig, *J. Chem. Phys.* **77**, 2317 (1982).

[39] L. E. Bowman, B. J. Palmer, B. C. Garrett, J. L. Fulton, C. R. Yonker, M. Pfund, S. L. Wallen, *J. Phys. Chem.* **100**, 18327-18334 (1996).

[40] D. A. Draegert, N. W. B. Stone, B. Curnutte, D. Williams, D. *J. Opt. Soc. Am.* **56**, 64 (1966).

[41] T. Tassaing, Y. Danten, M. Besnard, E. Zoidis, J. Yarwood, Y. Guissani, B. Guillot, *Mol. Phys.* **84**, 769 (1995).

[42] Y. Danten, T. Tassaing, M. Besnard, *J. Phys. Chem. A* **104**, 9415 (2000).

[43] M. Besnard, Y. Danten, T. Tassaing, *J. Chem. Phys.* **113**, 3741 (2000).

[44] T. Tassaing, R. Oparin, Y. Danten, M. Besnard, *J. Supercrit. Fluids* **33**, 85 (2005).

[45] J. Sadlej, *Int. J. Quantum Chem.* **90**, 1191-1205 (2002).

[46] M. Kanakubo, T. Aizawa, T. Kawakami, O. Sato, Y. Ikushima, K. Hatakeda, N. Saito, *J. Phys. Chem. B* **104**, 2749-2758 (2000).

[47] C. J. Fecko, J. D. Eaves, J. J. Loparo, A. Tokmakoff, P. L. Geissler, *Science* **301**, 1698-1702 (2003).

[48] S. H. Lee, P. J. Rossky, *J. Chem. Phys.* **100** 3334 (1994).

[49] K. Watanabe, M. L. Klein, *Chem. Phys.* **131**, 157 (1989).

[50] S. W. Rick, S. J. Stuart, B. J. Berne, *J. Chem. Phys.* **101**, 6141 (1994).

[51] M. T. Nguyen, G. Raspoet, L. G. Vanquickenborne, P. T. V. Duijnen, *J. Phys. Chem. A* **101**, 7379-7388 (1997).

List of Publications

- ***Ab initio* investigations of structural, electronic, and dynamical properties of D_2O-supercritical CO_2 binary mixture**,
  M. Saharay, and S. Balasubramanian
  J. Phys. Chem. B (2007) (submitted).

- **Evolution of Intermolecular Structure and Dynamics in Supercritical Carbon dioxide with Pressure: An *Ab Initio* Molecular Dynamics Study**,
  M. Saharay, and S. Balasubramanian
  J. Phys. Chem. B **111**, 387-392 (2007).

- **Electron Donor-Acceptor Interactions in Ethanol-CO_2 Mixtures: An *Ab Initio* Molecular Dynamics Study of Supercritical Carbon dioxide**,
  M. Saharay, and S. Balasubramanian
  J. Phys. Chem. B **110**, 3782-3790 (2006).

- **Enhanced Molecular Multipole Moments and Solvent Structure in Supercritical Carbon dioxide**,
  M. Saharay, and S. Balasubramanian
  ChemPhysChem **5**, 1442-1445 (2004).
  Erratum: M. Saharay, and S. Balasubramanian
  ChemPhysChem **7**, 1167 (2006).

- ***Ab initio* Molecular-Dynamics study of Supercritical Carbon dioxide**,
  M. Saharay, and S. Balasubramanian
  J. Chem. Phys. **120**, 9694 (2004).